1-2023

Computational Performance Assessment of Buoyant Shrouded Turbines in UAE

Mohamed Farmaan Abdul Khader
mfa3254@rit.edu

Recommended Citation
Abdul Khader, Mohamed Farmaan, "Computational Performance Assessment of Buoyant Shrouded Turbines in UAE" (2023). Thesis. Rochester Institute of Technology. Accessed from

Rochester Institute of Technology

Computational Performance Assessment of Buoyant Shrouded Turbines in UAE

By

Mohamed Farmaan Abdul Khader

A Thesis Submitted
In
Partial Fulfillment of the
Requirements for the Degree in
Master of Science
In
Mechanical Engineering
Supervised by

Dr Ghalib Kahwaji

Department of Mechanical & Industrial Engineering
Rochester Institute of Technology
Dubai

Jan 2023

The thesis “Computational Performance Assessment of Buoyant Shrouded Turbines in UAE” by Mohamed Farmaan Abdul Khader has been examined and approved by the following Examination Committee:

Dr. Ghalib Kahwaji _
Professor and Chair (Advisor)
Dept. of Mechanical Engineering

Dr. Mohamed Samaha _
Associate Professor (Committee Member)
Dept. of Mechanical Engineering

Dr. Mohammed Abdulrahman _
Assistant Professor (Committee Member)
Dept. of Mechanical Engineering

Acknowledgements

I would like to thank my esteemed supervisor Dr. Ghalib Kahwaji. for his invaluable supervision, support, and guidance through valuable feedback throughout this project. My gratitude extends to Dr. Samaha for his support and guidance in the thesis. In addition, many thanks to all faculty and staff members of the mechanical and industrial department at the Rochester institute of technology for their valuable input. Finally, I would also like to thank my parents for their support throughout my Master's journey and their wisdom which pushed me to pursue further education.

Abstract

With the increase in the economic impact of fossil fuel consumption over the past few decades, the demand for alternative sources of fuel for consumer consumption led to the initiation of scientific research related to renewable resources. The present research aims at analyzing the wind energy capability at low and high altitudes in low wind regions like the UAE (United Arab Emirates) by studying the different wind speed-altitude models and studying the potential of augmenting wind turbines performance using diffuser augmented-floating turbine system incorporating the horizontal axis wind turbine (HAWT). The study was conducted computationally using Ansys Fluent and MATLAB software. The k-ω SST (Shear Stress Transport) turbulent model was used to carry out the simulation and the power was determined from the computational result. The computational simulation for both the bare turbine and the shrouded turbine was run at a base wind velocity of 8m/s. The determination of the airfoil profile for the design of the annular shroud was carried out in MATLAB with the computational results as the input parameter. The buoyant calculations for the study were carried out entirely theoretical utilizing the literature as a reference and a prototype representation of the buoyant turbine system is presented. The presented results are determined through a comprehensive comparison study between a buoyant shrouded turbine system and a bare turbine at altitudes of 18 m and 200 m respectively at a design wind velocity of 8m/s. The study concluded that the 13m chord length variant of the KT (Karman-Trefftz) profile provided a maximum of 270% increase in the available wind power ratio and a maximum of 61% increase in the air flow rate within the annular shroud. The NACA (National Advisory Committee for Aeronautics) symmetric airfoil having thickness of 25% was selected based on annular shroud volume as the performance in symmetric airfoil did not converge and presented a consistent increase in its shroud performance with thickness increase. The power ratio for 0^o and -2^o AOA (Angle of Attack) of 13m KT profile variants presented better results in comparison to the others. In analyzing the turbine with the inclusion of the shroud, the CFD (Computational Fluid Dynamics) performance results indicated a 201% increase in the generated turbine power when compared with the manufacturer bare turbine power. The conceptual design of the shroud presented a net buoyant lift of 17.01% higher than the weight of the system while the lift is also 24.7% higher than the net drag of the system. The conceptual representation of the system design is also presented for better visualization of the system design.

Table of Contents

List of Figures

List of Tables

List of Abbreviations

ABL - Atmospheric Boundary Layer

ABT - Airborne Turbine

AOA - Angle of Attack

ASTM - American Society for Testing and Materials

AWEA - Asia Wind Energy Association

AWT - Airborne Wind Turbine

BAT - Buoyant Air Turbine

BEMS - Boundary Element Model Systems

CFD - Computational Fluid Dynamics

DAWT - Diffuser Augmented Wind Turbine

DTU - Denmark Technical University

GIS - Geographical information System

HAWT - Horizontal Axis Wind Turbine

IRENA - International Renewable Energy Agency

KT - Karman-Trefftz

MFR - Mass Flow Rate

NACA - National Advisory Committee for Aeronautics

PV - Photo-Voltaic

RANS - Reynold Averaged Navier Stokes

REmap - Renewable Energy Mapping

RPM - Rotations per Minute

SST - Shear Stress Transport

TSR - Tip Speed Ratio

VAWT - Vertical Axis Wind Turbine

Nomenclature

Symbol		**Name**	**Unit**
A_{shroud}	-	Area if the shroud	m^2
A_{throat}	-	Throat area	m^2
b	-	Complex function real constant	-
bf	-	Bias factor	-
C, ζ	-	Chord length	m/%
C_D	-	Drag coefficient	N
Cp	-	Pressure coefficient	-
D	-	Shroud throat diameter	m
d(Ux,Uy,Uz)/dt	-	Rate of Change of Velocity	m/s^2
dP/dx	-	Pressure gradient	N/m^3
F_1	-	Blending function	-
F_B	-	Buoyant force	N
F_D	-	Drag force	N
g	-	Acceleration due to gravity	m/s^2
G_k	-	Turbulent kinetic energy generator	-
h	-	Height from ground to hub	m
Ho	-	Reference height	m
k	-	Turbulent kinetic energy	m^2/s^2
$L_{Conductive\ Tether}$	-	Length of Conductive Tether	m

$L_{\text{Steel Tether}}$	-	Length of the Steel Tether	m
l_m	-	Mixing length	m
M	-	Maximum camber calculated	m/%
m*	-	Mass flow rate	kg/s
Mr	-	Mass flow amplification factor	-
m_{turbine}	-	Mass of the Turbine	kg
N	-	Rotational speed	RPM
n_d	-	Number of Divisions	-
P	-	Position of Maximum Camber Calculated	m/%
$P\infty$	-	Stagnation pressure	N/m^2
P_{gauge}	-	Gauge pressure	N/m^2
$P_{\text{operating}}$	-	Operating pressure	N/m^2
P_{total}	-	Total pressure	N/m^2
P_{turbine}	-	Turbine power	W
r	-	Growth rate	-
R	-	Radius of a circle	m
Rs	-	Throat shroud radius	m
T	-	Calculated thickness	m/%
$T_{\text{conductive}}$	-	Tensions conductive tether	N
t_{material}	-	Thickness of the Material	m
t_{steel}	-	Thickness of the steel tether	mm
T_{steel}	-	Tension steel tether	N

T_{torque}	-	Turbine torque	N-m
U, U_{wind}, Vo	-	Reference velocity	m/s
u, V	-	Calculated velocity	m/s
u', v'	-	Velocity fluctuations	m/s
Ux,Uy,Uz	-	Velocity in Coordinate Direction (x,y,z)	m/s
V steel Support	-	Volume of the steel tether	m^3
$V_{allowance}$	-	Allowance volume	m^3
V_{shroud}	-	Volume of the shroud	m^3
w	-	Complex function	-
$W_{He/H}$	-	Weight of lighter than air gasses	N
W_{shroud}	-	Weight of the shroud	N
$W_{turbine}$	-	Weight of the turbine	N
xl	-	X axis -Coordinate variable Lower	-
xu	-	X axis -Coordinate variable Upper	-
y, H	-	Calculated height	m
y_c	-	Coordinate camber variable	-
y_l	-	Y axis -Coordinate variable Lower	-
y_t	-	Coordinate thickness variable	-
y_u	-	Y axis -Coordinate variable Upper	-
z	-	Complex number	-
Zo	-	Roughness length	m
α	-	Friction coefficient	

α_{yaw}	-	Yaw angle	deg
δ	-	Boundary layer thickness	m
ε	-	Eddy Dissipation rate	-
θ	-	Inclination angle steel support tether	deg
θ_3	-	Inclination angle conductive support tether	deg
$\theta_{declination}$	-	Declination angle	deg
θ_{slope}	-	Slope angle (airfoil design)	deg
κ	-	Von Karmann’s constant	
λ	-	Tip speed ratio	-
μ	-	Dynamic viscosity	m^2/s
μ_t	-	Turbulent viscosity	m^2/s
Φ	-	Trailing edge angle	deg
ω	-	Specific Eddy dissipation rate	-
ω_N	-	Angular velocity	rad/s

Chapter 1

Introduction

Renewable energy is one of the most advent sources of electricity production considered around the world, for they are not scarce and viable for energy generation. There are numerous categories of renewable energy sources that can contribute to world energy production such as solar, wind, and biomass, to name a few. The statistical studies conducted on greenhouse gas production stated that the majority of greenhouse emissions is caused by fossil fuels [1,2] and, the two most effective sources of electricity production introduced for ecological benefits are hydro and wind energies.

1.1. Renewable Energy Road Map (REmap), Analysis of Renewable Energy Consumption:

Wind energy is one of the promising sources that has observed a rise in demand over the last few decades. A study conducted by Richard Bowers [3] in the US showed that the wind power generation of 300 million MWh has exceeded the hydropower generation by 26 million MWh giving an 8.6% percent increase in 10 years as shown in figure 1.1 below.

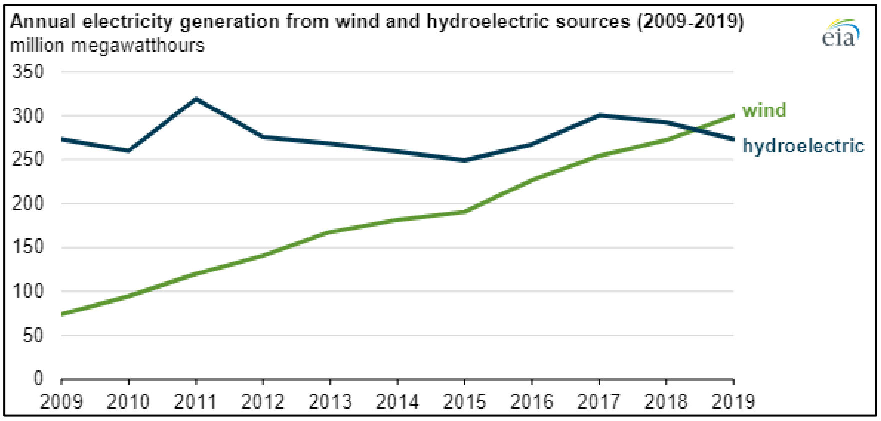

Figure 1.1. Wind vs Electrical Energy Annual Consumption from 2009-2019 in the US [3]

The total world annual generation from renewables showed that wind energy supplied around 6% of the world energy consumption and came ahead of hydro energy generation [4]. According to a study conducted by the Asia Wind Energy Association (AWEA), it was stated that the solar energy capability of UAE was overshadowed by the utilization of other forms of renewables which led institutes like Masdar to start investing in research to introduce wind energy in UAE [5]. A recent study by Masdar Institute and IRENA (International Renewable Energy Agency) noticed that the introduction of small turbines is contributing around 1% of the energy in and around UAE and concluded that UAE can harness more wind energy than what is observed [6,7]. A recent study by Masdar Institute and IRENA (International Renewable Energy Agency) noticed that the introduction of small turbines is contributing around 0.5% of the energy in and around UAE and concluded that UAE can harness more wind energy than what is observed [6,7]. The REmap projections towards the year 2030, conducted by IRENA in association with Masdar institute, stated that though solar energy is a dominant source of renewables in UAE, the country still has the capability to produce more wind energy as the average measured wind speed can exceed up to 12 m/s in certain regions [6]. The statistical data presented that the UAE's renewable energy usage could increase by 10 % while the total energy consumption mix could increase by 25% by 2030, see table 1.1 and figures 1.2 and 1.3.

Table 1.1. REmap analysis of Energy Consumption UAE [6,7]

Energy Production	**Percentage**	
	2020	2030
Non-Renewable	93	60
Renewable	7	40
Hydro and Marine	0	0
Solar	7	34.143
Wind	0	1.43
Bio-energy	0	1.43
Geothermal	0	0

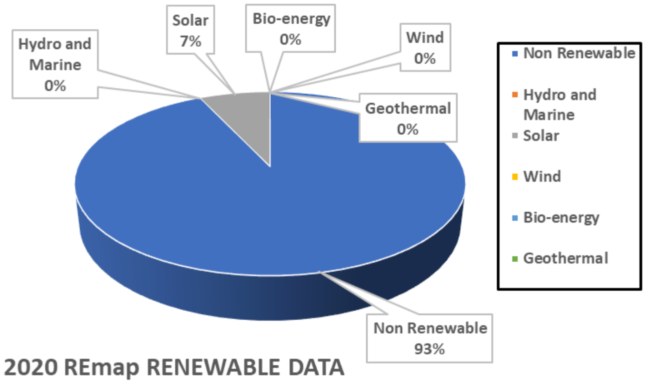

Figure 1.2. Renewable Energy production, 2020, UAE [6,7]

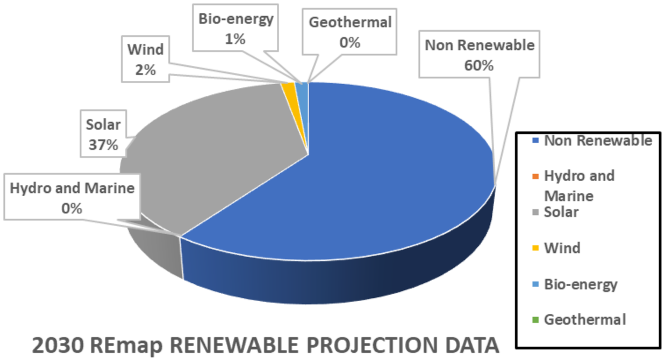

Figure 1.3. Projected Renewable Energy Production by 2030, UAE [6,7]

The presented statistical projections for wind farms in UAE indicated that, by the year 2030, the onshore wind farms could generate gross electrical energy of up to 1.2 Twh/ year while the offshore energy production will stay negligible. The overall electrical energy contribution from wind energy could reach up to 2% by the year 2030 as per the same study [6]. The above-mentioned study showed that fossil fuels and solar energy are the major sources of electricity production in the UAE while other renewables (Wind Energy, Geothermal Energy, and Biofuels) contributed a small percentage to the energy mix of the country [7].

1.2. Wind Energy and its technological Advancements:

Wind turbines were first introduced in the year 1887 by the inventor James Blyth [8]. The optimization and modification of the turbines since then led it to be classified into Horizontal Axis Wind Turbines (HAWT) and Vertical Axis Wind Turbines (VAWT). Scientists have introduced various modifications to turbine designs to increase its performance [9]. One of the recent turbine modifications is the development of Airborne Wind Turbines (AWT).

AWT's are turbines that have the ability to generate power at higher altitudes. They are classified into fly-gen type and ground-gen type based on the location of the generator. Ground-Gen type turbines have the capability of generating and storing the electricity at the ground station with the generator mounted at the ground level while the tethered airborne turbine systems are operating at higher altitudes. The electricity generation through ground-gen type turbine systems are harnessed through aerodynamic forces acting on the airborne system, and in some variants of the optimized systems, a fraction of the generated electricity is utilized intermittently to account for the recovery stage during the process. That is the tension in the tether generated from the lift force and the drag force acting on the airborne device will uncoil the winded tether within the generator for generating power. To repeat the process, the airborne wind turbine is winded back to the operating altitude where high wind forces are experienced, by utilizing less than 5% of the generated electricity to carry out the task [10]. Fly-Gen type turbine systems can generate electricity at higher altitudes with the generator attached to the turbine and the power generated from high altitudes is transmitted to the ground station through a conductive tether [11]. The system adopted in the current thesis is a fly-gen type airborne wind energy system. An example of the fly-gen and the ground-gen type can be observed from figures (1.4A and 1.4B) below.

A) Fly gen type Wind turbine [12]

B) Ground gen type Wind Turbine [13]

Figure 1.4. Type of Airborne Wind Turbine

Another performance improvement tool is the converging annular shroud addition to the turbine which augments airflow through the turbine and increases the wind velocity at the throat leading to a significant increase in power generation. The shroud as a mode of turbine system optimization was looked into by Ben Glass of the Massachusetts Institute of Technology [14], figures 1.5 and 1.6. This concept of airborne wind energy depends solely on the performance of the shroud profile utilized vis a vis the location of the shroud testing region.

Figure 1.5. Buoyant Air Turbine [15]

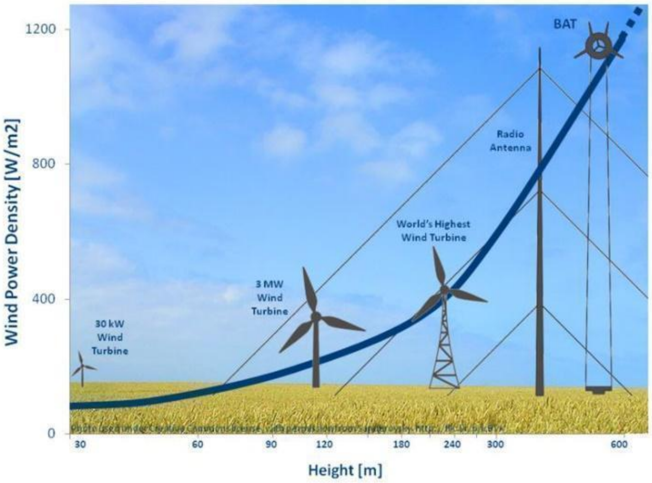

Figure 1.6. Power Density comparison of different BAT vs Conventional Wind Turbine [16]

1.3. Problem Statement:

As presented above, wind energy, hydro energy, and solar energy rose the ranks amongst the other energy production sources as the most promising renewable energy sources. IRENA, Abu Dhabi, surveyed the atmospheric capability of UAE and other low wind regions around the world, and they observed that high temperature and low wind regions like UAE have good wind capability at higher altitudes. With the available wind capability in UAE, Masdar has introduced plans for a 30MW wind turbine at Sir Bani Yas Island with the hope of increasing the countries total power capability and increasing the renewable demand in power generation [5]. The wind flow capability of these regions brought forward the concept of airborne turbines. The studies on turbine system optimizations utilizing the shroud technology are limited. The present thesis incorporates the annular shroud variant of the turbine modification, whereas the past studies corresponding to the incorporation of the annular shrouded turbine specific to low wind regions are rare. Thus, there is a need for a better understanding of how different variants of ABT (Airborne Turbines) modifications can be incorporated based on the region's boundary specifications.

1.4. Research Objective and Methodology:

The present study incorporates a comparison study between the buoyant shrouded turbine and the bare turbine through a comprehensive numerical analysis of the turbine power and its performance characteristics using Ansys Fluent. Prior to the comparison, an optimized design of a turbine shroud is performed and an inference into the wind speed relationship to altitude is established. The study utilizes the Aeolos H 30kW as the base rotor. The turbine was modeled utilizing the CATIA V5 software with the blade dimensions DU 93 W210 referenced from Yirtici and Perry Roth Johnson [17,16]. The shroud optimization study will be carried out by initially determining the shape of the profile to be utilized for the shroud design. Then a profile elimination methodology, based on the parametric comparison between the airfoil profiles, is conducted to finalize a high-performance profile for shroud optimization. The airfoil shape determination study is sub-categorized into the KT and the NACA 4 series airfoil models. Based on past studies, it is stated that the KT methodology utilizes a conformal mapping method to convert a unit circle in a complex plane to an airfoil in a cartesian/polar plane [18]. As a result, the airfoil profile is derived by varying the radius of the unit circle and the real constant in the complex plane linearly resulting in an airfoil profile whose chord length ranges from 3m to 15m for every positive odd integer. In the case of the NACA 4 series airfoil profile, the symmetric airfoil is taken into consideration with the chord length finalized from the analysis of the KT airfoil. The thickness ranging from 12 – 26% for every positive even integer is analyzed [14]. The shroud optimization considered the following parameters: the pressure coefficient, the velocity profile especially at the throat region, the mass flow rate, the mass flow rate amplification factor, the wind power, and the area ratio. The computational results are to be derived utilizing MATLAB, ANSYS Fluent, CATIA V5, and Xfoil.

The final aim of examining the utilization of shrouded buoyant wind turbines to increase the power coefficient (Cp) of the turbines in low-wind regions such as the UAE will then be evaluated. The Aeolos H 30kW turbine with a DU93 W 210 blade is chosen as a reference machine for this study. The Rotor and the Shrouds are modeled using the CATIA V5 design software before importing them into the ANSYS software. The present research is carried out in five phases:

- The UAE wind data exploration.
- Shroud Optimization Study
- Altitude-Velocity model derivation
- The numerical model development and validation
- Floating system realization and design for the UAE.

1.5. Structure of the Thesis

The dissertation is organized in six chapters, with chapter one presenting a brief description of the renewable sources along with the references presenting statistical data on the consumption of renewables in UAE. Subsequently, a brief description of modern wind turbines and airborne wind turbines is presented. The problem statement mentions the lack of studies related to the development of AWT and their application in the UAE. Finally, a description of the research objective to present a buoyant turbine system that is optimal for utilization in the UAE is presented along with a brief discussion on the research methodology carried out for attaining the objective. The second chapter presents the literature and the past research that served as a base in attaining the objective of the thesis. The history of modern wind turbine systems, a description of the introduction of AWT systems, and the research studies related to the development of AWT systems is presented. Additionally, the research studies that presented a foundation for the five phases of the studies carried out in the thesis are presented. The third chapter of the thesis discusses the methodology to carry out the research objective for the dissertation. The model design of the turbine and the annular buoyant shroud, the mesh gradient study, the mathematical model, and the input boundary conditions carried out to conclude the research objectives of the dissertation are presented. The fourth chapter of the thesis presents the wind data results and the optimum altitude model results that validate the velocity profile with increase in the altitude within the boundary layer, concept of the study. The comparison between the logarithmic law and the power law is initiated and the meteorological data representation of the wind velocity distribution across the UAE is presented. The fifth chapter presents the computational results for the annular shroud optimization study conducted for both the KT model and the NACA series symmetric airfoil, a performance comparison study between the bare turbine and the optimized annular shroud turbine system with the power generated as the defining parameter, and finally a preliminary study on the buoyancy calculation introduction with a conceptual design of the system and a visual representation. The final chapter is concluded with a summary of the results with the potential future developments that can be carried out to further develop the study.

Chapter 2

Literature Review

The renaissance in the field of renewable sources after the disclosure of the long-term effects of the greenhouse gas influenced by non-renewable sources has renewed many ideas to utilize the abundant sources of nature to our advantage [19]. Amongst the different available renewable sources, the increase in demand for the Photovoltaics (PV) and wind energies have been registered to about 27% and 13% respectively till today, [20], out of which the UAE presented 8% increase in renewable and nearly a 90% increase in the non-renewable generation till 2019 with the consumption of the non-renewable decreasing by 5% till 2019. Though there is an increase in non-renewable energy generation in the UAE by 90% over the years 2010-2019, electricity production from PV has seen a 94% increase over the same period. With the potentiality of wind energy production in UAE [5], turbine modification studies are to be considered to introduce the wind energy utilization capability in UAE. Though the research specific to UAE, carried out by Masdar Institute, showed promising results with standard turbines, complications are faced when concluding the location for the turbine placement [5]. Therefore, the modified turbine design specific to the conditions of the UAE has to be looked into to tackle the issue of lack of renewable source reliability and production. In this chapter, we will observe the past studies in the field of wind turbines and how they tackled the parameters and boundary conditions presented in their respective research.

2.1. Geographical Terrain Data and Atmospheric Boundary Layer Study:

The atmospheric boundary layer represents the layers of atmosphere observed below the troposphere where boundary conditions of pressure and temperature are directly influenced by the surface of the earth [21]. The Atmospheric Boundary Layer (ABL) plays a vital role in determining the performance of wind turbines as it affects both the upstream, and downstream and the wake created behind the turbines [22]. The different terrain distributions present variable effects in the boundary layer as well as the velocity flow through the turbine. The turbine placement location is selected based on the altitude range where the influence of the roughness length by the terrain on the earth’s surface diminish and effect on turbine operations is minimal, see figure 2.1 below [22].

To best utilize the wind, turbines shall be placed at the height where the velocity profile starts leveling, a sign of stabilizing boundary layer away from terrain roughness, [21].

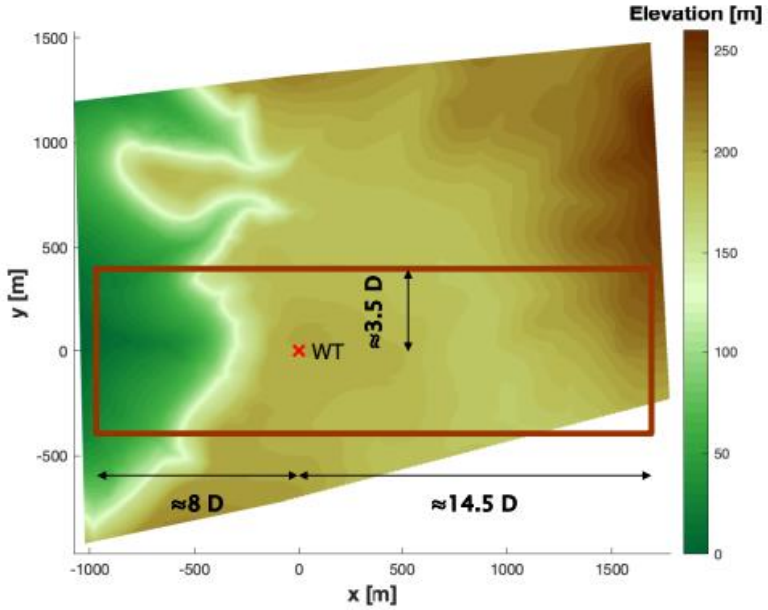

Figure 2.1. Topographic map of Testing Site with wind direction data [22]

The parameter that influences the ABL is the terrain profile which can be characterized by the roughness parameter, Zo. The roughness length (Zo) can be defined as the thickness of protrusions from the earth's surface [23]. The other parameter used to characterize the ABL is the surface friction coefficient of the terrain (α). The turbulent boundary layer velocity profile is well explained by the 1/7th power law, [24,25], given as:

$$\frac{u}{U} = \left(\frac{y}{\delta}\right)^{\frac{1}{7}} \tag{2.1}$$

Where, δ =Boundary Layer Thickness, u =flow velocity, U= reference velocity and y= height from the surface

The two equations used to define the velocity profile in the ABL are the power law equation, stated above, and the logarithmic equation which was defined later as an improved alternative to the power law. The first altitude model equation, the power law, was studied at the Sandia National Laboratories in Albuquerque, New Mexico, where it was concluded that the altitude model used before the year 1985, i.e., the 1/7th power law, resulted in an inaccurate result at altitudes above 100 m according to a comparison between experimental result and theoretical results. The inaccuracy in the 1/7th power law model is a result of the equation's incapability to take the atmospheric thermal stratification into account. This inaccuracy was studied and through experimental validations, the introduction of the modified power law based on terrain specifications was introduced as:

$$\frac{u}{U} = \left(\frac{y}{\delta}\right)^{\alpha} \tag{2.2}$$

where, α = friction coefficient

It was estimated that the power law is more accurate in representing the ABL up to the range of 50-100m from the ground surface. In 1988, Silsoe Institute of Technology researchers, [26], examined the logarithmic velocity profile suitability to describe the ABL and concluded that log law better is suited than the exponential, power, profile. The significance of the roughness length in comparison to the friction coefficient and the revision of Davenport's roughness length classification was presented by Wieringa. The utilization of the friction coefficient presented variable inaccurate data when determining the velocity profile of a region because of its dependency on the altitude of the boundary layer [26]. Whereas the roughness length is deemed to be independent of the altitude and is directly related to the gathered terrain data, however, the relation between the roughness length and the friction coefficient was discovered and was presented in the form of the following equation:

$$\alpha = \frac{1}{ln\left(\frac{\sqrt{HH_o}}{Z_o}\right)} \tag{2.3}$$

where, H = desired altitude value, Ho = reference altitude value, and Zo = Roughness Length

The Davenport roughness length classification presents data for non-complex terrain, his classifications of roughness length presented accurate results even though the classification is based on the average observation of a terrain. The classification is still being revised by researchers through geo-topographical study and the classifications are still utilized for the ABL analysis carried out in present research studies. The classification can be observed in table 2.1 below.

Table 2.1. Davenport's Revised Roughness Length Classification [26]

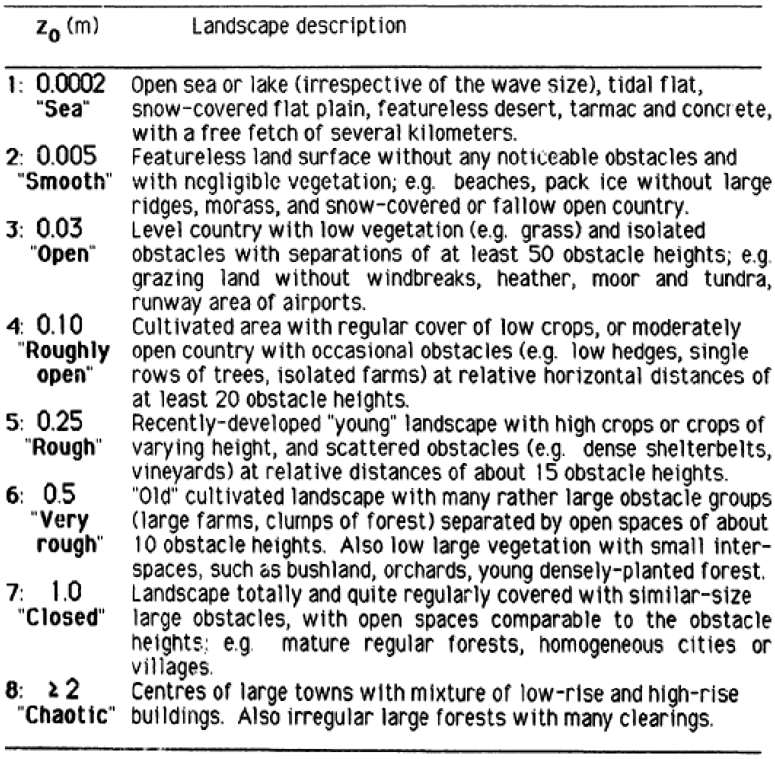

z_0 (m)	Landscape description
1: 0.0002 "Sea"	Open sea or lake (irrespective of the wave size), tidal flat, snow-covered flat plain, featureless desert, tarmac and concrete, with a free fetch of several kilometers.
2: 0.005 "Smooth"	Featureless land surface without any noticeable obstacles and with negligible vegetation; e.g. beaches, pack ice without large ridges, morass, and snow-covered or fallow open country.
3: 0.03 "Open"	Level country with low vegetation (e.g. grass) and isolated obstacles with separations of at least 50 obstacle heights; e.g. grazing land without windbreaks, heather, moor and tundra, runway area of airports.
4: 0.10 "Roughly open"	Cultivated area with regular cover of low crops, or moderately open country with occasional obstacles (e.g. low hedges, single rows of trees, isolated farms) at relative horizontal distances of at least 20 obstacle heights.
5: 0.25 "Rough"	Recently-developed "young" landscape with high crops or crops of varying height, and scattered obstacles (e.g. dense shelterbelts, vineyards) at relative distances of about 15 obstacle heights.
6: 0.5 "Very rough"	"Old" cultivated landscape with many rather large obstacle groups (large farms, clumps of forest) separated by open spaces of about 10 obstacle heights. Also low large vegetation with small inter-spaces, such as bushland, orchards, young densely-planted forest.
7: 1.0 "Closed"	Landscape totally and quite regularly covered with similar-size large obstacles, with open spaces comparable to the obstacle heights; e.g. mature regular forests, homogeneous cities or villages.
8: ≥ 2 "Chaotic"	Centres of large towns with mixture of low-rise and high-rise buildings. Also irregular large forests with many clearings.

Jongyeon [27] conducted a study to estimate the roughness length of the terrain in the high wind density region of Tokyo, Japan using a DOPLER LIDAR SYSTEM (DLS). They concluded that as a result of the different surface characteristics observed at the respective set sector of Tokyo, the variation in the roughness length of the region was determined through the velocity variation as a result of the adverse pressure gradient observed on the surface from the LIDAR system. Richard and Hoxey computationally theorized the effect of log law by deriving an equation that accounts for the turbulent characteristics experience in the ABL and plotting the trend of the velocity profile for higher altitudes. The studies were validated with the experimental data carried out with ultrasonic anemometers at the Silsoe Research Institute, see figure 2.2 below [28].

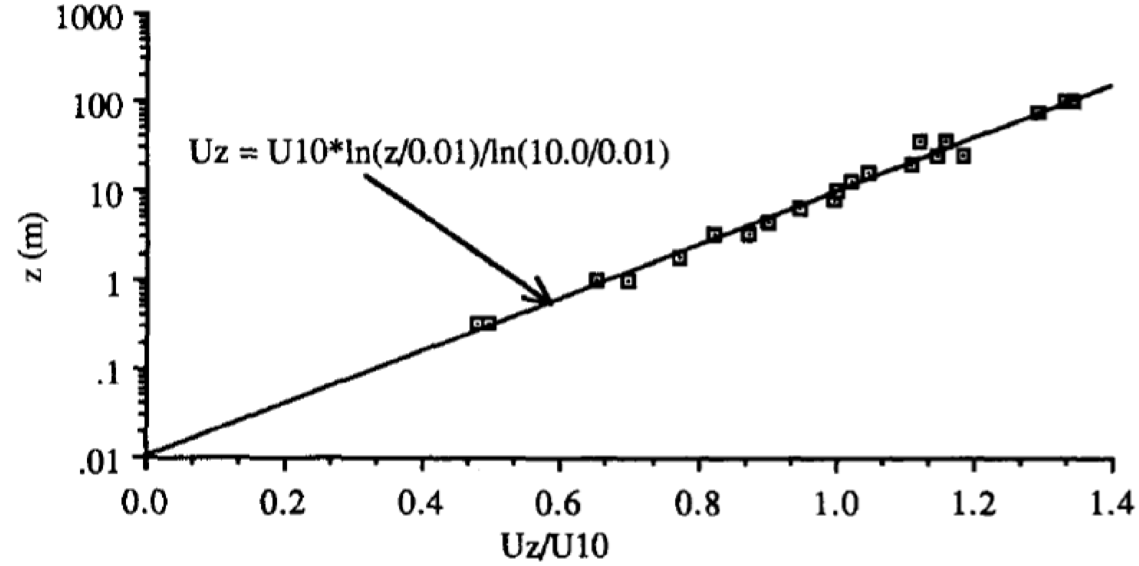

Figure 2.2. Silsoe Research Institute experimental data vs the log law data comparison 1988 [28]

2.2. Diffuser Augmented Turbine Modification Studies:

The history of wind energy was first introduced in the early 1st to 18th century with its application in pumping water, grinding wheat, and other auxiliary purposes. The first turbine (figure 2.3) introduced to generate electricity was designed by James Blyth in Scotland in the late 1800s [29,30].

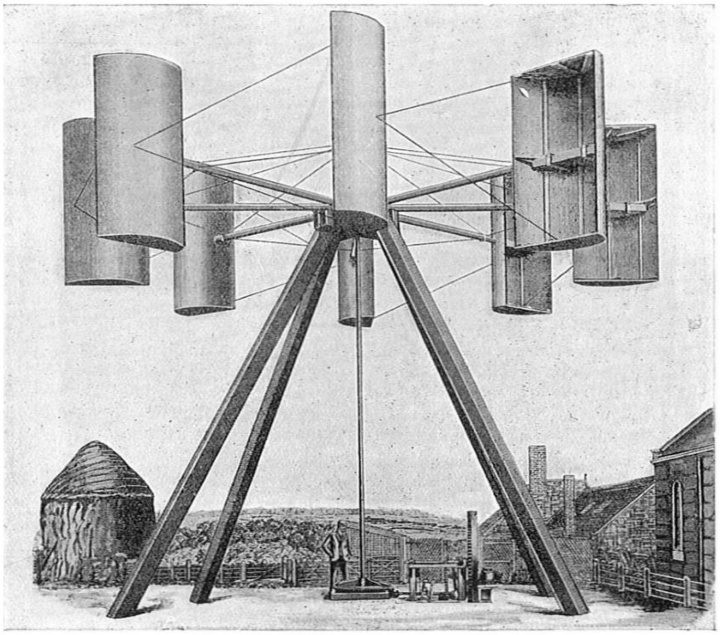

Figure 2.3. James Blyth 1891 Wind Turbine [30]

Ever since the introduction of the first turbine, there have been many design advances over the centuries for better energy harvesting and improved turbine performance. After the recent awareness of the ecological impact of non-renewable fossil fuels from the dispersed greenhouse gasses from energy production plants, there has been a surge in the research and development of optimized turbine designs which lead to many improvements including the concept of the airborne wind system that was first introduced by Ockles, [31], from the Denmark Technical University (DTU) in the year 2001, figure 2.4 below.

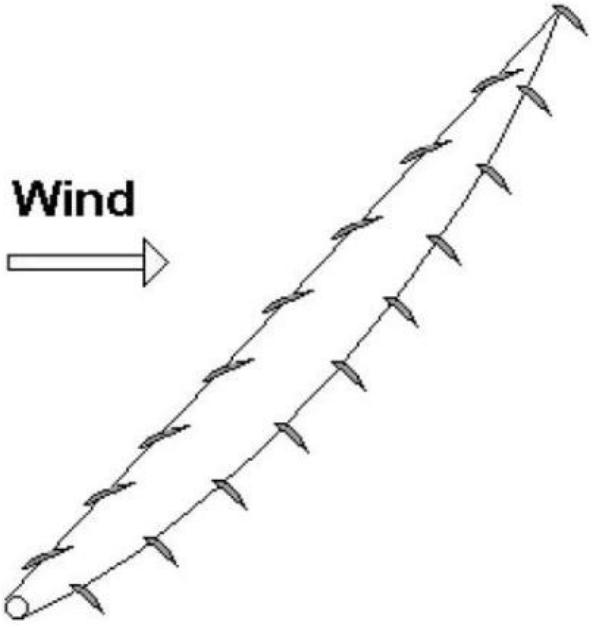

Figure 2.4. Ladder mill airborne wind energy system [31]

The lift and the drop generated from the airfoil blades facing the wind direction create an intermittent up-and-down motion that rotates the shaft on the ground and generates electricity. The blades are positioned in a way that the sagging end blades possess a higher angle of attack to generate high lift whereas the tension side of the blade drops the system down as a result of the downward force generated [31], this wind energy system is categorized under the ground-gen type. The airborne wind energy sector further developed and parted into a separate field called the fly-gen type system. The first fly-gen type wind energy system was introduced by a company called Maegenn Power Inc in Ontario in the year 2010, figure 2.5 below. The wind energy system designed by the company presented a horizontal rotor system that is lifted by the buoyant effect of the balloon enveloping the whole system and the lift force generated as a result of the Magnus effect around the balloon setup. The turbine is tethered to the storage and the transmission system located at the ground station. The generator located with the buoyant system generates electrical energy and it is transmitted to the ground station via a conductive tether that acts as both the support and energy transmission system for the ground station [32].

Figure 2.5. MARS (Maegenn Air Rotor System) 2010 [32]

The theoretical study to improve the performance of the turbine through a diffusive cowling was initially researched by M Sanuki from the meteorological institute in the 1950s, [33]. The study researched and reviewed different design modifications of the turbine with venturi-diffuser cowling. The venturi diffuser presented 1.3 times increase in the velocity flow near the throat in comparison to the free stream velocity which can be observed from figure 2.6, where the blank region of the plot presenting the particular value range as a result of the venturi effect. The study was validated experimentally and presented that the turbine power coefficient of the ventilated turbine is 4% more than without the venturi.

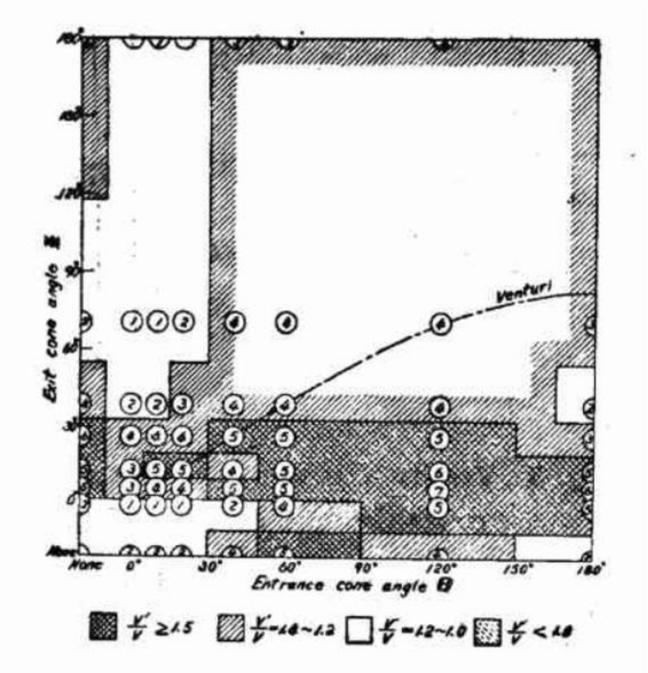

Figure 2.6. Throat Velocity Distribution Plot [33]

One of the relatively recent studies that incorporated the concept of DAWT, studied the effect of the velocity flow through a flanged diffuser. With the study carried out in a 1.5m x 2m wind tunnel, the study aimed to harness the separation at the end of the flanged diffuser, figure 2.7, to increase the mass flow and velocity by drawing the flow in from the inlet. The study concluded that though the turbine operations and local mean velocity behind the turbine are similar with and without the flanged diffuser, the four times increase in the performance of the flanged turbine is a result of the increase in velocity flow at the throat section because of the considerable separation created at the outlet. The challenge faced by the DAWT system is the recorded performance increase in the turbine was observed to occasionally reach beyond the Betz limit of 59.2% even though the system setup operations are similar to that of the standard turbine [34].

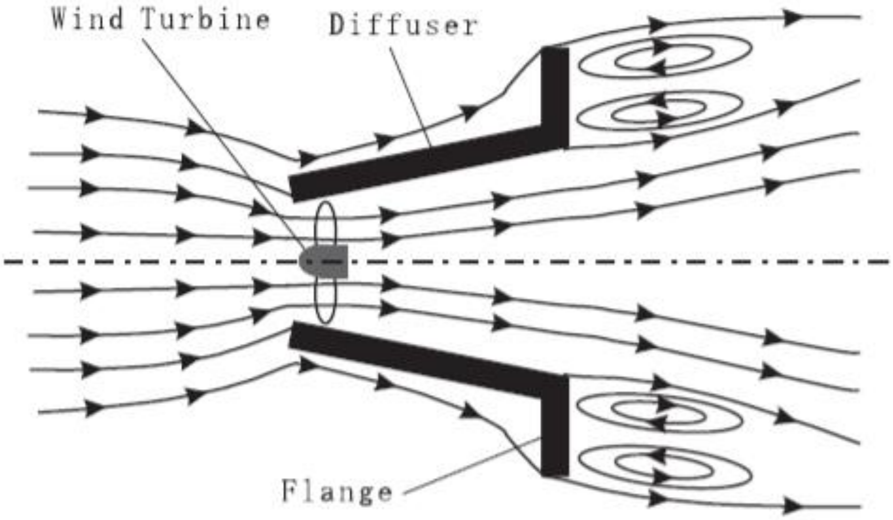

Figure 2.7. Flanged Diffuser Streamline flow [34]

The application of a diffuser to increase the performance of wind turbine systems inspired further research studies. The BAT by Altaerous Technologies, Ben Glass, MIT introduced was introduced in 2020 to tackle two advantages at a time. The Ben-Glass airborne system depicted in Figure 2.8 (a and b). The turbine system is a fly-gen type system that had the capability of harnessing the high wind velocities at high altitudes in the atmospheric boundary layer and is also capable of increasing the mass flow/velocity flow through the annular shroud. The author presented intellectual concepts of the turbine and stated that the annular shroud in the BAT presents good performance characteristics when the shroud profile design has a thickness ranging from 12% - 30% of the chord length. The working principle of the system is primarily based on the buoyant forces generated as a result of the difference between the density of air and the density of the gas utilized in the envelope. Since it is categorized under the fly-gen type of AWT system, the generated electricity was transferred to the ground station via a conductive tether [14]. The system was tested at Alaska where the cost of electricity is about 1$/kWh of consumption, but the 30 kW BAT system was generating enough energy that it had the capability of reducing the electricity consumption cost by 18 cents /kWh [12].

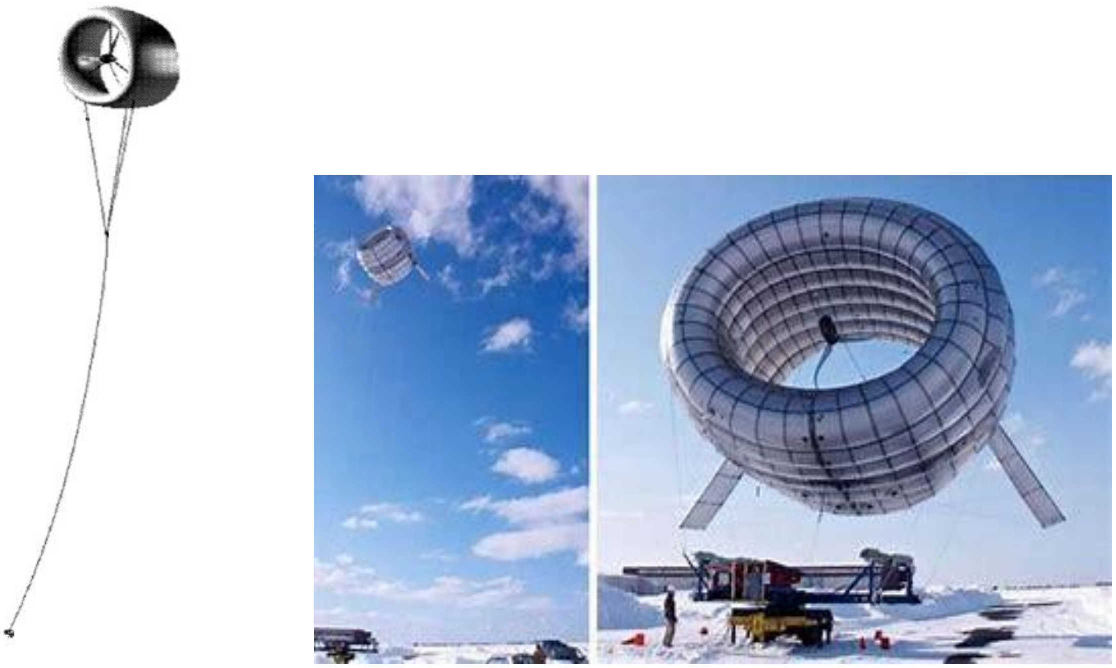

(a) (b)

Figure 2.8. BAT System Altaerous Technologies [12,14,15]

Surprisingly only limited studies are carried out in the development of the fly-gen type. Most of the research carried out in the AWT sector are computational studies that present a distinct analysis of the performance of the setup with the references taken as experimental validations. Saleem, [11] compared the performance of different geometrical shroud profiles (NACA 5415, NACA 9415, and NACA 5425) using CFD techniques and ANSYS CFX software. The study focused on the effects of shroud geometry on the thrust coefficient, pressure coefficient, and mass flow rate. The observation includes the incremental relation between the torque coefficient and the tip speed ratio. The study also concluded that the NACA 5425 showed a high thrust coefficient in comparison to the other two profiles, whereas the NACA 9415 showed a better power coefficient in comparison with the other airfoil shells. A detailed description of the selection of the airfoil profiles could be presented to further validate the reasoning behind the selection of the airfoils. Saleem, [35] also published a performance study on the shrouded turbine with the shroud geometries (NACA 9415, 5415, and 5425). The study concluded that the NACA 9415 has a higher power coefficient in comparison to both the NACA 5415 and the NACA 5425. The study reported a high thrust coefficient in NACA 5415 at a low tip speed ratio followed by NACA 9415 and

NACA 5425, the trend reversed later with the increase in tip speed ratio (TSR). The study also concluded that a pressure fluctuation was observed along the buoyant diffuser at yaw angles (α_{yaw}) of 0^o,5^o,10^o,15^o, and 20^o. Ali [36] conducted a comparison study on the design parameters of the diffuser by using the BEMS (Boundary Element Models) and RANS (Reynolds Averaged Navier Stokes) models for running the CFD simulation at variable wind velocity and TSR and concluded that there is a 21.3 % increase in the power coefficient at the operational altitude of 400 m. Further studies on the computational comparison between BEMS and the RANS CFD models showed that BEMS presented more accurate results when compared with the RANS CFD model though an error percentage of 12.5 % can be observed in the results between the two. The study carried out by Saeed [37] predicted the steady and unsteady aerodynamic performances of the airborne wind turbine system. He utilized the NREL (National Renewable Energy Laboratory) Phase IV rotor at various wind speeds of 7m/s, 10m/s, 15m/s, and 20m/s with a yaw angle of 0^o, 5^o, 10^o, and 15^o at an altitude of 400 m. The study concluded that the unsteady simulation recorded an almost constant torque value with a variation of ±2 Nm, a 17% increase in the torque at 5m/s and the study observed that at higher yaw angles and the unstable pressure distribution along the shell compromises the structural stability of the shell at operating conditions. Samson's [38] study presented a brief description of the buoyant effect of the annular shroud in addition to a comparison study between the utilization of helium and hydrogen gas for the buoyant shell. This study concluded that hydrogen has more transition points when utilized in comparison to helium, with a contradicting conclusion that the safety aspect of hydrogen (flammable) outweighs its economic benefit when compared to helium (noble gas). A detailed analysis with a practical comparison could be presented for a detailed study of the buoyant effect of the shroud in addition to material analysis of the shroud material.

Chapter 3

Methodology

3.1. Introduction:

In this chapter, the theoretical model utilized in the computational analysis of the buoyant turbine system and its input conditions utilized in the Ansys Fluent software for the computational analysis are discussed. The chapter is parted into the following subsections:

a. Design model and properties for the turbine, the shroud, and the full system.

b. The Governing equations, boundary conditions and the mesh dependency characteristics

3.2. Design model and properties:

The buoyant turbine system is an AWT setup that generates electricity by lifting the wind turbine to altitudes where high wind velocity flow is experienced. To generate adequate lift for the turbine to reach higher altitudes, the mass of the turbine is one of the important parameters to be taken into consideration along with the efficiency of the turbine. In this thesis, the Aeolos H 30kW turbine is selected for analysis for its lightweight characteristics. The turbine is a 3-bladed turbine that has an optimal Tip Speed Ratio between 4-5, this factor can be calculated from the number of blades on the selected turbine and is represented by the formula, [39]:

$$\lambda_{opt} = \frac{4\pi}{n_b} \tag{3.1}$$

where, n_b= number of turbine blades, λ_{opt} = Optimal Tip Speed Ratio

The properties of the three-bladed turbine are presented in table 3.1 below, [40]:

Table 3.1. Specifications of the Aeolos H 30kW

Properties	**Value**	**Unit**
Model	Aeolos H 30kW	-
Rotor Speed	90	rpm
Rated Power	30	kW
Material	Fiber E-glass	-

Cut-in Wind Speed	3	m/s
Cut-out Wind Speed	14	m/s
Rotor Diameter	12.8	m
Survival Wind Speed	50	m/s
Overall, Weight	981	kg
Generator Type	Permanent Magnet Generator	-

The turbine blades determine the efficiency at which the turbine can generate electrical energy from wind energy. This is a result of the lift force generated by the turbine blades because of the pressure differences caused by the Magnus effect around the airfoil shaped blades. The profile of the turbine blade utilized in the study is the DU-93-W210 from the DU (Denmark Univeritait) series [16,17]. The profile specifications of the DU93W210 turbine blade can be observed in table 3.2 below:

Table 3.2. Turbine Blade specification

Properties	Value	Unit
Model	DU93-W-210	-
Root Chord	0.703	m
Tip Chord	0.02	m
Twist Angle	17.45	degrees

With the turbine and the turbine blade specifications considered, the computational design model of the turbine is carried out in CATIA V5. In the case of the turbine blade, the profile of DU-93-W210 is taken from an open-source coordinate file published by Perry Roth Johnson [17]. The profile of DU-93-W210 and the 3-D model of the designed turbine can be observed in figures 3.1 and 3.2 below:

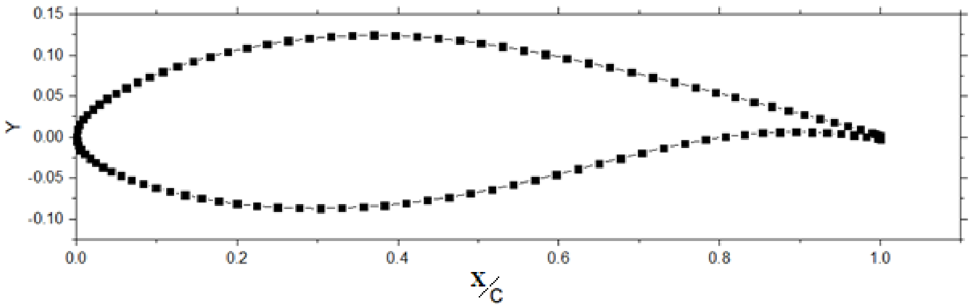

Figure 3.1. DU93-W-210 profile

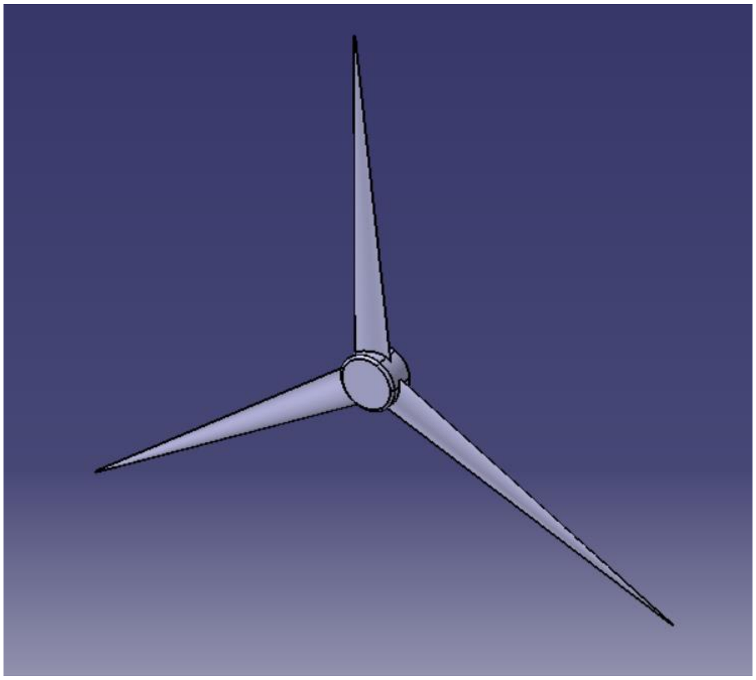

Figure 3.2. Aeolos H 30kW Wind Turbine rotor, (CATIA V5)

Prior to the 1970s, modern wind turbines were manufactured utilizing steel to generate electricity while post 70's manufacturers introduced the composites for their capability to reduce weight and inertia thereby increasing the efficiency. Current turbine blades utilize composite fibers (E-glass) as the standard material for manufacturing turbine blades because of their highly durable characteristics retaining their low-density value [41]. Aeolos H 30kW turbine blades are manufactured of E-glass whose properties can be observed in table 3.3 below [42]:

Table 3.3. Material properties of E-Glass, [42]

Properties	**Values**	**Unit**
density	2550	Kg/m^3
Thermal Expansion	5.0E-09	K^{-1}
Young’s Modulus	8.5E+10	N/m^2
Poisson’s Ratio	0.22	-
Bulk Modulus	5.059E+10	N/m^2
Shear Modulus	3.4836E+10	N/m^2
Tensile Yield Strength	1.95E+09	N/m^2
Compressive Yield Strength	4.0E+09	N/m^2
Tensile Ultimate Strength	2.05E+09	N/m^2
Compressive Ultimate Strength	5.0E+09	N/m^2

The annular shroud employed in this study is a hollow structure utilized to induce an increase in the mass flow rate and wind velocity and also bring about a buoyant effect for lifting the turbine. Before carrying out the computational analysis of the annular shroud, the shroud profile geometry is to be selected and optimized through the performance of both the shroud and the turbine. To conduct the optimization process, the selection criteria for the shroud optimization study of the thesis were initiated with building the shroud using the KT model. In addition to the KT concept study, a side study to determine a NACA airfoil that reflects the properties of the KT profile is also investigated for further insights into the optimization process. In the case of the NACA airfoil, the symmetric airfoil is designed with a thickness ranging from 12%-26% [14] of the chord length for every even positive integer, and the KT study is carried out with the chord length varying from 3m to 15m for every odd positive integer.

The Karman-Trefftz method is a conformal transformation that converts an equation of a circle in a complex plane to an airfoil in a polar/cartesian coordinate system and the complex function instigating the transformation is as represented below [43]

$$w = nb\left[\frac{(z+b)^n+(z-b)^n}{(z+b)^n-(z-b)^n}\right] \tag{3.2}$$

where, w= complex function, b =complex function real constant which is taken as the difference between the radius of the unit circle and the eccentricity within the circle, z= complex number

(and)

$$n = 2 - \frac{\emptyset}{\pi} \tag{3.3}$$

where, ϕ = trailing edge angle, n= exponential constant that relates the trailing edge angle to the complex function ‘w’

The manipulation of the chord length of the mapped airfoil profile depends on two variables: b and the radius of the circle (R) seen in equation 3.2. Since the KT study is an optimized variant of the Joukowsky model, the mapped chord length (ζ) is 2R with ζ a function of the complex real constant b [45]. In other words, by increasing the radius of the circle and by varying the complex function real constant ‘b’, the circle is morphed to the airfoil shape with the leading-edge point and the tailing edge point taken about the eccentricity points of the circle plotted in the complex coordinate. The plots are generated from MATLAB and a sample of the plot derived from the output for the 13m chord length can be observed in figure 3.3 below

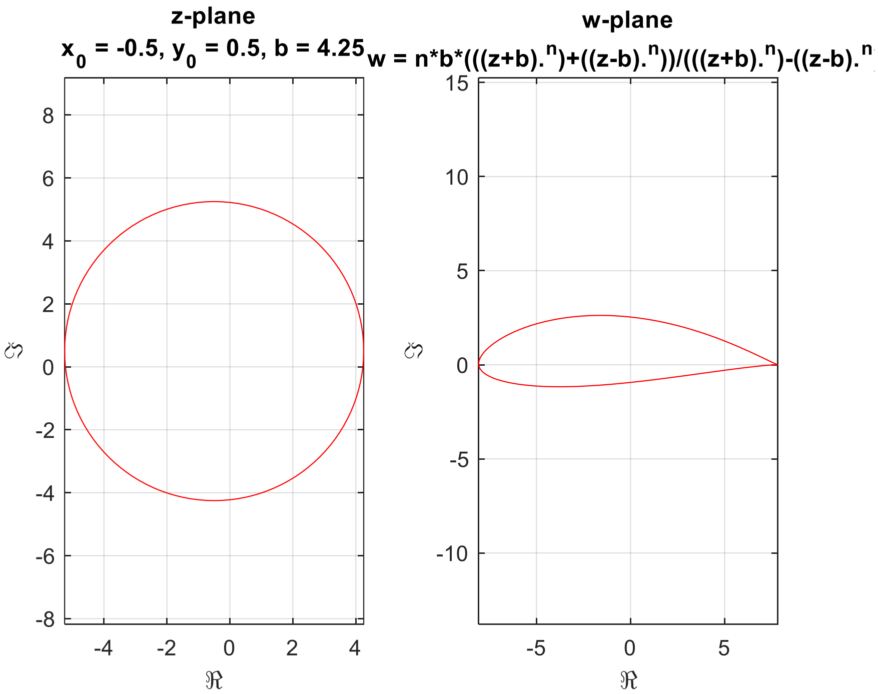

Figure 3.3: KT 13m Chord Length, MATLAB output plots

The history of Karman-Trefftz started with the Joukowski equation below, which was derived by Nikolai Joukowski using the conformal transformation method to derive an airfoil.

$$w = z + \frac{b^2}{z} \tag{3.4}$$

where, w= complex function and z= complex variable

The conformal mapping of Karman-Trefftz works by manipulating real coordinate points in the complex plane with one point about the trailing edge and the other point about the contour of the unit circle in the complex plane. In the case of Joukowski, the trailing edge point creates a differential image function that leads to singularity [45,46]. This made it impractical for the airfoil to be used in the industry. To overcome this issue, Karmann and Trefftz, later on, derived an equation that incorporates a trailing edge angle into the equation of the complex function resulting in a non-zero angle trailing edge which was considered more practical [46].

In the case of the symmetric airfoil, according to Stanford's NACA airfoil data summary, it was stated that the NACA 4 series airfoil is best possible for shroud applications as a result of their good stall characteristics [47], and most of the past studies concluded that the NACA 4 series and 5 series airfoils have better aerodynamic characteristics in comparison to the other airfoils as they are considered in the realm of the thick airfoils which are suitable for such applications. The 4-series study of the symmetric airfoil is carried out for the lower half of the symmetric airfoil to study the flow characteristics of the wind about the airfoil profile. The piecewise equations describing the NACA 4 series airfoil profile are:

$$x_u = C - (y_t).sin\theta \tag{3.5}$$

$$y_u = y_c + (y_t).cos\theta \tag{3.6}$$

$$x_L = C + (y_t).sin\theta \tag{3.7}$$

$$y_L = y_c - (y_t).cos\theta \tag{3.8}$$

where, yc is the maximum camber defined by:

$$y_c = \frac{M}{P^2}.(2PC - C^2) \qquad 0 \le C < P \tag{3.9}$$

$$y_c = \frac{M}{(1-P)^2}.(2PC - C^2 - 2P + 1) \qquad P \le C \le 1 \tag{3.10}$$

With C= Chord Length, P= Position of Maximum Camber and M= Maximum Camber calculated for the airfoil.

The gradient of the max camber is calculated by differentiating y_c as follows:

$$\frac{dy_c}{dC} = \frac{2M}{P^2} .(P - C) \quad 0 \leq C < P \tag{3.11}$$

$$\frac{dy_c}{dC} = \frac{2M}{(1-P)^2} .(P - C) \quad P \leq C \leq 1 \tag{3.12}$$

And the thickness of the airfoil is calculated from the following formula:

$$\mp y_t = \frac{T}{0.2} \left(0.2969\sqrt{C} - 0.1260C - 0.3516C^2 + 0.284C^3 - 0.105C^4\right) \tag{3.13}$$

where, the corresponding constants define the thickness at each node/coordinate defined for the airfoil.

Finally, the angle (ɵ) in equation below is derived to accommodate for the angular variation along the coordinate points of the airfoil giving rise to curved airfoil like profile.

$$\theta = \frac{dy_c}{dx} \tag{3.14}$$

To complete the buoyant annular shroud design, it is 3D modeled using the software CATIA V5. As a result of the implementation of both the Karman-Trefftz Model and the NACA symmetric airfoil model, the Karman-Trefftz profiles are generated using equation and in the case of the NACA symmetric airfoil profile, the coordinates data of the symmetric airfoil profile are generated using the Xfoil software which utilizes the above equations (Eqn 3.5 to 3.14). The representation of both the Karman-Trefftz and the NACA 4 series symmetric airfoil can be seen in figures 3.4 and 3.5 below:

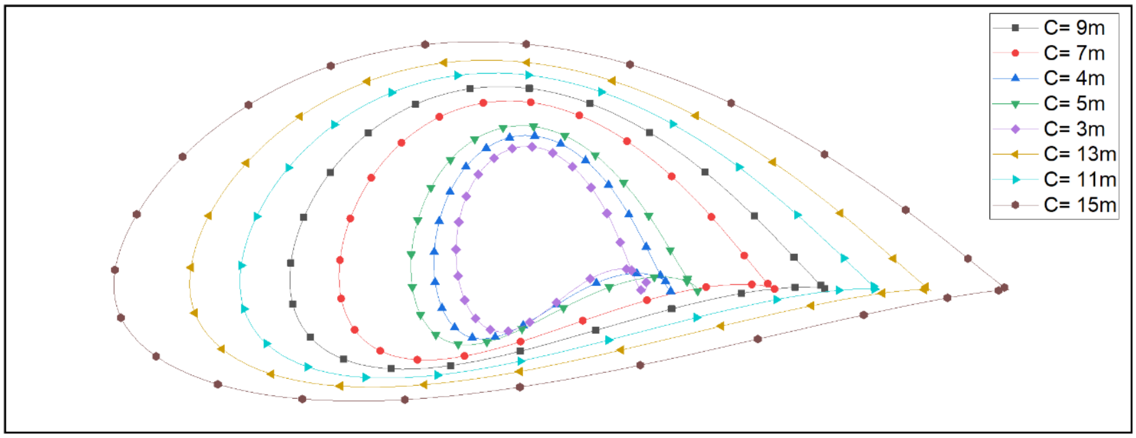

Figure 3.4. Karman-Trefftz Profile Compilation for different chord lengths (C = 3m to 15m)

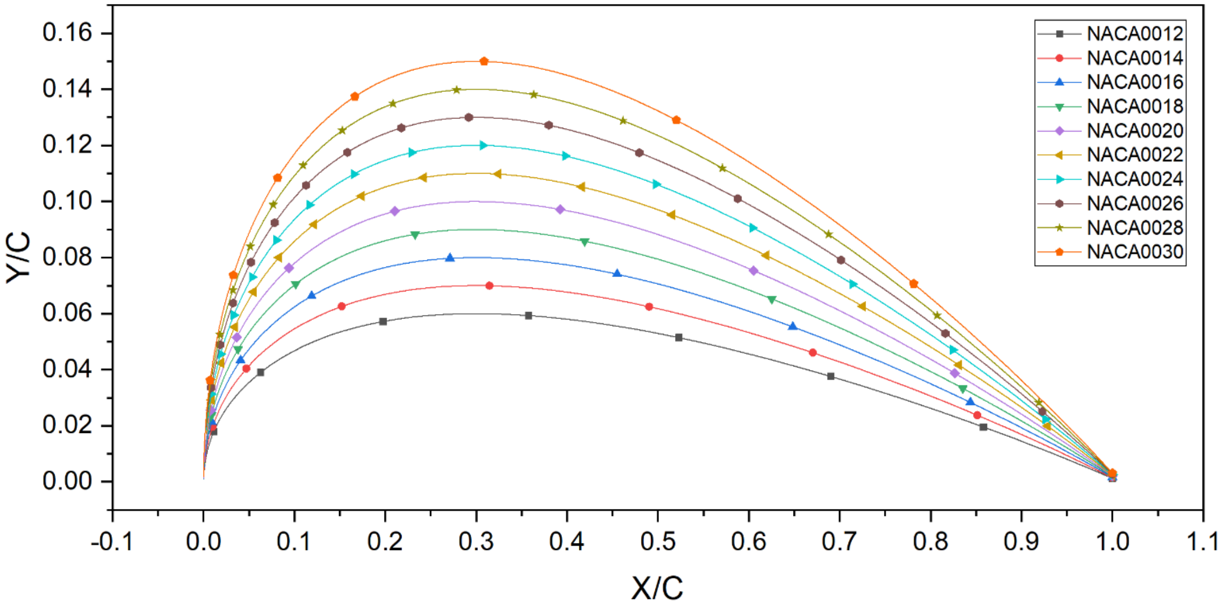

Figure 3.5. Symmetric NACA Profile Compilation for different thicknesses (t = 12% to 30%)

For the purpose of visualization, a representation of the 15m chord length annular shroud geometry designed through CATIA V5 is given in figure 3.6 below:

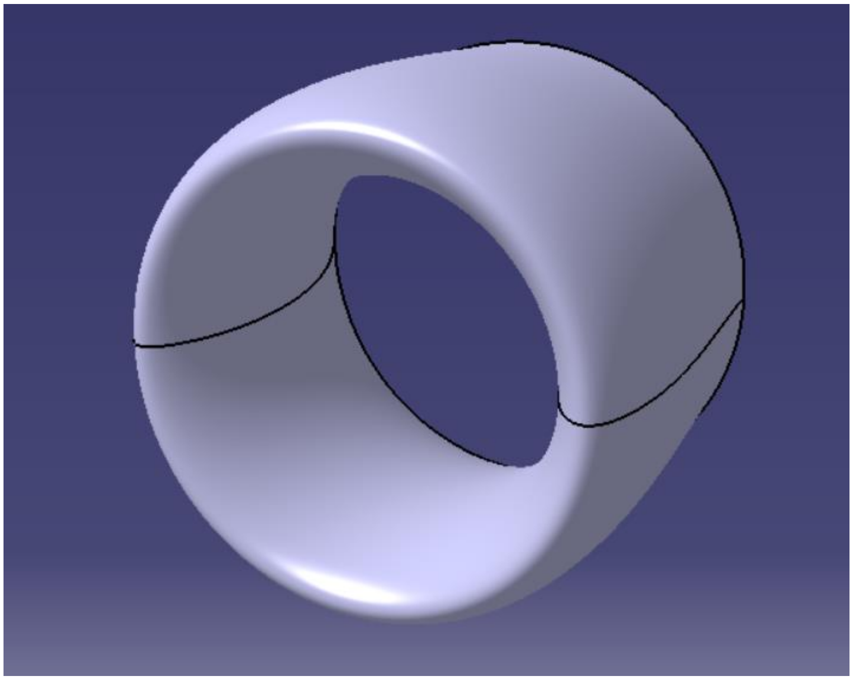

Figure 3.6. C = 15m Karman-Trefftz Annular Shroud

The material of the buoyant shroud is an important factor in the design as it carries the assembly and keeps the form of the shroud. Since the design of the buoyant shroud resembles that of the airships or the blimps, the material utilized there can be incorporated into the buoyant shroud material design. The standard material for the design of the envelopes in blimps and airships are lightweight polymeric materials like mylar, chloroprene, and kevlar for their high tensile strength property to be able to withstand high internal pressure without blowing up. For computational analysis, mylar is chosen for its elastic properties and its properties can be observed from table 3.4:

Table 3.4. Properties of Mylar, [48]

S.NO	Properties	Value	Testing Method	Unit
1	**Density**	1390	ASTM-D1505	kg/m^3
2	**Viscosity**	0.56	ASTM-D4603	dl/g
3	**Surface Roughness**	38	Optical Profilometer	nm
4	**Yield**	21000	-	in^2/lb
5	**Tensile Strength**	28000	ASTM-D882	psi
6	**Modulus**	710000	ASTM-D882	psi

7	**Elongation**	115	ASTM-D882	%

3.3. The governing equations and boundary conditions:

In this section, the governing equations and boundary conditions describing the problem physics are presented, followed by the computational scheme used to solve them. A standard CFD study employs the mass, energy and momentum conservation equations. In this thesis, considering the effects of the boundary layer flow and the turbine simulation with an operating altitude ranging from 18m to 200 m above the earth’s surface, eddy viscosity models are utilized for the simulation of the buoyant system and the turbine along with the applicable boundary conditions that are defined in the following sections.

The RANS equations are time-averaged equations that define the turbulent flow of fluids. The RANS equation is built upon the concept of the Reynolds decomposition of each quantity into its averaged and fluctuating components [49]. The simulation is carried out in a 3D polar coordinate and 2D cartesian coordinate system for the performance study and the shroud optimization study respectively. The RANS momentum equations for both the polar and the cartesian coordinate and the continuity equation are given below:

Cartesian Coordinates:

$$X - \ momentum\text{:}\ \frac{\partial U_x}{\partial t} + \left[U_x \frac{\partial U_x}{\partial x} + U_y \frac{\partial U_x}{\partial y}\right] = -\frac{1}{\rho}\frac{\partial P}{\partial x} + \vartheta_l \left[\frac{\partial^2 U_x}{\partial x^2} + \frac{\partial^2 U_x}{\partial y^2}\right] - \rho\underline{u'v'} \qquad (3.15)$$

$$Y - \ momentum\text{:}\ \frac{\partial U_y}{\partial t} + \left[U_x \frac{\partial U_y}{\partial x} + U_y \frac{\partial U_y}{\partial y}\right] = -\frac{1}{\rho}\frac{\partial P}{\partial y} + \vartheta_l \left[\frac{\partial^2 U_y}{\partial x^2} + \frac{\partial^2 U_y}{\partial y^2}\right] - \rho\underline{u'v'} \qquad (3.16)$$

$$Continuity\ Equation\text{:}\ \left[\frac{\partial U_x}{\partial x} + \frac{\partial U_y}{\partial y}\right] = 0 \qquad (3.17)$$

Cylindrical Coordinates:

$$Continuity\ Equation\text{:}\ \frac{1}{r}\frac{\partial (rU_r)}{\partial r} + \frac{1}{r}\frac{\partial (U_\theta)}{\partial \theta} + \frac{\partial (U_z)}{\partial z} = 0 \qquad (3.18)$$

$$r - \ momentum\text{:}\ \frac{\partial U_r}{\partial t} + \left[U_r \frac{\partial U_r}{\partial r} + \frac{U_\theta}{r}\frac{\partial U_r}{\partial \theta} + U_z \frac{\partial U_r}{\partial z}\right] = -\frac{1}{\rho}\frac{\partial P}{\partial r} + \vartheta_l \left[\frac{1}{r}\frac{\partial^2 U_r}{\partial r^2} + \frac{1}{r^2}\frac{\partial^2 U_r}{\partial \theta^2} + \frac{\partial^2 U_r}{\partial z^2} - \frac{2}{r^2}\frac{\partial U_\theta}{\partial \theta}\right] - \rho\underline{u'v'} \qquad (3.19)$$

$$\theta - \ momentum\text{:}\ \frac{\partial U_\theta}{\partial t} + \left[U_r \frac{\partial U_\theta}{\partial r} + \frac{U_\theta}{r}\frac{\partial U_\theta}{\partial \theta} + U_z \frac{\partial U_\theta}{\partial z}\right] = -\frac{1}{\rho}\frac{\partial P}{\partial \theta} + \vartheta_l \left[\frac{1}{r}\frac{\partial^2 U_\theta}{\partial r^2} + \frac{1}{r^2}\frac{\partial^2 U_\theta}{\partial \theta^2} + \frac{\partial^2 U_\theta}{\partial z^2} + \frac{2}{r^2}\frac{\partial U_r}{\partial \theta}\right] - \rho \underline{u'v'} \tag{3.20}$$

$$Z - \ momentum\text{:} \frac{\partial U_z}{\partial t} + \left[U_r \frac{\partial U_z}{\partial r} + \frac{U_\theta}{r}\frac{\partial U_z}{\partial \theta} + U_z \frac{\partial U_z}{\partial z}\right] = -\frac{1}{\rho}\frac{\partial P}{\partial z} + \vartheta_l \left[\frac{1}{r}\frac{\partial^2 U_z}{\partial r^2} + \frac{1}{r^2}\frac{\partial^2 U_z}{\partial \theta^2} + \frac{\partial^2 U_z}{\partial z^2}\right] - \rho \underline{u'v'} \tag{3.21}$$

where, u',v' = Fluctuating velocities, $\frac{\partial U_x}{\partial t}, \frac{\partial U_y}{\partial t}, \frac{\partial U_r}{\partial t}, \frac{\partial U_\theta}{\partial t}\ and\ \frac{\partial U_z}{\partial t}$ = Rate of change of velocities, ϑ_l = Fluid viscosity, $\frac{\partial P}{\partial x}, \frac{\partial P}{\partial y}, \frac{\partial P}{\partial r}, \frac{\partial P}{\partial \theta}$, and $\frac{\partial P}{\partial z}$ = Pressure Gradients, and r= radial distance

The Reynolds decomposition led to the introduction of the Reynolds stress term which is difficult to solve as a result of its fluctuating nature. To solve the RANS momentum equation, the eddy viscosity models are introduced to solve the Reynolds stress term. The different eddy viscosity models present are the k-ε model, k-ω model, k-ω SST model, Spalart-Allmaras model, and Smagorinsky model, [50].

To model and solve the turbulent eddy generation and dissipation characteristics in a turbulent boundary layer, the first model introduced by Prandtl's called the mixing length model presented results that defined the formation and dissipation of the eddies within the boundary layer. To solve for the eddy viscosity in the RANS equation, this model presented correlates the eddy viscosity to the mixing length, where the mixing length is defined as the size of the eddy within the observable layer, [51], as per the following model.

$$l_m = \kappa y \tag{3.22}$$

$$\mu_t = \rho (l_m)^2 \left|\frac{dU}{dx}\right| \tag{3.23}$$

where, κ (Von Karman's Constant) = 0.41, y =vertical distance from the wall, l_m = Mixing length distance, dU/dx = Velocity gradient about the cartesian coordinate and μ_t = Turbulent Eddy Viscosity

The mixing length model concluded that the mixing region as a result of the eddy generation is observed to be larger further away from the wall boundary in comparison to the near wall where the eddies are smaller as a result of the viscous damping effects within the viscous sublayer. The only concern presented with the model is its inability to explain the dispersion of the eddy from the wall as it presents the state of the eddy at a fixed distance from the wall. Since turbulent effects flow is diffusible and convective, the mixing length model was further updated by introducing two transport equations; the turbulent kinetic energy (k), equation 3.24, which is studied through the velocity fluctuations in the turbulent region, and the eddy dissipation rate (ε), equation 3.25, which is used to study the eddy diffusion from the wall boundary layer, [52,53].

$$\frac{\partial(\rho k)}{\partial t}+\frac{\partial(\rho k u_i)}{\partial x_i}=\frac{\partial}{\partial x_j}\left[\frac{\mu_t \partial k}{\sigma_k \partial x_j}+\mu\frac{\partial k}{\partial x_j}\right]+G_k-\rho\varepsilon \tag{3.24}$$

$$\frac{\partial(\rho\varepsilon)}{\partial t}+\frac{\partial(\rho\varepsilon u_i)}{\partial x_i}=\frac{\partial}{\partial x_j}\left[\frac{\mu_t \partial\varepsilon}{\sigma_\varepsilon \partial x_j}+\mu\frac{\partial\varepsilon}{\partial x_j}\right]+C_{1\varepsilon}\frac{\varepsilon}{k}(G_k)-C_{2\varepsilon}\rho\frac{\varepsilon^2}{k} \tag{3.25}$$

where, u_i = represents velocity component in the corresponding direction

$$G_k \text{ = Generation of Turbulent Kinetic Energy} = G_k = -\rho\underline{u'v'}\frac{\partial U_i}{\partial x_j} \tag{3.26}$$

μ_t= turbulent viscosity, σ_k, σ_ε , $C_{1\varepsilon}$,and $C_{2\varepsilon}$ = Empirical constants, k =Turbulent Kinetic Energy, ε = Eddy Dissipation rate

The main drawback of using the k-ε model ($y+ < 30$) is its inaccuracy in computing turbulence in the viscous boundary layer ($y+ <5$) where the turbulent dissipation due to viscosity is high.

The analytical studies of most external aerodynamics problems are carried out in the turbulent regions of the boundary layer and most of the studies employ the k-ω SST, k-ω, and the Spalart-Allmaras models. The study conducted by Peerakit Kekina. et.al and Douvii C Eleni presented a comparative analysis between the Spalart-Allmaras, RNG k-ε, and the k-ω SST turbulence model through an aerodynamic analysis of the NACA 0012 airfoil for AOA ranging from 0^o to 20^o using OpenFOAM. The Cl (lift coefficient) and Cd (drag coefficient) for high and low Reynolds numbers were compared with the experimental data derived from a wind tunnel. The study concluded that the Spalart-Allmaras and the k-ω SST model presented results closer to the experimental data in comparison to the k-ε model for AOA 0^o to10^o whereas the RNG k-ε model presented marginally better results for AOA ranging from 11^o to 20^o, [54,55].

On account of the past studies and their validation against the experimental data, the k-ω SST model was chosen for the analysis in the current thesis. The k-ω SST model was utilized to study the pressure and the velocity gradient along the shroud as a result of its ability to explain both the effect of near-wall turbulence as a result of viscous damping and the turbulent kinetic energy effects away from the wall. This model aids in numerically calculating and analyzing the turbulence till the viscous boundary layer using the k-ω equations (turbulent kinetic energy (3.27) and specific dissipation rate (3.28)) and then is blended to the k-ε model (3.25) and (3.26) where the turbulent dissipation is low as a result of lack of influence from viscosity, the transition is carried out through a blending function F_1, [52,56,57].

$$\frac{\partial(\rho k)}{\partial t} + \frac{\partial(\rho k u_i)}{\partial x_i} = \frac{\partial}{\partial x_j}\left[\mu_k k \frac{\partial k}{\partial x_j}\right] + G_k - \beta^* \rho \omega k \tag{3.27}$$

$$\frac{\partial(\rho \omega)}{\partial t} + \frac{\partial(\rho \omega u_j)}{\partial x_j} = \frac{\partial}{\partial x_j}\left[\mu_{\omega i} \omega_i \frac{\partial \omega}{\partial x_j}\right] + 2\rho(1 - F_1)\sigma_{\omega i}\frac{1}{\omega}\frac{\partial k}{\partial x_j}\frac{\partial \omega}{\partial x_j} \tag{3.28}$$

where, ω = Specific Eddy Dissipation Rate

F_1 = Blending Function

μ= Dynamic Viscosity

$\sigma_{\omega i}$, σ_{ki}, β^* and β= empirical constants that close the k-ε (i=2) and the k-ω (i=1) equations.

The allocation of boundary labels to both the shroud optimization model and the system model is the first stage of the boundary condition allocation methodology. The inlet, outlet, and wall symmetry are the allocated boundaries for the closed enclosure designed for the model, whereas the wall is defined for the analyzing model located within the closed enclosure. The representation of the model and its allocated boundary can be observed in figure 3.7 A, B1 and B2 below:

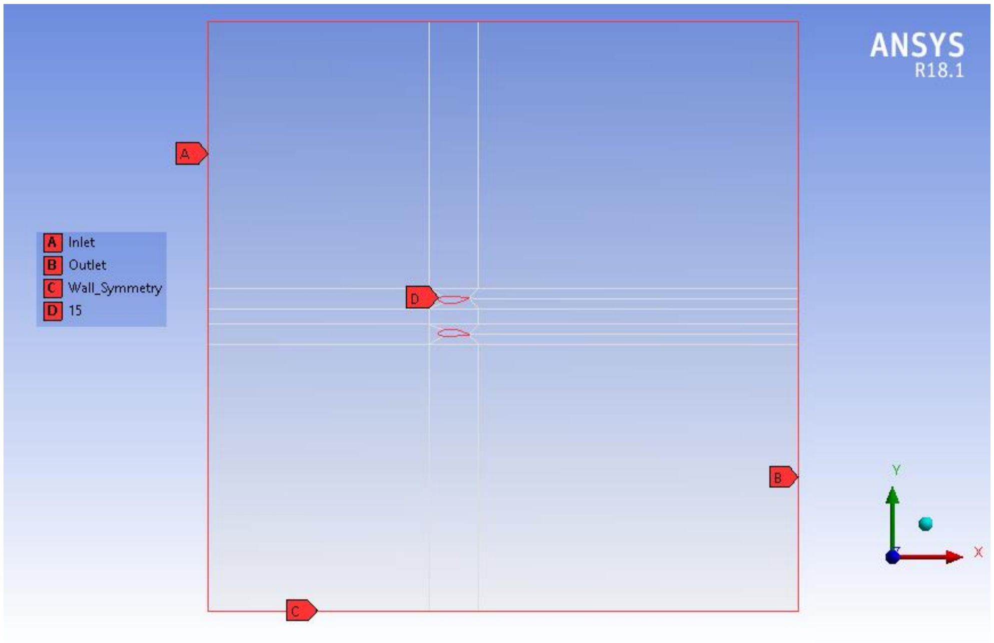

(A) Shroud model boundary label, KT profile, chord length = 15m

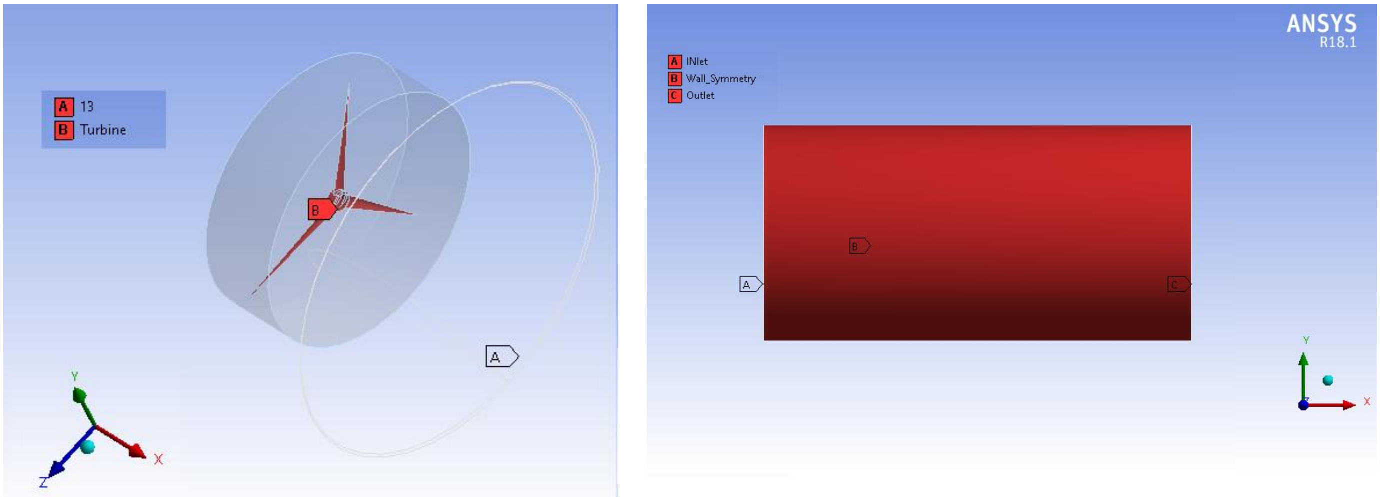

(1) Turbine and shroud model

(2) Enclosure model

(B) System model

Figure.3.7. Boundary allocation for the shroud and system models

From the figure above, it can be seen that a small cylindrical domain created around the turbine model, this is termed as the rotor domain where the designed 3D turbine model exhibits a rotational moment relative to the rotor domain when carrying out the performance analysis. The parameter associated with the rotation of the rotor domain is the turbine RPM (Rotations Per Minuite). The RPM is calculated from the wind speed and the tip speed ratio. To account for the variable RPM as a result of the variable wind speed, the rpm is calculated using the TSR equation below, [39]:

$$\lambda = \frac{\omega_N . r}{U_{wind}} \tag{3.29}$$

where, r = swept area radius, λ = Tip Speed Ratio, ω_N= Angular Velocity, and U_{Wind} = Wind Velocity

To derive continuous computational results of the targeted parameters, the setting of the interface boundary condition is observed and set for the computational simulation, the mesh interface representation within the system space can be observed in figure 3.8 below. The next stage is the setting of the type of boundary for each labeled surface on the model which can be observed from both figure 3.8, and table 3.5 below:

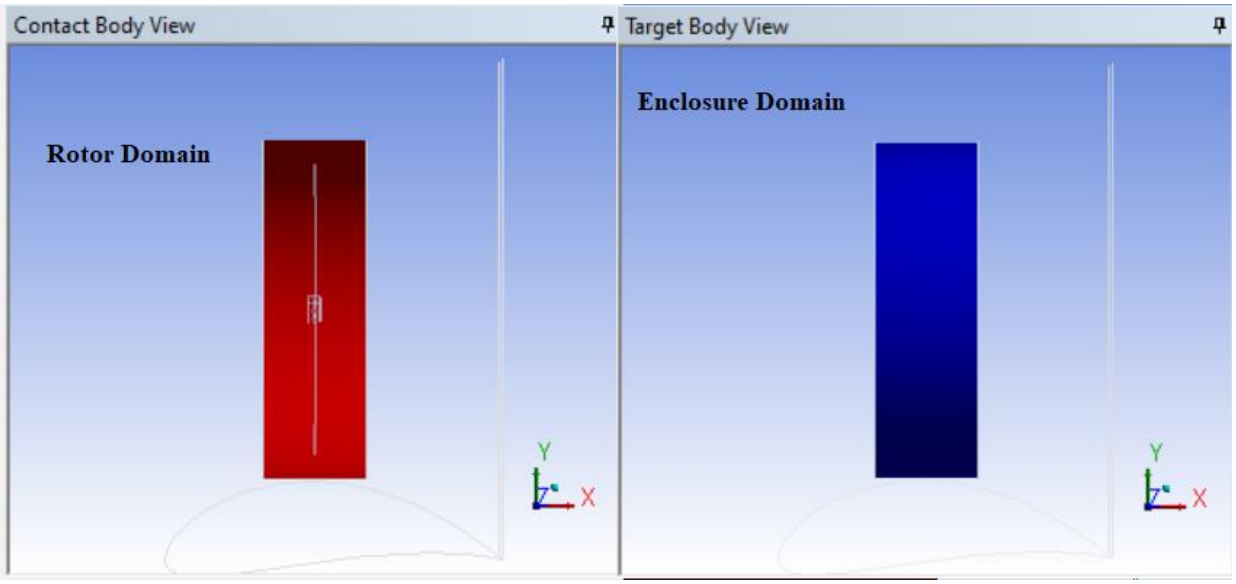

Figure 3.8. Interface zone representation in performance model

Table 3.5. Allocation of the type of boundary to the allocated boundary

Boundaries		Type of Boundary
Inlet		Velocity Inlet
Outlet		Outflow
Turbine and Annular Shroud		Wall
Wall		Wall-Symmetry
Rotor Domain	Inlet_Interface_Rot	Interface Zone
	Outlet_Interface_Rot	
	Wall_Interface_Rot	
Enclosure Domain	Inlet_Interface_Encl	Interface Zone
	Outlet_Interface_Encl	
	Wall_Interface_Encl	

The inlet velocity is taken at 8m/s for high altitude buoyant shroud system with the pressure of the closed system taken as 102500 Pa. Since the flow is incompressible, the operating pressure for the computational analysis is set to 0 and the gauge pressure is set to the atmospheric pressure:

$$P_{total} = P_{gauge} + P_{operating} \tag{3.30}$$

The initialization of the computational analysis is from the inlet and to reduce the computational cost the simple method of pressure-velocity coupling is employed. To accommodate for adequate convergence time, the simulation is set to run for 2000 iterations under the static condition since the results studied in this section present a single final result. In the case of the 2D shroud optimization analysis, the coefficient of drag was taken to observe the convergence of the result while in the case of the 3D performance study, the moment about the rotational axis is taken for the same observation, which can be observed from the plots in figures 3.9 (a) and (b) below:

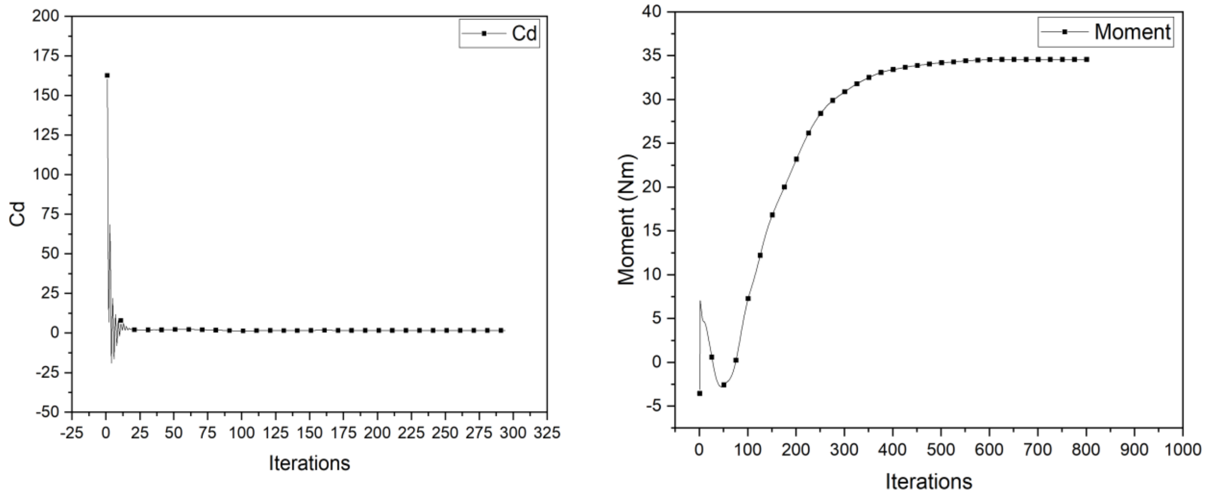

(a) 2D shroud Optimization Study, KT Chord Length = 15m

(b) 3D Performance Study, Bare Turbine, moment about the rotational axis

Figure.3.9. Convergence trend of computational result for data extraction, 2D shroud optimization analysis and 3D performance analysis

Figures 3.10-A to C demonstrates the mathematical model domain with both the shroud and turbine located in the center. The domain is cylindrical with a side length of 20D, where D is the diameter of the shroud throat [35]. The dimensions of the enclosure are taken as such to eliminate the effect of the enclosure boundary wall on the turbine-shroud flow characteristics.

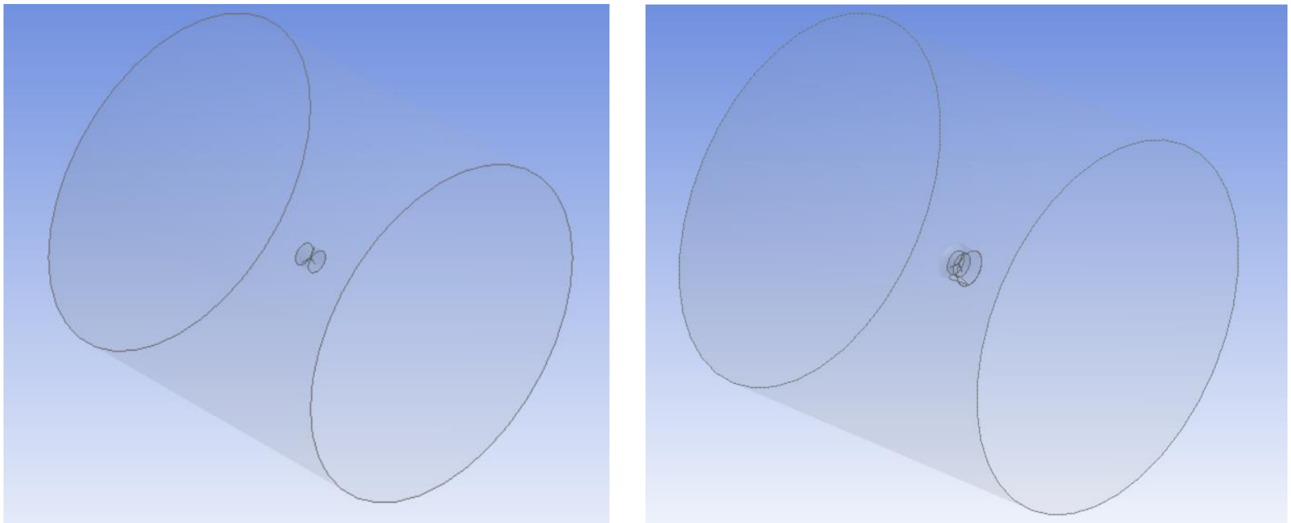

A) Full Model without Annular Shroud **B) Full Model with Annular Shroud**

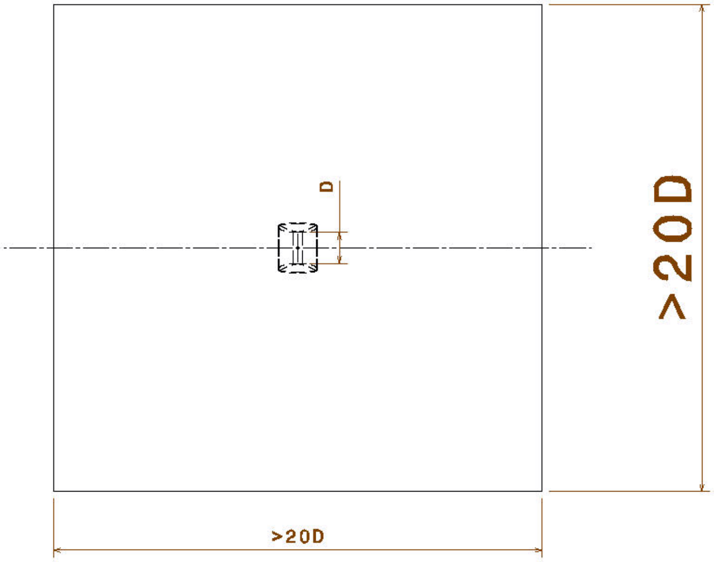

C) Dimensional Draft of the computational domain.

Figure.3.10. The computational domain representation of the Buoyant Turbine System

The mesh in computational simulations is defined as the discretization of the domain into multiple subdomains called cells or elements. The meshing procedure is carried out to improve the computational accuracy and optimize the computational time. The different mesh types are classified based on the type of domain specified by the user; either 2-D or 3-D and its classification can be seen from figure 3.11 below.

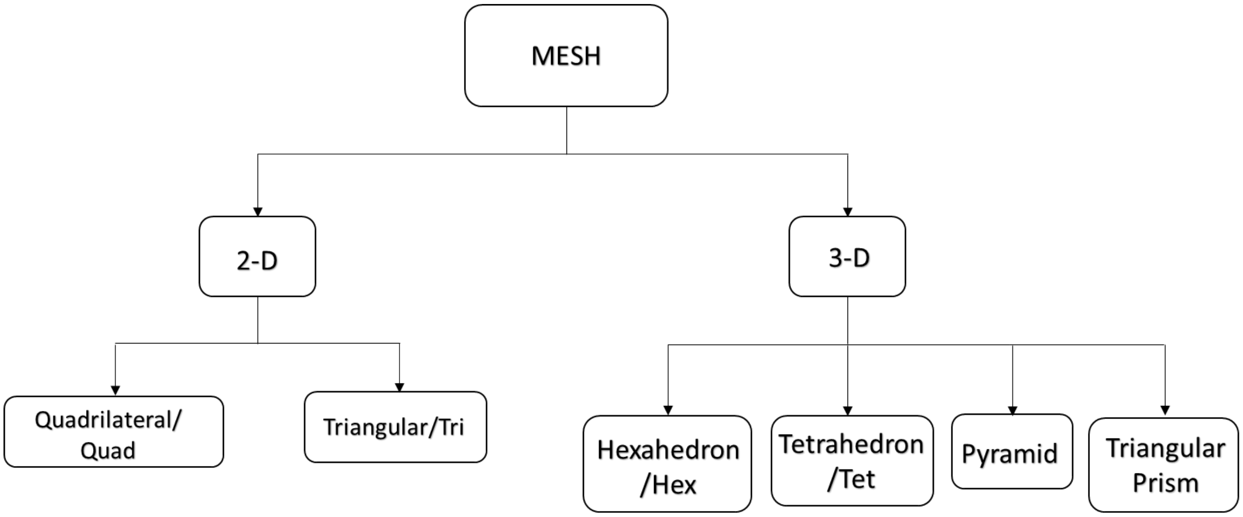

Figure 3.11. Mesh Classification

The determination of the optimum mesh is based on the number of elements and nodes the domain is discretized into. The accuracy of the results is determined by the optimum mesh size and the optimum mesh size is determined by the convergence of the solution where the computational results become independent of the mesh size. The current thesis runs computational analysis for the shroud optimization study which is a 2D study and the performance analysis of the turbine which is a 3D study because of the 3rd dimensional rotational moment required for visualization of the turbine simulation.

In the case of the shroud optimization study, an O-grid type meshing method is utilized for the airfoil analysis for a uniform and structured distribution of quadrilateral /rectangular mesh elements along the domain. The quadrilateral mesh type for the discretization of the model is carried out with a bias factor value set to 5 and the number of division values is presented in table 3.6 and figure 3.12 below, [58]. The bias factor is an inflation factor that is directly related to the growth rate and the number of divisions an edge is discretized into, which can be seen from the equation below.

$$bf \;= r^{n_d - 1} \tag{3.31}$$

Where, bf =bias factor, r = growth rate and n_d = number of divisions

The hard bias option is chosen to retain the number of divisions set by the user for the meshing process. The representation of the mesh can be observed in figure 3.13 below. The shroud optimization model is discretized into 206341 nodes and 205372 elements.

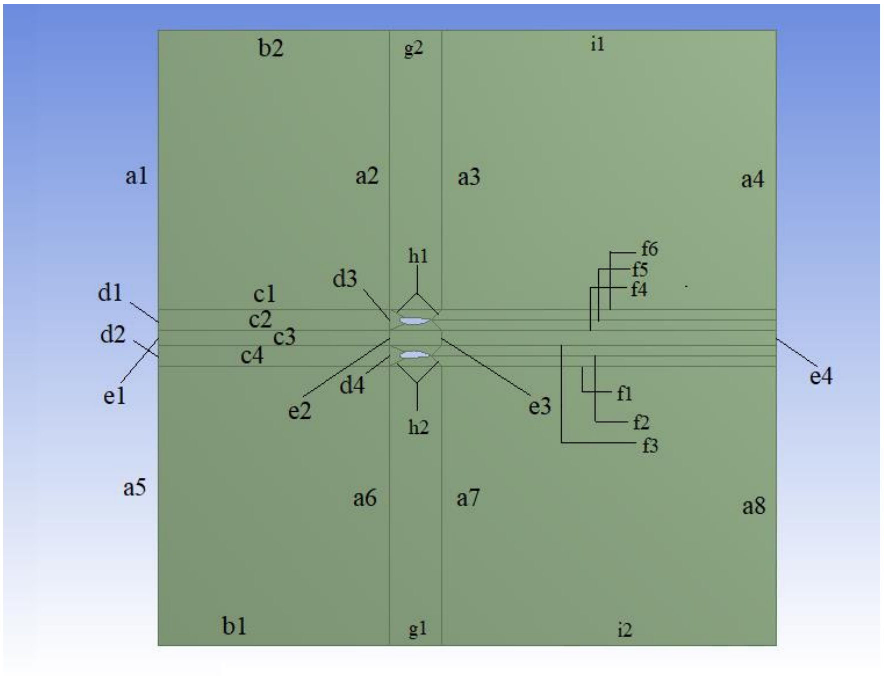

Figure 3.12. Edge Definition of Shroud Optimization Study Model

Table 3.6. Number of Divisions, Edge Length, Bias-Type, and Bias Factor

S.No	Edge label	No of Divisions	Bias Factor	Bias Type
1.	a1-a8	100	5	- — —— — -
2.	c1-c4	100	5	—— — - -
3.	d1-d4	20	-	-
4.	b1, b2	100	-	-
5.	e1-e4	50	-	-
6.	f1-f6	500	5	- - — ——
7.	g1, g2	100	-	-
8.	h1, h2	10	5	- - — ——
9.	i1, i2	500	-	-

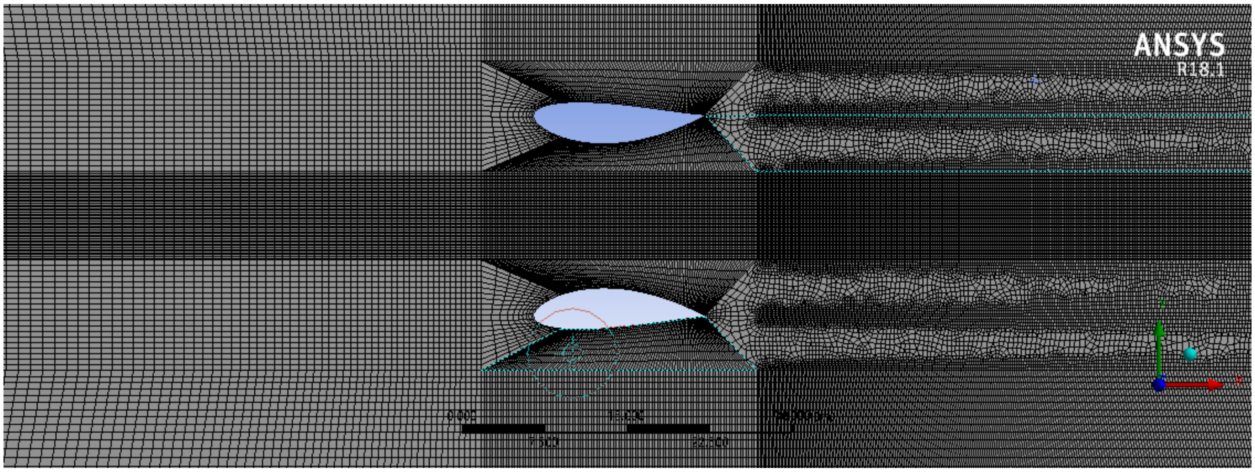

Figure 3.13. Shroud Optimization Study Model Mesh

For the performance study of the buoyant turbine system with a full 3D model of the setup, the tetrahedral mesh methodology was employed for the study. A fine mesh structure with an inflate growth rate of 1.15 resorts for the mesh of the full model. To determine the approximate mesh element size for both the full model with and without the annular shroud, the mesh independent study has been carried out with the reference parameter as the torque and the power of the turbine. The torque and power are chosen since the manufacturer performance of the industrial turbine used in this study is reported using the generated torque and power, [42]. The simulation for the mesh independence study was carried out with a wind velocity of 14m/s and rpm of 90. The turbine power equation utilized for the mesh independent test is as follows:

$$P_{turbine} = \frac{2 * \pi * N * T_{torque}}{60} \tag{3.32}$$

where, T_{torque} = Mechanical Torque of the turbine (Nm), N= Rotational Speed of the turbine (rpm), and $P_{turbine}$ = Turbine Power

The mesh dependency results are shown in tables 3.7 and 3.8**:**

Table 3.7. Mesh Independence Study for a system without annular shroud: Bare Turbine

Elemental Size (mm)	No of Nodes	No of Elements	Torque (N-m)	Power (W)	Variation
25	1177555	849858	1259.21	11867.7	
20	1431677	1035020	1392.58	13124.7	0.09577
15	1948488	1411058	1728.58	16291.4	0.19437

10	2672460	1937749	2189.41	20634.7	0.21048
7.5	3711676	2693576	3008.65	28355.8	0.27229
7	3940707	2860104	3135.12	29547.8	0.04033
6.5	4200607	3048982	3284.1	30951.9	0.04536
6	4495316	3263436	3342.06	31498.1	0.01734
5.5	4835766	3510968	3470.49	32708.5	0.03700
5	5216413	3787498	3644.37	34347.3	0.04776
4.75	5433280	3945213	3651.79	34417.3	0.00201
4.5	5661411	4111159	3686.16	34741.2	0.00932
4.25	6534596	4744197	3992.42	37627.6	0.07671
4	6885450	4998929	4008.01	37774.6	0.00388
3.75	7268102	5276553	4076.77	38422.6	0.01686
3.5	7686686	5580822	4165.14	39255.5	0.02121
3.25	8151840	5918509	4147.64	39090.5	0.00421
3	8661155	6288341	4219.56	39768.4	0.01704
2.75	9237035	6706719	4314.54	40663.5	0.02202
2.5	10163183	7379462	4298.54	40512.7	0.00372
2.25	10619970	7711306	4274.75	40288.5	0.00556
1.5	15575024	11309396	4314.7	40665.1	0.00926

Table 3.8. Mesh Independence Study for a system with annular shroud: Shrouded Turbine

Elemental Size (mm)	No of Nodes	No of Elements	Torque (N-m)	Power (W)	Variation
2.5	1536632	1030361	5971.42	56279.3	
2.25	1573898	1055302	6023.27	56767.9	0.008608
2	1890450	1270187	6135.97	57830.1	0.01836
1.75	1988798	1336553	6160.87	58064.8	0.00404

1.5	2094371	1408006	6047.68	56998.0	0.01459
1.25	2203385	1481654	6316.87	59535.0	0.04261
1	2819423	1897921	6139.84	57866.6	0.02883
0.75	3189098	2146669	6175.83	58205.8	0.00582
0.5	4545307	3058649	6170.18	58152.3	0.00091
0.25	7079742	4751081	6162.95	58084.4	0.00117

The above listed data is also plotted in figures 3.14 and 3.15 of the tabular data in tables 3.7 and 3.8 below. From the plots, it was concluded that the suitable mesh elemental size for the model setup without the annular shroud was around 2.1-1.25 mm whereas in the case of the model with the annular shroud, the elemental size was 0.75-0.25mm. In the case of the independence test for the annular shroud, the analysis was started from the mesh size 2.25mm to effectively present the eventual large variations which will be observed before the starting mesh size and we can observe that the mesh is reaching convergence from 1mm.

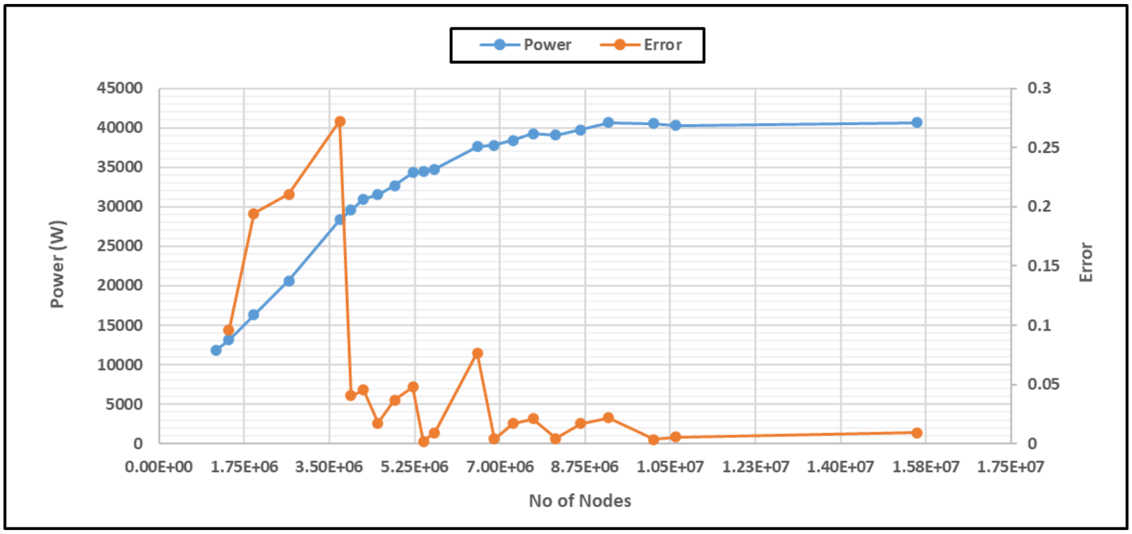

Figure 3.14. Grid Independence Test: System without Annular Shroud

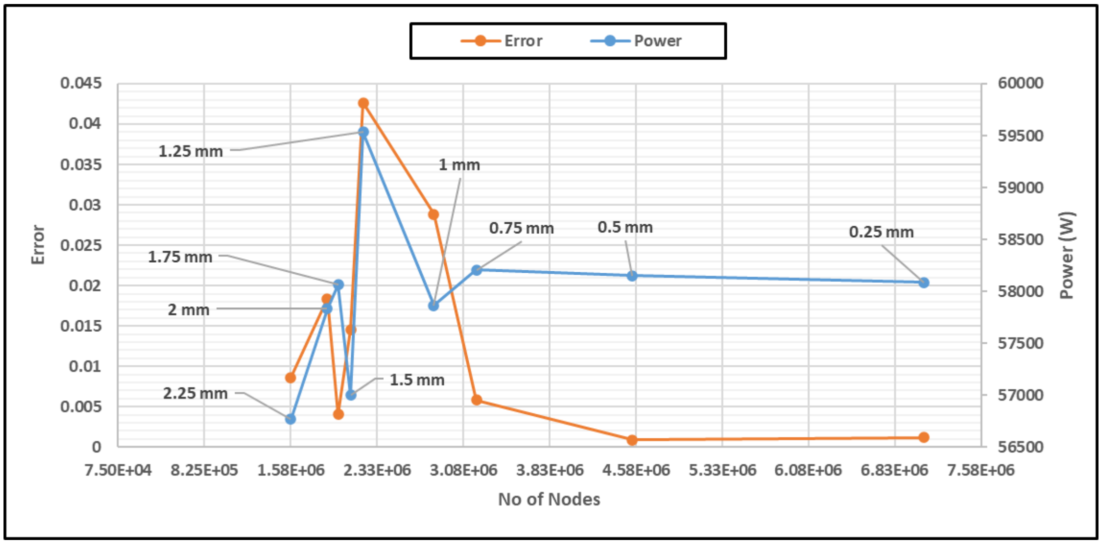

Figure 3.15. Grid Independence Test: System with Annular Shroud

The visualization of the mesh for the annular shroud system seen from figure 3.16 below:

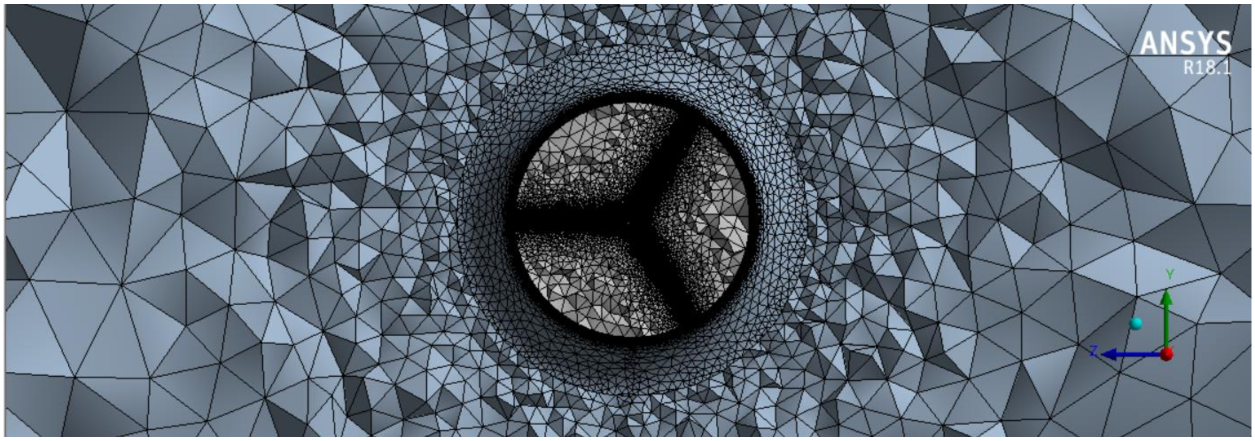

Figure 3.16. Annular shroud system model mesh

Chapter 4

UAE wind data modeling

4.1 Introduction

This chapter looks at the available wind data for the UAE and attempts to correlate wind speed and altitude reaching heights of around 200 m above the earth's surface. It contains two subsections; the first examines the ABL models and the second searches for relatively high potential wind localities in the region based on the 10 m wind map plotted using the ArcMap 17.1 and UAE meteorological data gathered from the references, [59,60,64].

4.2. Altitude-Velocity correlations

The increase in the velocity with the increase in altitude is the initial factor to study when it comes to research pertaining to the analysis of the high-altitude buoyant wind turbine technology. The cumulative ABL is stratified into a different atmospheric layer with the boundary layer extending up to the troposphere. Multiple past studies have stated that the ABL thickness extends vertically from 0.5 km to 2 km from the surface of the earth [61]. The atmospheric boundary layer is influenced by multiple factors including the roughness length of the earth's surface, the temperature, pressure, and density variation with altitude [61].

To effectively define the conditions of the atmosphere and infer the velocity profile at different altitudes, two models were suggested, the power law and the log law. The power law was initially suggested by Menuicci, [25] when he first observed an inaccuracy in applying the 1/7th law of the wall to correlate wind velocity and altitude. The inaccuracy in the study was observed in relation to the ABL thermal stratification which was not included in the analysis. A review study conducted by Henessy, [62] elaborated that the height of the surface roughness of the terrain dictates the usage of the log law or the power law. It was stated that the power law is suitable up to a few meters from the roughness height [25]. The readings from the thermal anemometer and the calculated data showed a large error % when compared with each other through a regression analysis. As a result, Menicucci suggested the following model that relates velocity and altitude:

$$\frac{V}{V_o} = \left(\frac{H}{H_o}\right)^{\propto} \tag{4.1}$$

where, V = Estimated Velocity (m/s) at the target height H (m), V_o = Reference Velocity (m/s), H_o = Reference Height (usually= 10m), and α = Friction Coefficient given by equation 2.3 above.

The log law is the second equation that was derived subsequently in the same era. The only variation that can be observed is the utilization of the roughness length parameter, (Zo), which can be described as the roughness of the terrain which influences the velocity profile relation. It was stated that the roughness length is independent of altitude while the friction coefficient defined in the power law is highly dependent on altitude. The log law can be represented as follows [26]:

$$\frac{V}{V_o} = \frac{ln\left(\frac{H}{Z_o}\right)}{ln\left(\frac{H_o}{Z_o}\right)} \tag{4.2}$$

where, Zo = Roughness Length

This section presents a comparative study between the log law and the power law to determine the suitable altitude model that will aid in determining the wind profile of the ABL for the UAE. This is carried out by studying Davenport’s roughness length classification and determining the roughness parameter that pertains to the terrain of the region [26]. The resulting velocity profile derived from the log law and the power law utilizing the roughness and the friction parameters is compared with each other. The study is concluded through an auxiliary study that compares the results derived from the altitude model with the meteorological data published by the UAE government [59,60]. For the calculation, Dubai (UAE), is taken as the region to be analyzed. To compare the power law and the log law, the terrain roughness and the friction parameter is taken for the terrain of the open area with houses, tall shrubs and bushes, and some trees. This terrain is selected since out of 4114 km2 of land area, Dubai land usage has reached about 61900 donums, which brings to about 98.1% of Dubai an open area with shrubs and trees. This explains the average wind velocity value published from satellite data in the government sites mentioned above [63]. The roughness parameter table and the plotted comparison between the power and the log law are presented below in table 4.1 and figure 4.1:

Table 4.1. Roughness length and friction coefficient parameter of open area

Terrain Type (Davenports Classification)	**Friction Coefficient (α)**	**Roughness Length (Zo)**
Open Area with shrubs and bushes and a few establishments	0.3	0.2

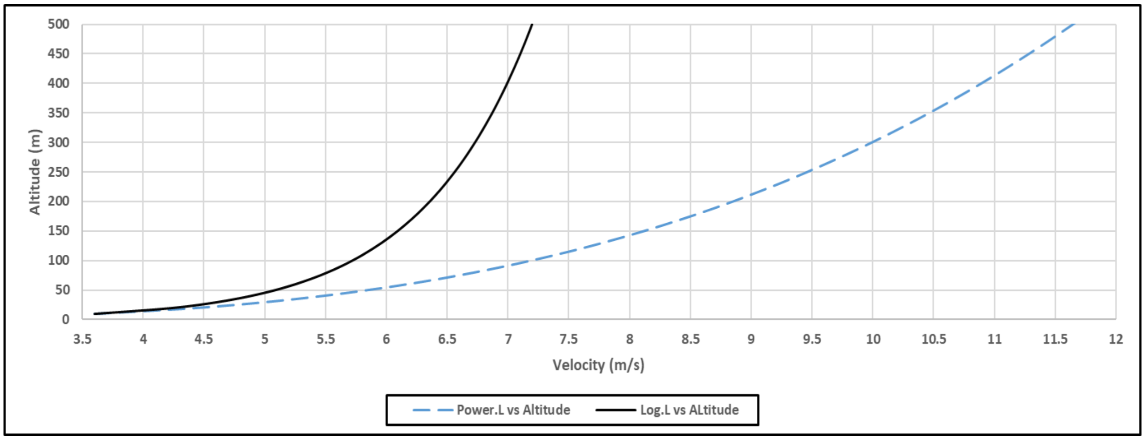

Figure 4.1. Comparison between the power law and the log law

From the plot above we can infer that the logarithmic law delivers a more realistic results in comparison to the power. This in line with the statement from the literature that the power law is most suited for altitude till 50m, after which the turbulent boundary follows a logarithmic law profile with altitude. This trend helps us conclude that the suitable altitude model that can be utilized for the study is the log law. To validate the accuracy of the log law, the velocity value at an altitude of 200m is compared with the meteorological data gathered from the UAE government website, which can be observed in table 4.2, [64,59,60].

Table 4.2. Comparison between the meteorological data and the calculated data

Data Type	**Mean Wind Velocity (m/s)**		**200 m**
Meteorological Data	6.6		
Logarithmic Model	6.8		
Error	0.02941	2.941 %	

The above results concludes that the log law model is more accurate for describing the velocity-altitude relationship of the ABL hence will be adopted in this research.

4.3. Geographical Information System:

Geographical information system (GIS) employs the principle of geospatial topology, where the statistical data of the population and the environmental conditions are visualized with the surface of the earth or with each other. These comparisons are carried out to study and analyze the patterns and relationships between the data being compared [65,66]. In this section of the study, the 10m wind map is presented for better visualization of the location for BAT setup from figure 4.2:

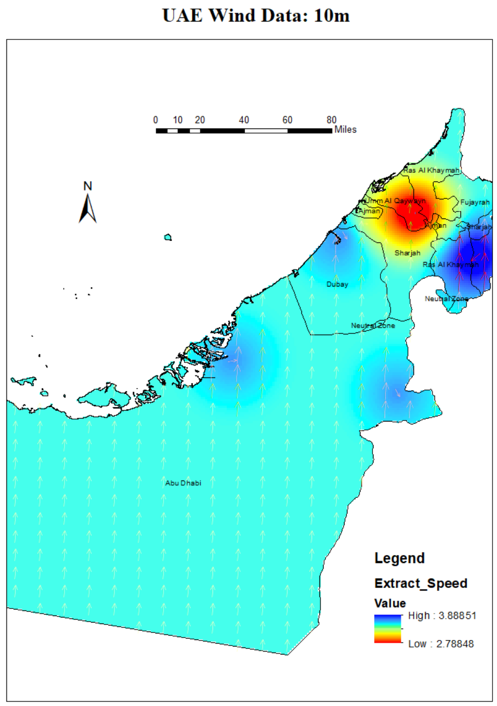

Figure 4.2. Represents the wind map of UAE at 10m Altitude

From figure 4.2, above we can observe that the wind velocities are higher in the mountain range regions like Fujairah and the regions around it and relatively better wind velocities can also be observed in and around the desert regions of UAE. The monthly average mean wind speed for each locality/region of UAE referenced from the meteorological data can be observed in figure 4.3 (A, B, and C) below, [59], from which we can observe that Fujairah presents a more stable and consistently high wind speed region in comparison to the other localities:

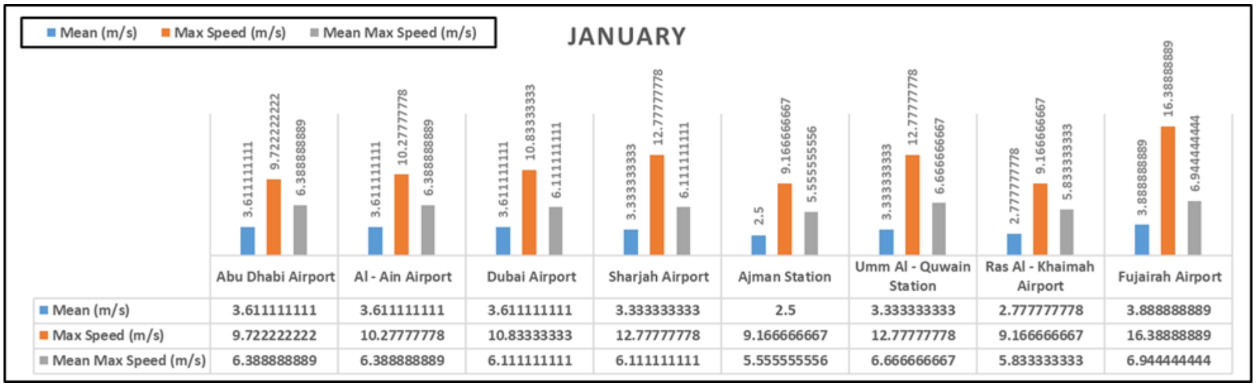

	Abu Dhabi Airport	Al - Ain Airport	Dubai Airport	Sharjah Airport	Ajman Station	Umm Al - Quwain Station	Ras Al - Khaimah Airport	Fujairah Airport
■ Mean (m/s)	3.611111111	3.611111111	3.611111111	3.333333333	2.5	3.333333333	2.777777778	3.888888889
■ Max Speed (m/s)	9.722222222	10.27777778	10.83333333	12.77777778	9.166666667	12.77777778	9.166666667	16.38888889
■ Mean Max Speed (m/s)	6.388888889	6.388888889	6.111111111	6.111111111	5.555555556	6.666666667	5.833333333	6.944444444

(A) January meteorological wind speed data

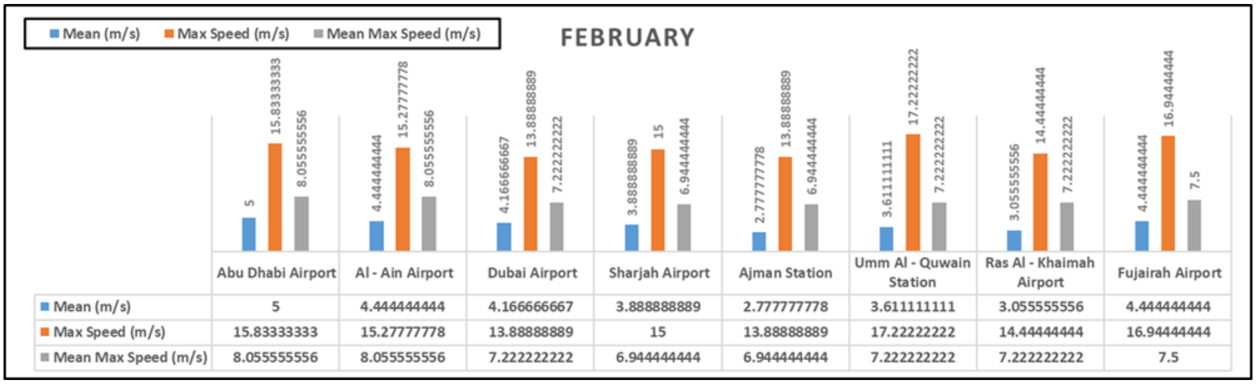

	Abu Dhabi Airport	Al - Ain Airport	Dubai Airport	Sharjah Airport	Ajman Station	Umm Al - Quwain Station	Ras Al - Khaimah Airport	Fujairah Airport
■ Mean (m/s)	5	4.444444444	4.166666667	3.888888889	2.777777778	3.611111111	3.055555556	4.444444444
■ Max Speed (m/s)	15.83333333	15.27777778	13.88888889	15	13.88888889	17.22222222	14.44444444	16.94444444
■ Mean Max Speed (m/s)	8.055555556	8.055555556	7.222222222	6.944444444	6.944444444	7.222222222	7.222222222	7.5

(B) February meteorological wind speed data

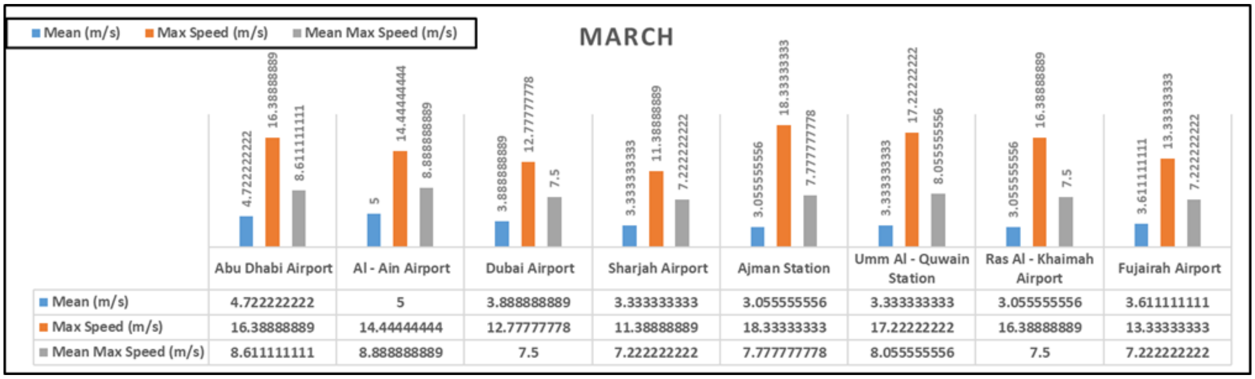

	Abu Dhabi Airport	Al - Ain Airport	Dubai Airport	Sharjah Airport	Ajman Station	Umm Al - Quwain Station	Ras Al - Khaimah Airport	Fujairah Airport
■ Mean (m/s)	4.722222222	5	3.888888889	3.333333333	3.055555556	3.333333333	3.055555556	3.611111111
■ Max Speed (m/s)	16.38888889	14.44444444	12.77777778	11.38888889	18.33333333	17.22222222	16.38888889	13.33333333
■ Mean Max Speed (m/s)	8.611111111	8.888888889	7.5	7.222222222	7.777777778	8.055555556	7.5	7.222222222

(C) March meteorological wind speed data

Figure 4.3. Monthly wind speed meteorological data of UAE region

Chapter 5

Annular Shroud System Performance and Buoyancy Calculations

In this chapter, the computational results of the annular shroud profile selection process, the performance comparison between the annular shroud system and the bare turbine system, and finally the buoyancy calculation with a prototype shroud system design are presented.

5.1. Shroud Optimization:

The shroud optimization analysis is carried out using the KT, conformal transformation and the bisected symmetric airfoil geometries. The symmetric airfoil is designed with a thickness ranging from 12%-26% [14] of the chord length for every even positive integer and the KT profile is generated with the chord length varying from 3m to 15m for every positive odd integer. The main focus of this section is to determine the optimal chord length from the KT model and then compare the different thicknesses of the symmetric NACA 4 series airfoil with the results from the KT model study to determine the optimal profile. The NACA 4 series are selected based on past studies by Stanford who made a distinct differentiable table to define the applications for each NACA series. They concluded that the NACA 4 series airfoil can be considered for shroud design applications for its good stall characteristics [47]. The study explored angles of attack of -2^o, 0^o, 2^o, and 5^o. The shroud optimization focused on the pressure coefficient, the mass flow rate, area ratio, and the wind power variation to decide on the optimal shroud.

5.1.1. Karman-Trefftz profile:

As discussed in chapter 3, the Karman-Trefftz is a conformal transformation method that converts an equation of a circle in a complex plane to an airfoil in a polar/cartesian coordinate system. The KT profile study is executed by designing an annular shroud with an airfoil profile determined through a MATLAB program utilizing equation 3.2 with a chord length varied through the radius of a circle in the complex plane. For carrying out the study, the chord length varied from 3m to 15m for every odd integer and the geometrical configurations derived from the same can be observed in figure 3.4.

The area ratio is adopted to compare the performance of different airfoils. It is calculated as the ratio of the area at the stagnation section to that of the throat at a given cord length and angle of attack as shown in figure 5.1 below:

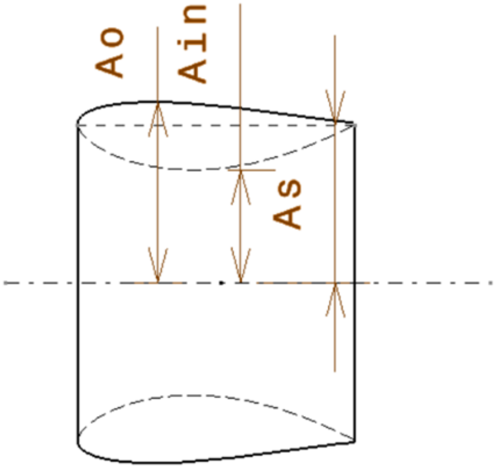

$$Area\ Ratio = \frac{A_{stagnation}}{A_{Throat}} = \frac{Stagnation\ Area}{Throat\ Area}$$

Figure 5.1. Annular Shroud Area Ratio Nomenclature

The area ratio for the KT profile with different cord lengths and angles of attack is presented in table 5.1 below:

Table 5.1. Area Ratio vs Chord Length

Chord Length (m)	**Area Ratio**			
	0º	**5º**	**2º**	**-2º**
3	1.3797	1.2890	1.3212	1.3890
5	1.4772	1.4840	1.4571	1.4829
7	1.6109	1.6687	1.6253	1.5912
9	1.6900	1.7466	1.6897	1.6648
11	1.7709	1.8652	1.7680	1.7372
13	2.0914	2.1351	2.0047	1.9917
15	1.9172	2.0118	1.9521	1.8478

From table 5.1, it can be observed that the area ratio is highest for the 13m chord length with the 5^{o} angle of attack with that at 0^{o} coming next. Next, we looked at the effect of the area ratio on the induced mass flow rate through the throat and the resulting velocity profile as well as the pressure change along the shroud. The area ratio resulted in an increase in the velocity which brings about change in pressure within the throat section. The velocity profile plot of the throat region for -2^{o}, 0^{o}, 2^{o} and 5^{o} AOA and different airfoil configurations is plotted in figures 5.2-a to d below:

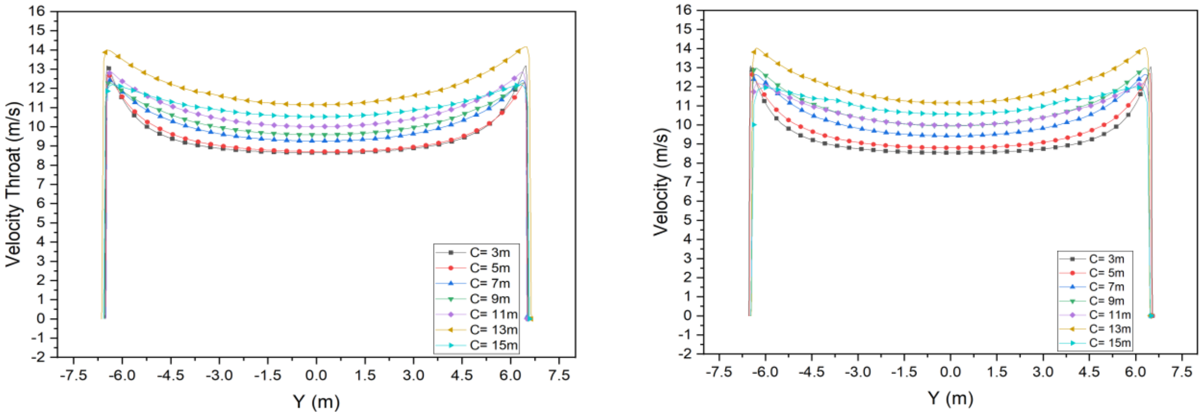

(a) Velocity KT 0^{o} AOA

(b) Velocity KT -2^{o} AOA

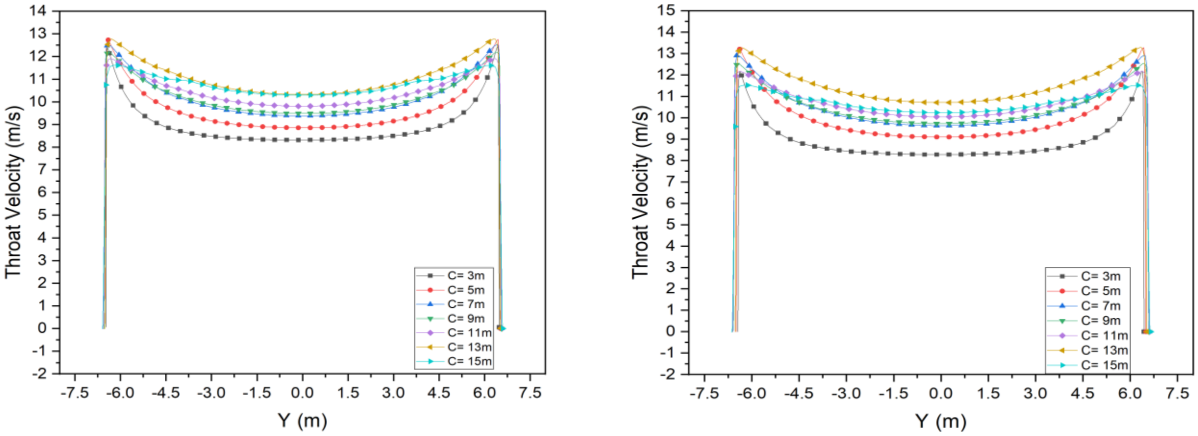

(c) Velocity KT 2^{o} AOA

(d) Velocity KT 5^{o} AOA

Figure.5.2. Velocity Cumulative: Karman-Trefftz for different chord length and, AOA -2^{o}, 0^{o}, 2^{o} and 5^{o}

From figure 5.2, it can be seen that the average throat velocity increases with increasing the chord length with the highest velocity peak at a chord length of 13m then starts decreasing for all angles of attack.

The pressure coefficient is an additional important parameter that aids in understanding the performance of the selected airfoil, it is given by:

$$Cp = \frac{P - P_\infty}{\frac{1}{2}\rho {V_\infty}^2} = \frac{Pressure\ Difference}{Dynamic\ Pressure} = 1 - \left(\frac{V}{V_\infty}\right)^2 \tag{5.1}$$

The pressure coefficient can be used to assess the flow velocity at the throat since the throat area is kept constant to account for the clearance between the turbine tip and the annular shroud, see figure 5.3 below.

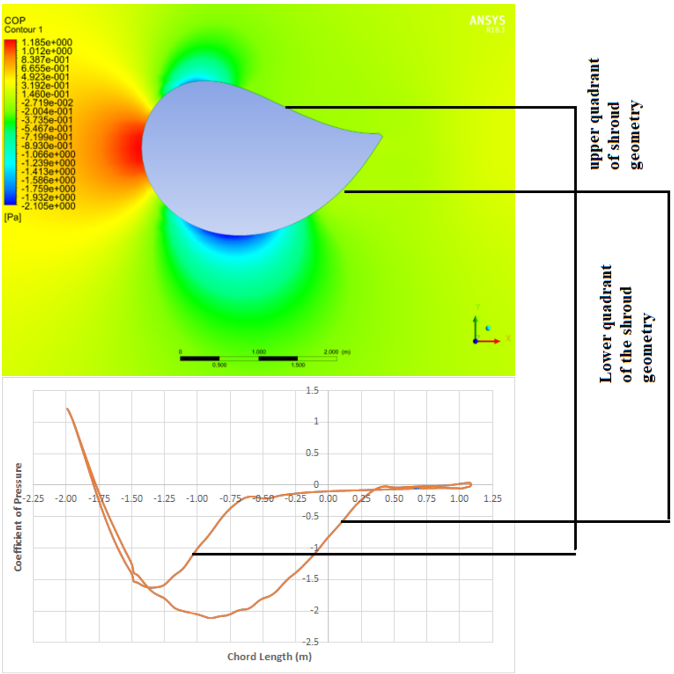

Figure 5.3. Pressure Coefficient Interpretation

As a result of the high curvature observed in the geometry from 3m, 4m, and 5m chord length which can be seen from figure 3.4, it can be observed from figure 5.4 that the curvature resulted in high stall as a result of the early separation and delay in the pressure recovery. The early separation destabilizes the flow around the shroud creating turbulent eddies bringing about an unpredictable pressure variation between the outer region and the throat of the 3m, 4m and the 5m variants of the KT profiles. This makes it impractical to use the first three KT profiles in forming the turbine shroud. Examining profiles with chord lengths between 9 and 15 meters showed a much lower pressure coefficient near the throat of the 13m chord length airfoil, which is a result of the increase in velocity near the low area throat section where the turbine will be placed.

A compilation of the pressure coefficient of the Karman-Trefftz configurations is presented below in figure 5.5.

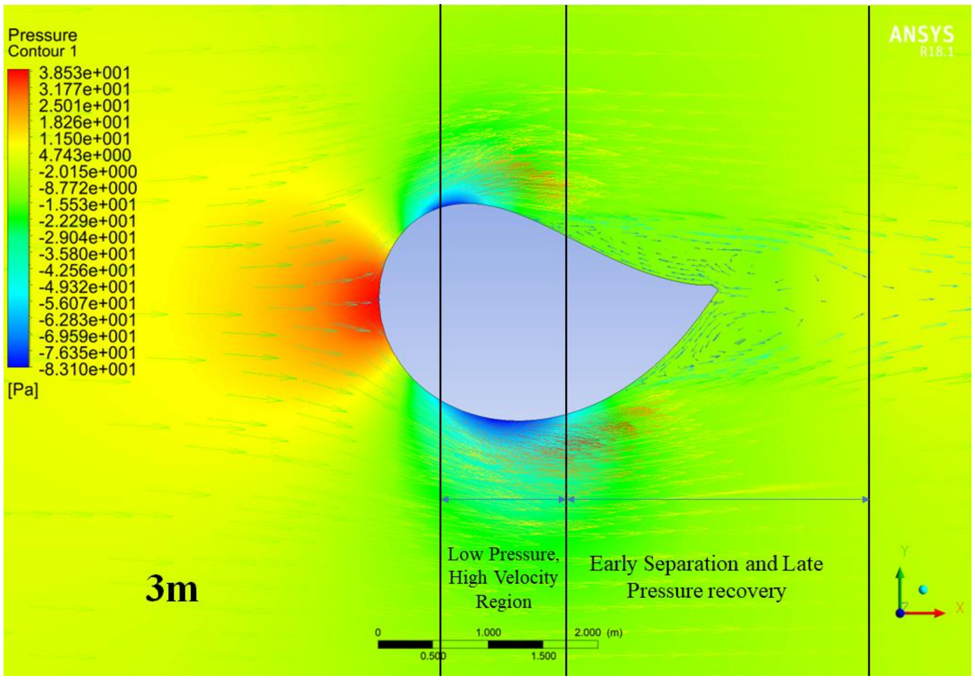

Figure 5.4. Velocity vector and pressure contour plot, C= 3 m

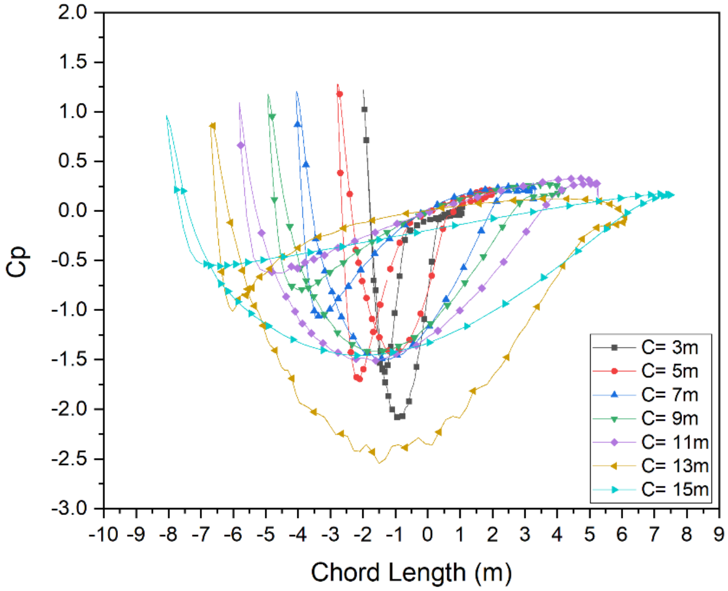

Figure 5.5. Pressure Coefficient C = 3m to 15m

The mass flow rate amplification factor, defined as the ratio of the shrouded system mass flow rate to the open system flow rate, signifies the improvement caused by the shroud system.

According to a study conducted at Stanford, the amplification factor is a viable tool for shroud selection. The integral form of the Mass Flow rate can be represented from the equation below:

$$\dot{m} = 2\pi\rho \int_0^R u(r)rdr \tag{5.2}$$

where, ρ = density of air, R = Throat Radius, u(r) = axial velocity component, $\dot{m}$= Mass flow rate

The mass flow amplification factor seen below:

$$Mr = \frac{\dot{m}}{(\rho U_\infty \pi {R_s}^2)} \tag{5.3}$$

where, Rs = Standard Shroud Throat Radius, U_∞ = Up stream wind velocity

The mass flow rate integration is carried out using the “trapz ()” function of MATLAB and the results are as presented in Table 5.2 and Figures 5.6 (a and b) below:

Table 5.2. Mass Flow Rate Karman Trefftz for AOA 0^o, -2^o, 2^o and 5^o

Chord Length (m)	**Mass Flow Rate (Kg/s) x10^3**				**Mass flow Amplification Factor**			
	0^o	**5^o**	**2^o**	**-2^o**	**0^o**	**5^o**	**2^o**	**-2^o**
3	1.6243	1.4761	1.5117	1.5967	1.2487	1.1348	1.1622	1.2275
5	1.6080	1.7027	1.6475	1.6430	1.2362	1.3089	1.2665	1.2631
7	1.7076	1.8423	1.7486	1.7215	1.3128	1.4024	1.3443	1.3235
9	1.7745	1.8193	1.7463	1.8049	1.3642	1.3986	1.3425	1.3875
11	1.8222	1.8455	1.7776	1.7681	1.4008	1.4188	1.3666	1.3593
13	2.1039	1.9439	1.8606	1.9922	1.6174	1.4944	1.4304	1.5315
15	1.8752	1.8188	1.8114	1.8073	1.4416	1.3982	1.3925	1.3894

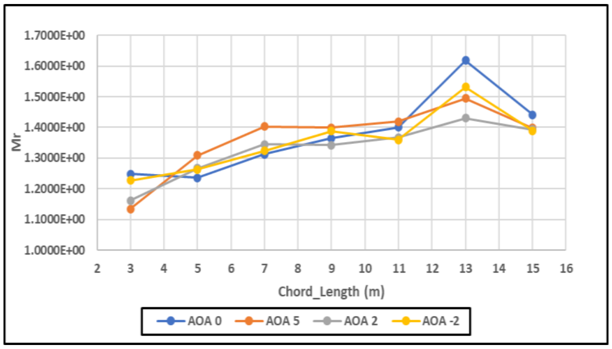

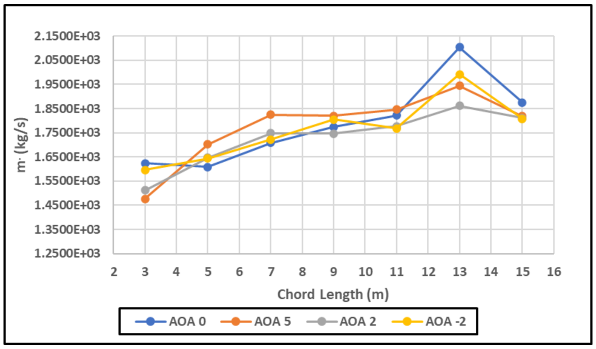

(a) Mr vs Chord Length (b) Mass Flow Rate vs Chord length

Figure.5.6. Mass flow Rate and Mass Flow Amplification Factor vs different Chord Length for AOA 0°, 2°, -2°, and 5°, C = 3m to 15m

From the above figure and the table, we can deduce that the 13m chord length delivers a higher mass flow rate in comparison with the other airfoils. However, although the 5° AOA variant of the 13m chord length resulted in the highest area ratio, table 5.1 above, the maximum flow rate occurred at the 0° AOA as shown table 5.2 and figure 5.6 above. This can be attributed to the longer path from the stagnation point to the throat position in the 5° AOA case which gave rise to a thicker boundary layer formation and lower flow rate, see table 5.3 below:

Table 5.3. Stagnation point position

Chord length (m)	**Stagnation Point Position (Y m)**			
	0°	**5°**	**2°**	**-2°**
3	7.6350	7.4500	7.5000	7.6300
5	7.9000	8.000	7.8800	7.8800
7	8.2500	8.5000	8.3300	8.1500
9	8.4500	8.7000	8.5000	8.3300
11	8.6500	9.0000	8.7000	8.5000
13	9.4000	9.6000	9.2500	9.1000
15	9.0000	9.3600	9.1500	8.7500

Figure 5.7 (a) and (b) shows the pressure distribution along the profile where the 0° angle of attack case demonstrated a smoother and relatively lower pressure variation along the inner surface of the shroud.

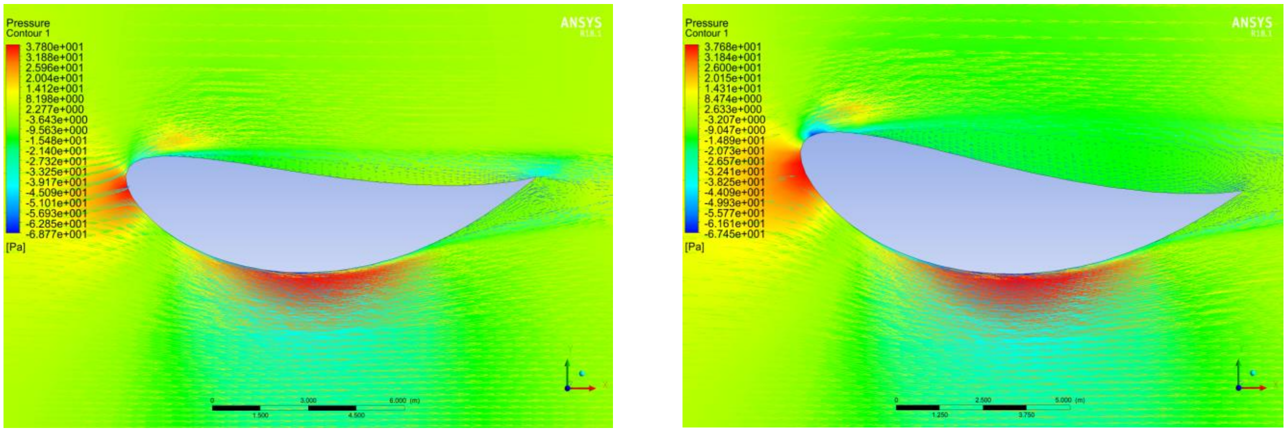

(a) 0^o AOA

(b) 5^o AOA

Figure 5.7. 0^o, and 5^o AOA vector-pressure contour for chord length 13m

In the mass flow rate amplification comparison, we can observe that the 0^o and -2^o, presented a much higher mass flow in comparison to the other 13m variants.

The case of the shroud system optimization cannot be concluded without looking at the generated turbine power. The comparison datum was taken as the power of the wind available at an area equal to the throat of the shroud and a free stream wind velocity which is given by:

$$P = \frac{1}{2}\rho A_{throat} V_{\infty}{}^{3} \tag{5.4}$$

where, P = Wind Power (W), ρ= air density (kg/m^3), A_{throat} = Throat area within the annular shroud and V_{∞} = free stream velocity

The integral form of the wind power in the throat region within the annular shroud can be represented as follows:

$$P = \frac{2\pi\rho}{2}\int_{0}^{R_{peak}} \big(u(r)\big)^{3} r dr \tag{5.5}$$

where R_{peak} = The radius from the peak velocity of the boundary layer to the center of the annular shroud.

The computed results for the wind power and power ratio are given in table 5.4 and figure 5.8 below from which we can see that the 13m, 0^o AOA profile shroud resulted in an increase in the available wind power.

Table 5.4. Wind Power and Power Ratio vs Chord Length

Chord Length (m)	Wind Power (W) $x10^4$				Power Ratio			
	0^o	5^o	2^o	-2^o	0^o	5^o	2^o	-2^o
3	8.3855	6.5856	6.9273	7.8941	2.0145	1.5821	1.6642	1.8965
5	8.1014	9.7745	8.7654	8.6264	1.9463	2.3482	2.1058	2.0724
7	9.6885	11.276	10.187	10.193	2.3276	2.7089	2.4474	2.4487
9	10.487	11.066	10.060	11.663	2.5193	2.6585	2.4168	2.8020
11	11.681	11.397	10.493	10.895	2.8063	2.7380	2.5208	2.6174
13	15.416	13.973	15.241	15.699	3.7070	3.3569	2.9724	3.6615
15	12.133	10.857	10.982	11.668	2.9149	2.6083	2.6383	2.8032

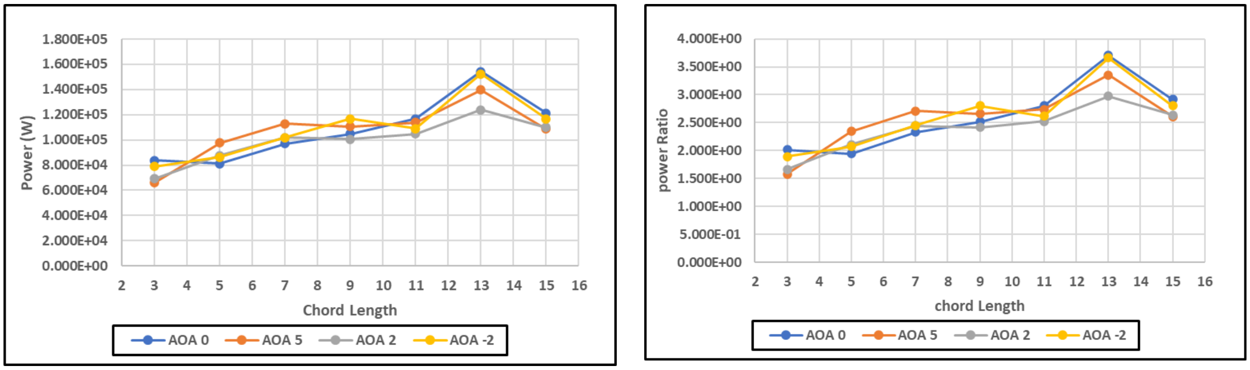

(a) Power vs Chord Length

(b) Power Ratio vs Chord Length

Figure.5.8. Wind Power vs different Chord Length vs different AOA Representation, C = 3m to 15m, AOA 0^o, 2^o, 5^o, -2^o

Table 5.5 and figure 5.9 below summarizes all the comparisons discussed above:

Table 5.5. Karman Trefftz data, cumulation for all angle of attack

Chord Length (m)	0º			5º		
	Power Ratio	Mass Flow Ratio	Area Ratio	Power Ratio	Mass Flow Ratio	Area Ratio
3	2.0145	1.2487	1.3797	1.5821	1.1348	1.2889
5	1.9463	1.2361	1.4771	2.3482	1.3088	1.4840
7	2.3276	1.3127	1.6109	2.7089	1.4024	1.6687
9	2.5193	1.3642	1.6900	2.6585	1.3986	1.7465
11	2.8063	1.4008	1.7709	2.7380	1.4187	1.8651
13	3.7070	1.6174	2.0913	3.3569	1.4944	2.1350
15	2.9149	1.4416	1.9171	2.6083	1.3982	2.0118

Chord Length (m)	2º			-2º		
	Power Ratio	Mass Flow Ratio	Area Ratio	Power Ratio	Mass Flow Ratio	Area Ratio
3	1.6642	1.1622	1.3211	1.8965	1.2275	1.3890
5	2.1058	1.2665	1.4571	2.0724	1.2630	1.4828
7	2.4474	1.3442	1.6252	2.4487	1.3234	1.5911
9	2.4168	1.3424	1.6897	2.8020	1.3875	1.6648
11	2.5208	1.3665	1.7680	2.6174	1.3592	1.7372
13	2.9724	1.4304	2.0047	3.6615	1.5315	1.9917
15	2.6383	1.3925	1.9520	2.8032	1.3894	1.8477

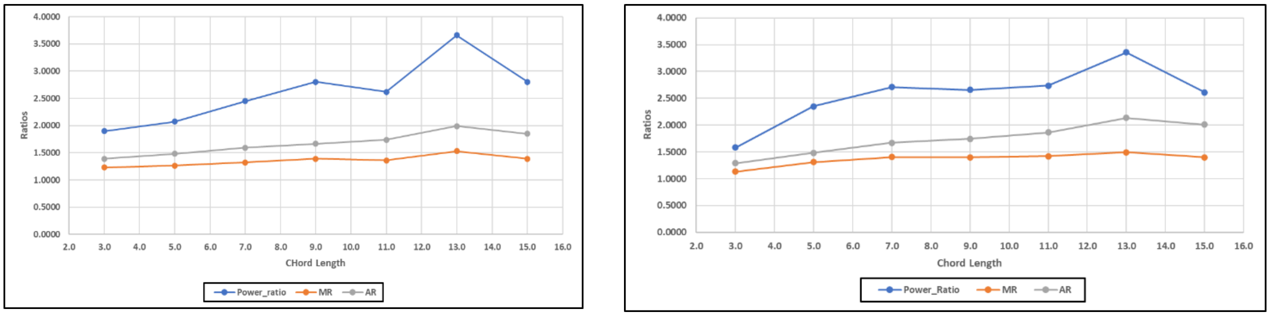

(a) AOA 2^{o}

(b) AOA 5^{o}

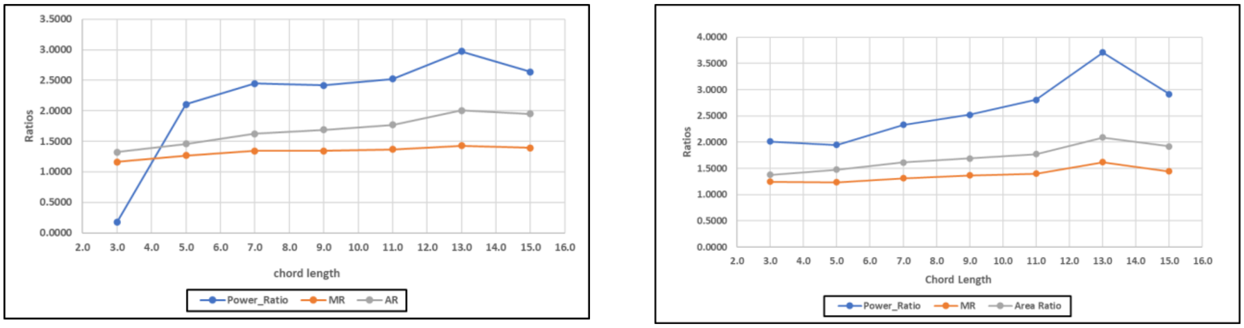

(c) AOA -2^{o}

(d) AOA 0^{o}

Figure.5.9. Karman Trefftz Data Cumulation for AOA 0^{o}, -2^{o}, 2^{o} and 5^{o} and different chord length, C= 3m to 15m

From the above table and plots, it can be concluded that although the profile cord length and angle of attack are the major players in determining the area configuration inlet to throat area ratio, hence the mass flow rate and available wind power, the distance from the stagnation point to the throat plays a secondary role in disturbing the expected relationship through affecting the boundary layer thickness development and the integrated mass flow rate through the throat area.

5.1.2. Symmetric Airfoil:

This section compares the performance of the NACA 4 series airfoil with that of the KT 13m profile. The study covered a thickness ranging from 12% to 26% for every even positive integer, see figure 3.5 of chapter 3 above [14]. According to Stanford's NACA airfoil data summary, it was stated that the NACA 4 series airfoil is best possible for shroud applications as a result of their good stall characteristics [48], and most of the past studies concluded that the NACA 4 series and 5 series airfoils have better aerodynamic characteristics in comparison to the other airfoils. The angle of attack was not considered since the airfoil is symmetric.

The calculated area ratio for the 0°, -2° and 2° AOA variants of symmetric airfoil is shown in table 5.6 below, from which we can see that the area ratio keeps increasing with the increase of the profile thickness.

Table 5.6. Thickness (%) vs Area Ratio

Thickness	Area Ratio 0°	Area Ratio -2°	Area Ratio 2°
12	1.296	1.266	1.286
14	1.349	1.321	1.337
16	1.359	1.355	1.388
18	1.414	1.410	1.432
20	1.440	1.427	1.441
22	1.477	1.465	1.496
24	1.552	1.522	1.552
26	1.579	1.561	1.589

From the table above we can observe a proportional increase in the area ratio despite the variation in AOA. From further observation on the AOA variation, we can also infer that with increase in the negative angle of attack the area ratio decreases and the same can be said for the increase in the positive AOA will result in the increase in the area ratio. As a result, further variants of different angles of attack are not taken into consideration and the study for symmetric airfoil is restricted to the 0°, 2° and -2°.

The Pressure coefficient compilation figure for the airfoils at 0 deg angle of attack is presented below in figure 5.10 for observation. From the plot in figure 5.10, we can observe that there is a steady reduction in the pressure coefficient at the lower quadrant of the airfoil with the increase in the thickness of the airfoil. This can only be validated if the throat area is constant for the increase in thickness. To validate the result of the pressure coefficient, the experimental Cp data of NACA 0012 at 0° AOA which was carried out by Marquette University was taken as reference [68]. The comparative result of Cp for NACA 0012 between the experimental and the computational result can be observed in figure 5.11 below. From figure 5.11, we can observe that there is a slight variation in the Cp between the computational and the experimental result, this could be as a result of the atmospheric conditions the experiment was carried out in which and the condition of the wind tunnel surface which could factor in to the negligible variation in the flow of the fluid about the airfoil.

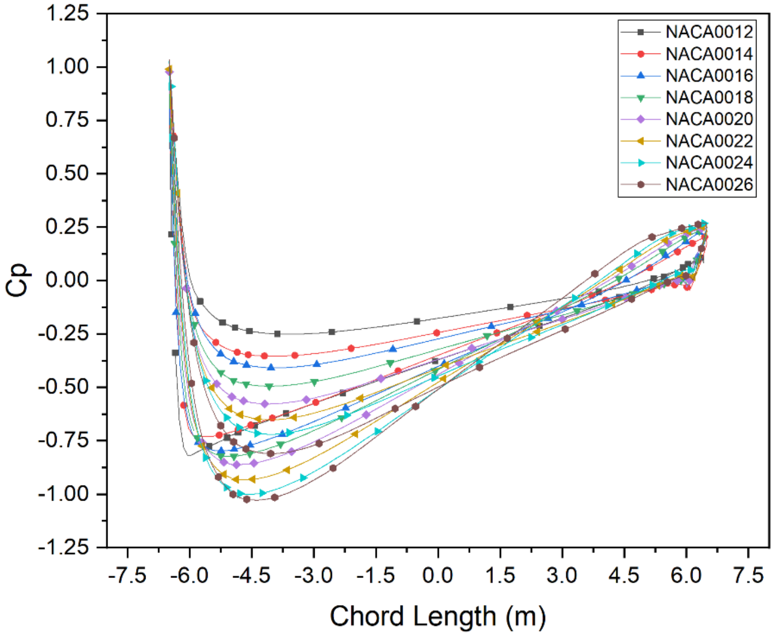

Figure 5.10. Pressure Coefficient: NACA 4 series Symmetric Airfoil for different thicknesses, t= 12% to 26%

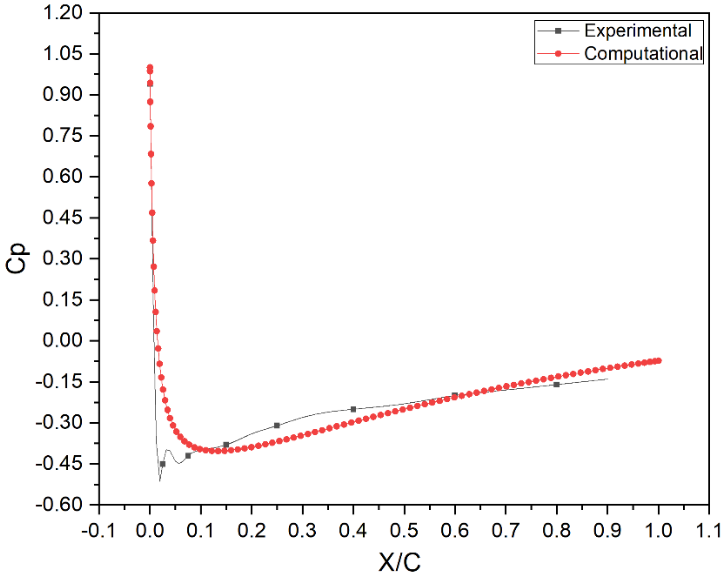

Figure 5.11. Experimental vs Computational Comparison: NACA 0012

The parameters studied in the KT study are presented. The velocity profile of the throat region, is taken into consideration for the study. The velocity profile for -2° ,2° and 0° AOA is presented in figure 5.12 below:

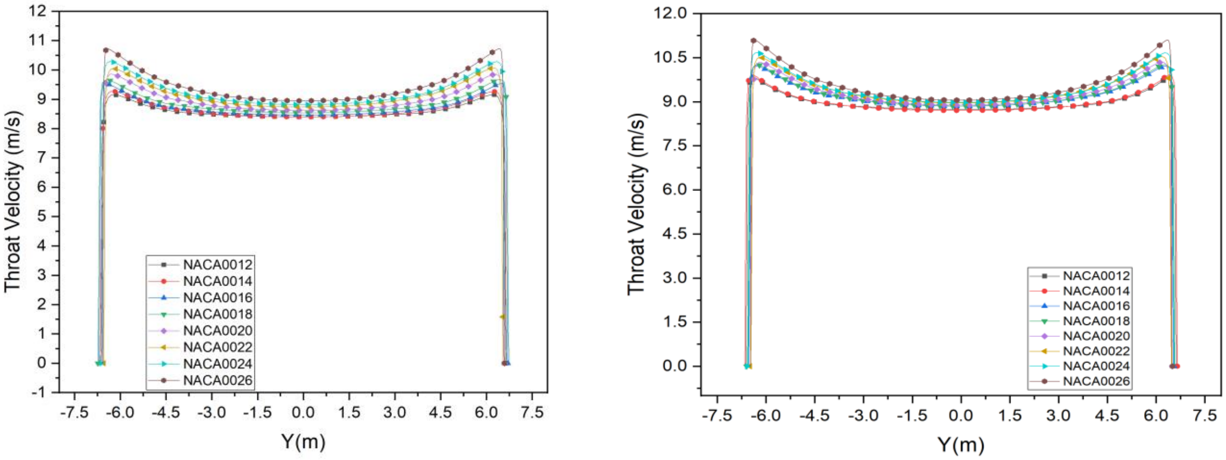

(a) AOA 0°

(b) AOA -2°

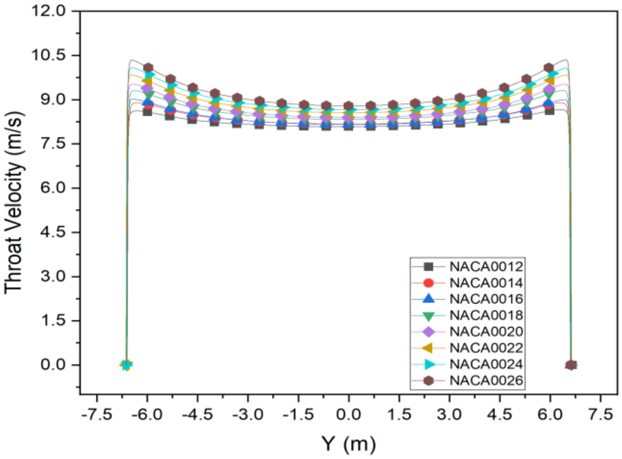

(c) AOA 2°

Figure.5.12. Throat Velocity Profile: Symmetric NACA 4 Series, AOA -2°, 0° and 2°

From figure 5.12 above we can infer that a similar increasing trend in the data for the -2°, 2° and 0° AOA with the -2° AOA variant presenting a higher flow velocity through the throat section in comparison to the 0°. Using the integral equation of mass flow rate (5.2) as mentioned in Karman-Trefftz, the mass flow rate is computed in MATLAB with the trapezoidal method (trapz() function), and the results are plotted in figure 5.13 utilizing the data from table 5.7 as follows:

Table 5.7. Mass flow and Mass flow Amplification Rate Factor vs Thickness

Thickness	Mass Flow Rate 0° x10^3	Mass Flow Rate -2°x10^3	Mass Flow Rate 2° x10^3	Mass Flow Amplification 0°	Mass Flow Amplification -2°	Mass Flow Amplification 2°
12	1.4637	1.5235	1.4091	1.1252	1.1713	1.0833
14	1.4821	1.5463	1.4200	1.1394	1.1888	1.0917
16	1.4813	1.5318	1.4298	1.1388	1.1776	1.0992
18	1.4981	1.5413	1.4650	1.1517	1.1849	1.1262
20	1.5228	1.5426	1.4977	1.1707	1.1859	1.1514
22	1.5451	1.5618	1.5422	1.1878	1.2007	1.1856
24	1.5813	1.5924	1.5657	1.2157	1.2242	1.2037
26	1.5929	1.6019	1.5903	1.2246	1.2315	1.2226

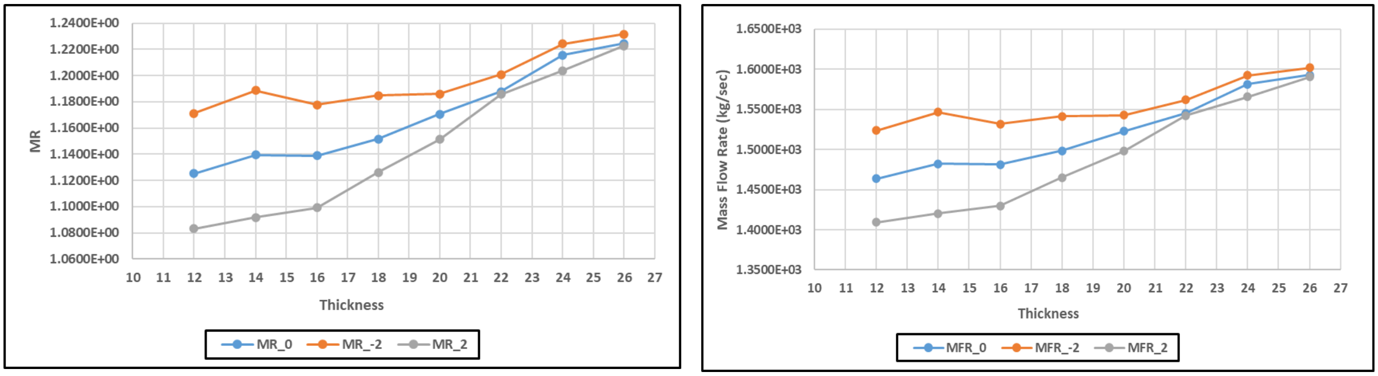

(a) Mass Flow Rate vs thickness

(b) Mr vs thickness

Fig 5.13. Mass Flow and Mass Flow Amplification vs different thicknesses, for AOA 0°, 2° and -2°, t = 12% to 26%

From the plots above an increasing trend of the data is observed in the mass flow rate and it can be concluded that the increase in trend persists beyond the defined thickness range. Both the figures 5.12 and 5.13 presents results in favor of the -2° AOA variant though the area ratio from table 5.6 presents results more favorable to the 0° AOA. This is can be explained through an observation from the location of the stagnation point of -2° which is more interior/lower in comparison to the 0^{o} AOA which can be observed from table 5.8 and the boundary layer separation comparison between the 0^{o} and the -2^{o} from figure 5.14 presented through vectors-pressure contour presents that the 0^{o} AOA variant traces a larger flow distance along the curvature before separation in comparison to the -2^{o} AOA giving rise to a better flow velocity and flow rate.

The stagnation point location and vector-pressure contour can be observed from table 5.8 and figure 5.14 below:

Table.5.8. Stagnation point: NACA 4 Series Symmetric Airfoil

Stagnation point Position (Rs) m			
Thickness (%)	**AOA 0^{o}**	**AOA -2^{o}**	**AOA 2^{o}**
12	7.4	7.2	7.4500
14	7.55	7.4	7.6000
16	7.58	7.45	7.7500
18	7.73	7.6	7.8750
20	7.8	7.65	7.9000
22	7.9	7.75	8.0500
24	8.1	7.9	8.2000
26	8.17	8.0	8.3

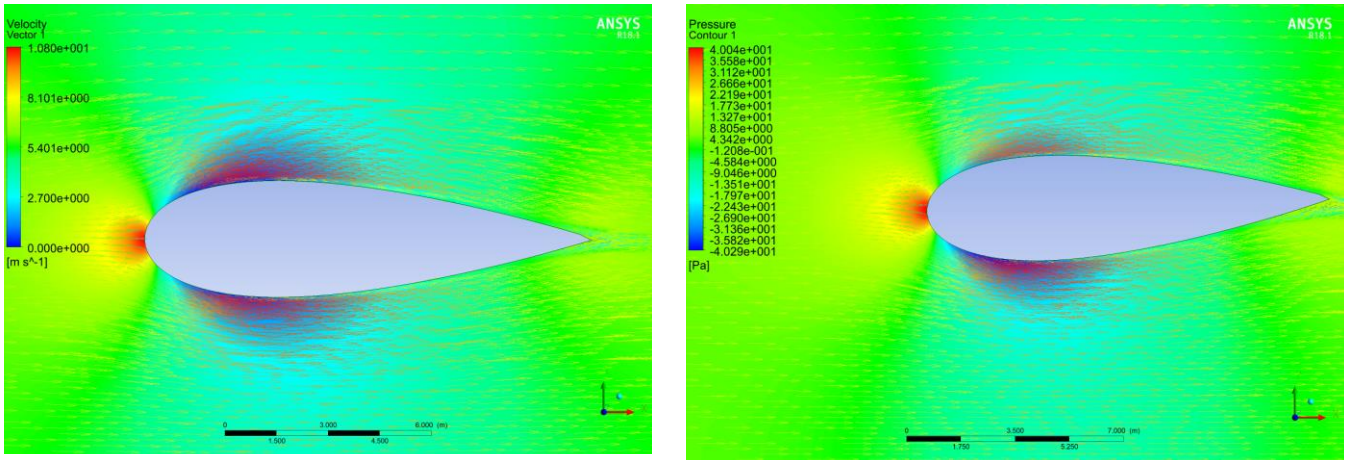

(a) 0^{o} **(b) -2^{o}**

Figure 5.14. Vector-Pressure contour of 0^{o} and -2^{o} AOA symmetric airfoil 26% thickness

The final parameter studied which also presents a similar trend is the wind power utilizing equation **(5.5)** as presented in the Karman-Trefftz methodology can be observed from figure 5.15 below:

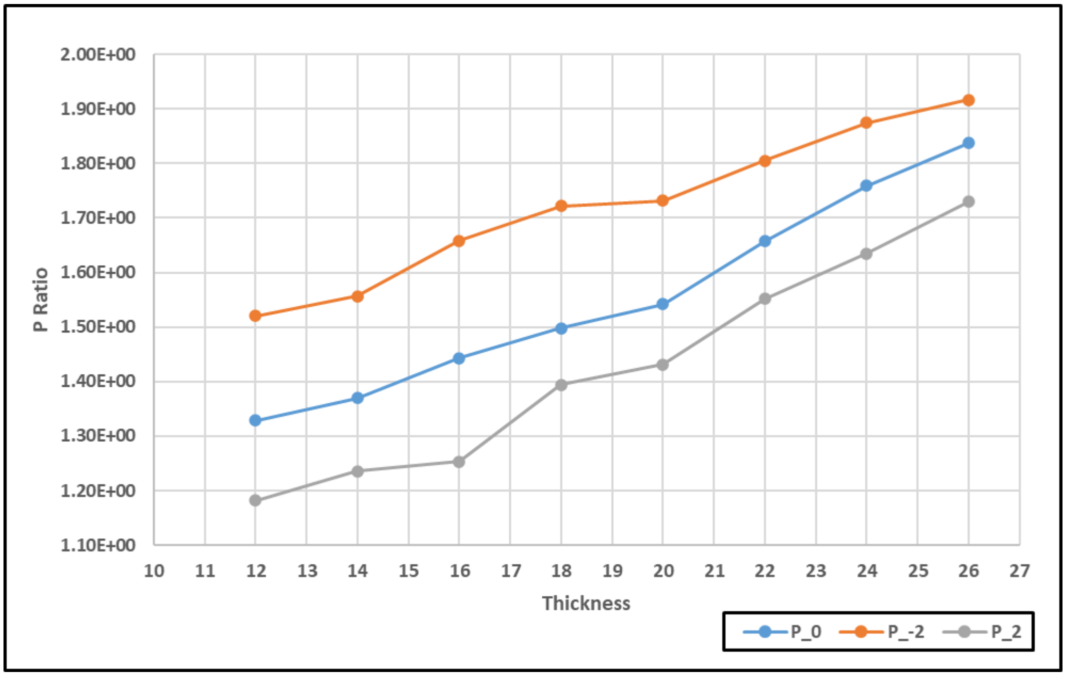

Figure 5.15. Power ratio to the different thickness configurations for AOA 0^o, -2^o and 2^o, t= 12% to 26%

Since the parameters related to the study of the thickness distribution present an increasing trend in performance with an increase in thickness the final parameter taken to finalize a shroud geometry in the case of the symmetrical airfoil is the annular shroud volume capable of the buoyant lift. This is done by comparing the volume of the 13m chord length shroud configuration of KT to the Symmetric airfoil thickness and selecting a volume close to the KT 13m conformally transformed airfoil.

We can conclude that 13m chord length KT airfoil presents a higher performance efficiency in comparison to the other airfoils in the Karman-Trefftz list and the bisected symmetric airfoil annular shroud that can closely relate to the 13m chord length is the profile that possesses a thickness of about 25% of the Chord length.

5.1.3. Turbine performance comparison:

The performance comparison between the bare turbine and the shrouded turbine is the final step to validate the advantage of the inclusion of annular shroud to the turbine system. Since the simulation is carried out computationally, the analysis is set at the optimum TSR of 4.12 derived from equation (3.29) with a wind velocity of 8m/s, where the RPM is determined. The calculated bare turbine is set at 50 RPM while the rotation for the shrouded turbine is calculated based on the augmented average wind velocity at the throat section of the 13m KT shroud, which is 12m/s for this case, resulting in 75 RPM for the shrouded turbine. To validate the effectiveness of the computational model, the 8m/s brochure data for the Aeolos H 30 kW turbine is compared to the computational results in table 5.9 below. The deviation is within 6.1% which can be attributed to the assumptions of the boundary conditions, The type of mesh utilized and the empirical constants that facilitate the physics used to set the CFD analysis, the discretization and convergence errors, hence we can accept the computational results with confidence. Table 5.10 compares the bare and shrouded turbines output power. Recalling the wind power comparison presented in the KT analysis section, we found that the shroud induced a 270% increase in the available wind power relative to the free stream wind. However, the results showed a turbine power augmentation of 221% from the computational results which indicates a loss of around 13.2% from the augmented wind power due to the turbine insertion in the shroud. This can be attributed to the interactions of the turbine blades tips with the shroud which generates added friction, the tip-shroud clearance of 5 cm and the non-uniform velocity distribution across the throat section.

The interaction of the augmented flow with the turbine insertion can be observed from the pressure contour comparison between the bare turbine and the modified turbine system presented in fig 5.16 (a) to (d) below. We can observe from figure 5.16 (a) that a high pressure is created close to the blade as a result of the reduction of the velocity as it approaches the swept area which is associated through the phenomenon of boundary layer creation on the surface of the turbine blade as a result of the viscous forces derived from the no-slip condition. From figure 5.16 (b), we can deduce a similar pattern of high pressure before the swept region at the upstream and the low pressure at the downstream but we can also observe a non-uniform pressure and velocity distribution about the blade geometry. The velocity contour of the turbine from the front view projection is presented below to present a better visualization of the wind flow through the bare and the 13m KT shrouded turbine. From figure 5.16 (c) and (d), we can observe the upstream velocity flow contour through the turbine and the phenomenon of velocity recovery behind each turbine blade as a result of the magnus effect about the turbine blade cross-section. We can observe a similar boundary layer formation on the edges of the blade, from the figure 5.16 (c) and (d), but a higher velocity can be observed in figure 5.16 (d) which can be attributed to the non-uniform velocity distribution about the throat section in the presence of the shroud. The average upstream velocity about the throat section flow within the shroud presents a 50% increase from the design velocity of 8m/s from

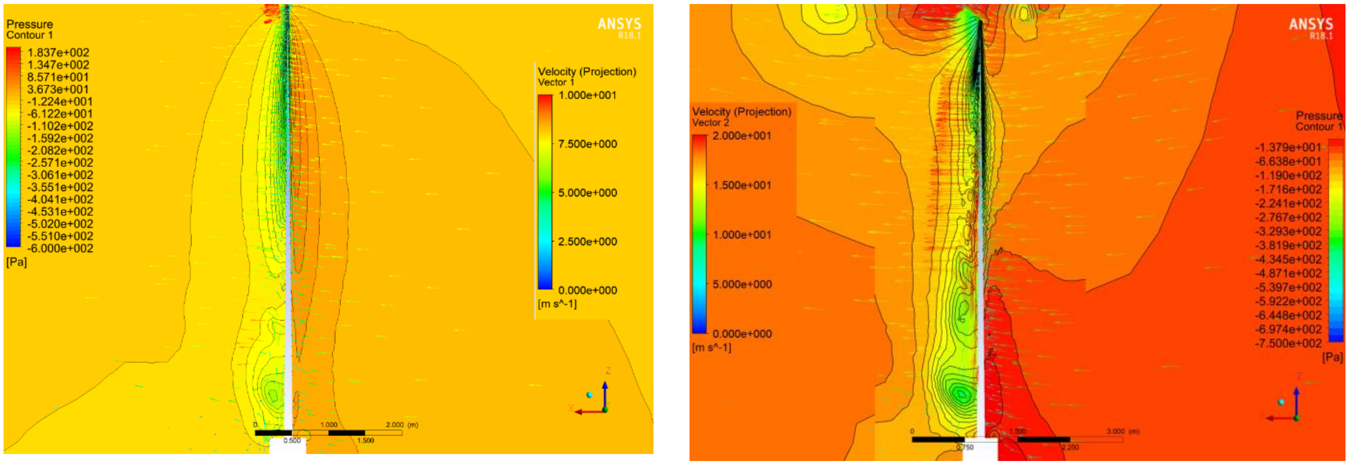

(a) Bare Turbine pressure + velocity vector contour

(b) 13m KT shrouded turbine pressure + velocity vector contour

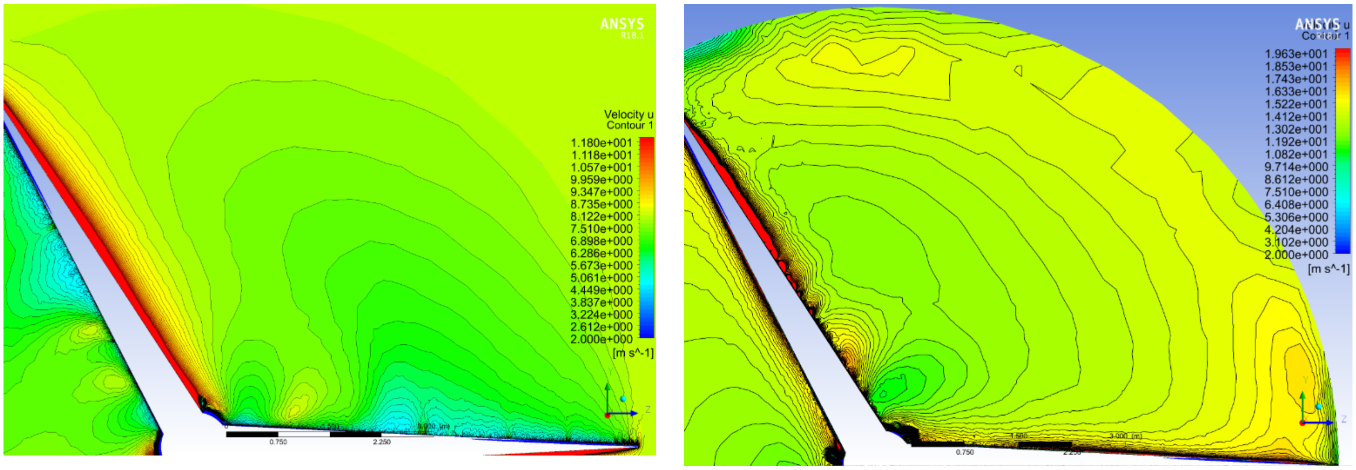

(c) Velocity contour of bare turbine

(d) Velocity contour of 13m KT shrouded turbine

Figure.5.16. Pressure contour and velocity contour of bare and 13m KT shrouded turbine

Moreover, the underestimation of the turbine power by the CFD model further reduces the predicted turbine power augmentation to 201.0% which matches the bare turbine predicted power ratio of 94%.

Table 5.9. Computational Result vs the Industrial Data (Bare turbine)

Wind Speed (m/s)	Industrial Data		Computational Data		Error (%)
	Torque (N-m)	Power (W)	Torque (N-m)	Power (W)	
8	2005.3	10500.0	1881.0	9849.2	6.1

Table 5.10. Bare Turbine vs Shrouded Turbine, Power Comparison

Wind Speed (m/s)	Bare Turbine		Shrouded Turbine	
	Torque (Nm)	Power (W)	Torque (Nm)	Power (W)
8	2005.3	10500.0	4030.3	31654.5

Table 5.11. Wind, manufacturer and Simulation power ratio Comparison

Available wind power ratio	Turbine power ratio (simulation)	Turbine power ratio (Manufacturer)
3.70	3.21	3.01

5.2. Buoyancy Calculation:

Buoyancy is a critical design factor for the system where it determines the shroud's capability to lift the required payload to the operational altitude. The floating turbine system consists of a turbine harnessed at the center of the annular shroud that is tethered to a rotational platform via 3 or 4 support tethers amongst which one is conductive in nature for transfer of electricity to the ground station. In this section, the buoyant lift force calculation is presented together with a visual representation of the concept design. The buoyant shroud system consists of a turbine, a 13m KT profile shroud which was derived from the shroud optimization study, a conceptual design of the skeletal structure, and finally the tethers that accounts for the stability of the system. A visualization of the parts of the buoyant shroud system can be seen in figure 5.17 below.

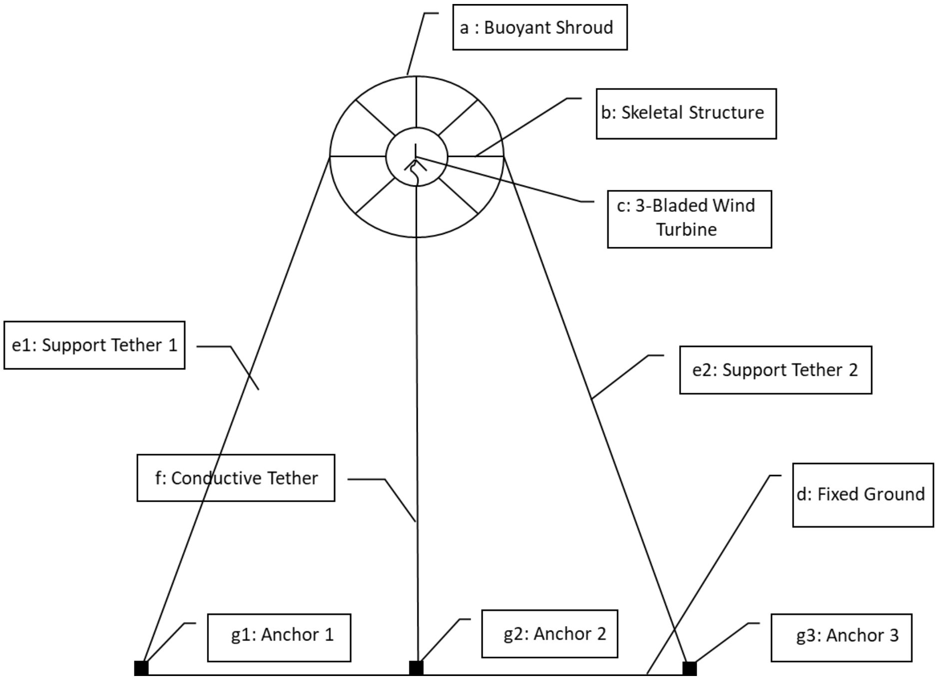

(a) **Front View**

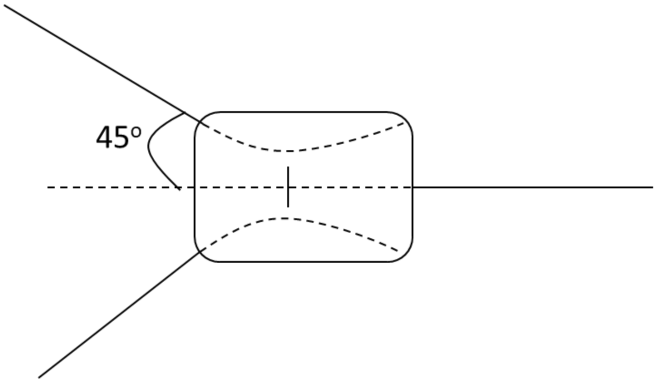

(b) **Top View**

Figure.5.17. Shroud system parts and representation

The Aeolos H 30kW turbine is taken for its relatively light weight. The buoyant shroud is the part of the system required for augmenting the wind power and lifting the turbine to the operational altitude. The material selected to fabricate the shroud is the same as that used for blimps which is plastic composite fiber sheets. In current manufacturing, the blimp envelope is mostly made of Kevlar, Mylar, and Chloroprene [69]. The weight of the shroud envelope is determined through the thickness of the material chosen for the design, and the volume of the solid envelope sheet derived though the surface area and the thickness of the envelope.

The third contributor to the system weight is the skeletal support structure of the buoyant shroud that acts as a foundation for its design. The conceptual skeletal support structure created for the current buoyant shroud setup is presented in figure 5.18

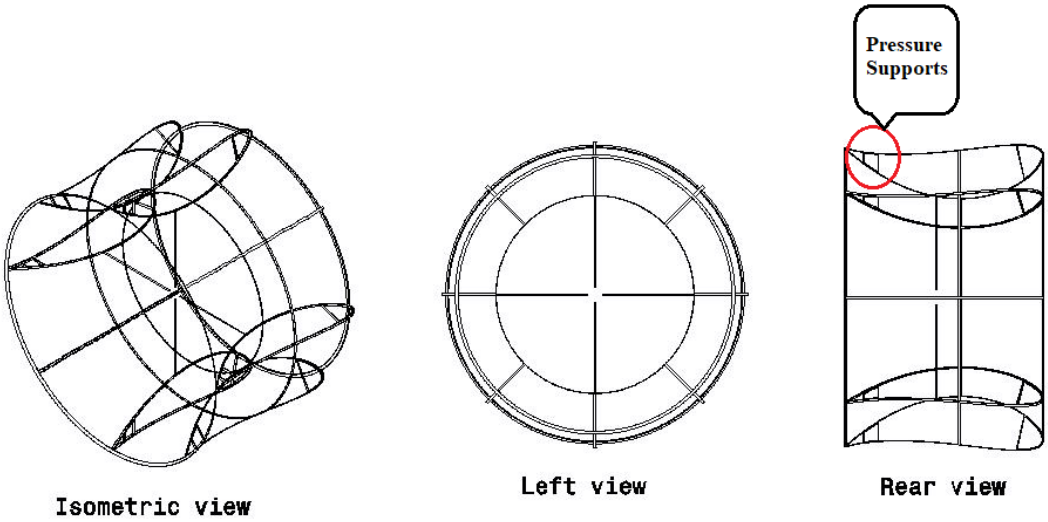

Figure.5.18. Skeletal Support Structure of Buoyant Shroud Setup

The skeletal structure is designed to provide a foundation for to the profile of 13m KT/NACA 0025 profile. The volume of the skeletal structure is determined using the CATIA V5 software. Typically, materials having high load bearing capacity is selected to accommodate for the pressure spots on the selected profile [70]. The lighter than air gases utilized for the lift of the system are either Hydrogen or Helium [38,71]. The main reason for the lower utilization of hydrogen is its high flammability when it mixes with oxygen in the air. The next alternative is helium, which is more expensive than hydrogen, however, it's widely preferred in airborne buoyancy-driven devices due to its safety features. The lifting capability of the hydrogen is about 1.1034 g/L whereas that for Helium is 1g/L.

The tethers are the stability support for the whole system as it's supposed to restrict the motion of the whole system at the operational altitude to maximize performance. For the conceptual design, 3 or 4 tethers are considered, out of which one is a conductive tether that transfers the generated electricity to the ground. A representation of a typical conductive tether i.e., an electrical cable can be observed from the figure 5.19 below

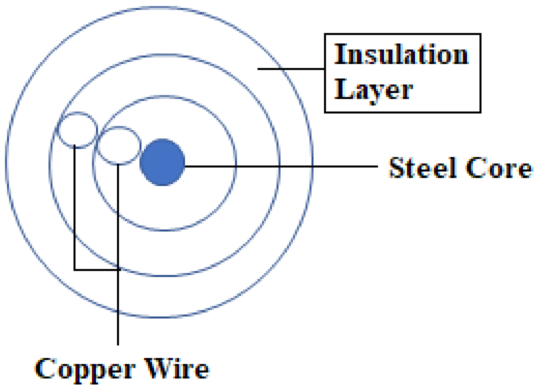

Figure.5.19. The layout of the electrical cable utilized in Industries

From the figure 5.18 above one can see that the supports are tethered and positioned structured in a trapezoidal tetrahedral structure to improve system stability. The position of support tether and its anchor are tethered at 45° from the center, to provide support against angular push down from the wind force experienced on the shroud from all the sides. The weight and the system characteristics of each part of the system can be observed from the table 5.12 below:

Table.5.12. Weight and system characteristics of the system parts:

Parts			**Weight (N)**
Turbine	Mass (Kg)	980.0	9613.8
Skeletal Structure	Volume (m^3)	3.228	85500.036
	Density Al (kg/m^3)	2700.0	
Shroud Envelope	Thickness of Material (mm)	1.5	18267.9
	Surface Area (m^2)	1501.7	
	Density of Mylar (Kg/m^3)	1400	
Tether Support (Steel)	Volume (m^3)	0.000322	24.1929
Conductive Tether	Volume (m^3)	0.010602	332.876

5.2.1 Force Calculations:

The buoyant force calculation which is essential to determine the lift capability of the system can be resolved through the free body diagram presented below in figure 5.20 (a) to (c).

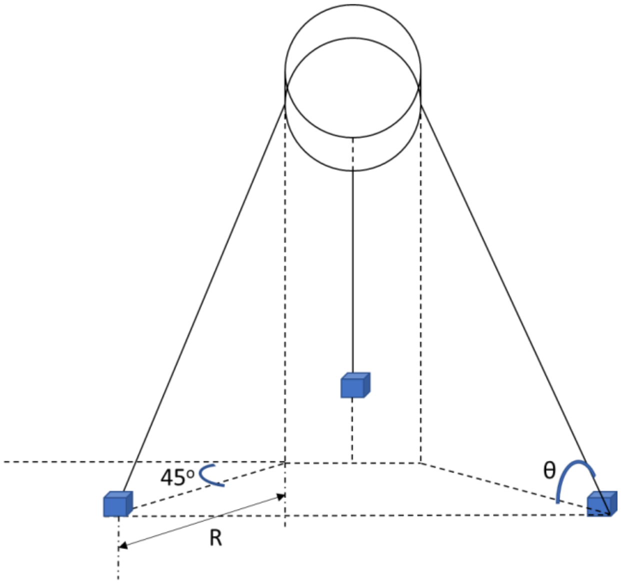

(a) Perspective View

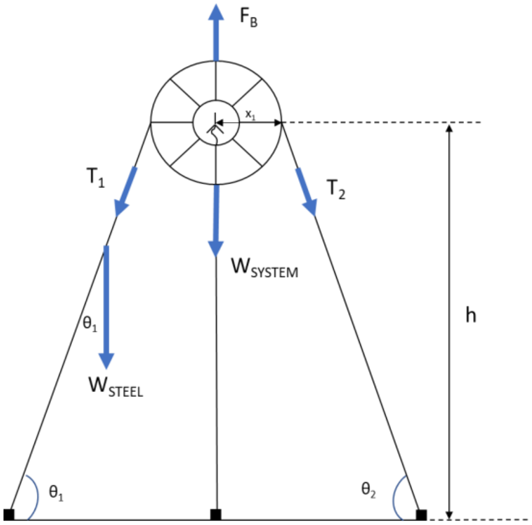

(b) Front View

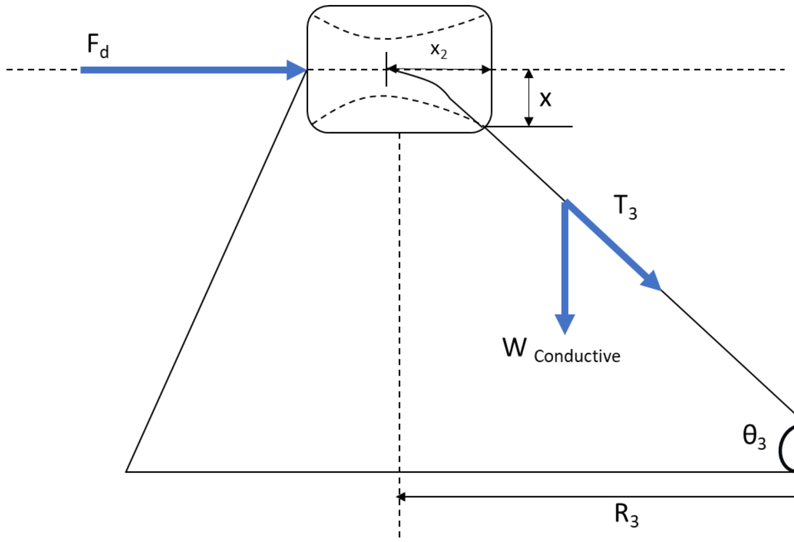

(c) Side View

Figure.5.20. Force Diagram/Dimensional Visualization of the Buoyant Tether System

From figure 20 (a) to (c), we can see that the buoyant force (F_B) should be greater than or equal to the weight of the system:

$$F_B = m_{turbine} . g + \rho_{material}. A_{shroud}. t_{material}. g + \rho_{material}. V_{Steel}. 2. g.\sin\theta + \rho_{material}. V_{Conductive}. g.\sin\theta_3 \tag{5.6}$$

$$F_B = W_{turbine} + W_{shroud} + W_{He,H} + 2. W_{steel} + W_{conductive} \tag{5.7}$$

Where, V_{steel} = Volume of the steel, $t_{material}$ = thickness of the material, $m_{turbine}$= mass of the turbine and $V_{conductive}$ = Volume of the conductive tether

The tether orientation is an essential aspect of the design. From figure 5.20 (a) we can observe that R (Anchor distance support from the center) for the front steel tether is fixed at 45° angle from the center of the horizontal plane, while the anchor for the conductive tether at the tail end is placed at a distance R_3 from the center, figure 5.20 (c). The inclination angle (θ) and tether length of both the support tether and conductive tether are determined below

$$\theta = \left[\frac{h}{R_{Steel/Conductive} - x}\right] \tag{5.8}$$

$$\theta_3 = \left[\frac{h - x_1}{R_{Steel/Conductive} - x_2}\right] \tag{5.9}$$

$$L_{Steel\ Tether} = \frac{h}{\sin\theta} \tag{5.10}$$

$$L_{Conductive\ Tether} = \frac{h - x_1}{\sin\theta} \tag{5.11}$$

Where, h = altitude from the ground, θ = Inclination Angle of Tether in perspective view, L_{tether} = length of the tether and $x = \sqrt{(x_1^2+x_2^2)}$ = diagonal distance from center to the edge of shroud system, x_1 = Outer shroud profile Radius and x_2 = Horizontal distance from center to tether fixed point on shroud system.

Considering, the effect of the drag on the buoyant shroud wall which influences the push down of the buoyant system closer to the ground thereby decreasing the inclination angle in the direction where the drag force is acting. The angle that is influenced by the drag can be derived from the force resolve diagram. In observing the front view projection of the force diagram, we can see that the drag force (F_D) below:

$$F_D = W_{steel} \cos\theta \tag{5.12}$$

We also know that $F_D = \frac{C_D}{2} \rho_{air} A_{shroud} {V_\infty}^2$ (5.13)

The required volume to lift the required payload to the operational altitude can be calculated utilizing the following expression.

$$V_{shroud}(\rho_{air} - \rho_{He})g = m_{turbine} \cdot g + \rho_{material} \cdot A_{shroud} \cdot t_{material} \cdot g + \rho_{material} \cdot V_{Support} \cdot 2. g. \sin\theta + \rho_{material} \cdot V_{Conductive} \cdot g. \sin\theta_3 \tag{5.14}$$

The tension experienced on the tether supports, as a result of the buoyant lift, is calculated by resolving the forces and calculating the linear equations below:

3 Tether

$$\sum F_y = 0$$

$$F_B - W_{system} - 2T_{steel} \sin\theta - T_{conductive} \sin\theta_3 = 0 \tag{5.15}$$

$$\sum F_x = 0$$

$$F_D - 2T_{steel} \cos\theta + T_{conductive} \cos\theta_3 = 0 \tag{5.16}$$

The 4 tether is also resolved similarly utilizing the same force resolving method.

The declination angle (θ declination) as a result of the drag can be derived from the force diagram and the resulting as follows:

$$tan\ \theta_{declination} = \frac{F_B+F_{allowance}}{F_D} \tag{5.17}$$

Initially, $F_{allowance}$ is not taken into consideration for declination angle determination, then to determine the $F_{allowance}$ it is calculated using the equation below:

$$F_{allowance} = F_D.tan\ \theta_1 - F_B \tag{5.18}$$

5.3. Buoyant Shroud System: Conceptual Visualization:

The final interpreted 3D model of the annular buoyant shroud system with the assembly of the turbine for both the 3-tether and the 4-tether configuration is presented below in figures 5.21 and 5.22 respectively:

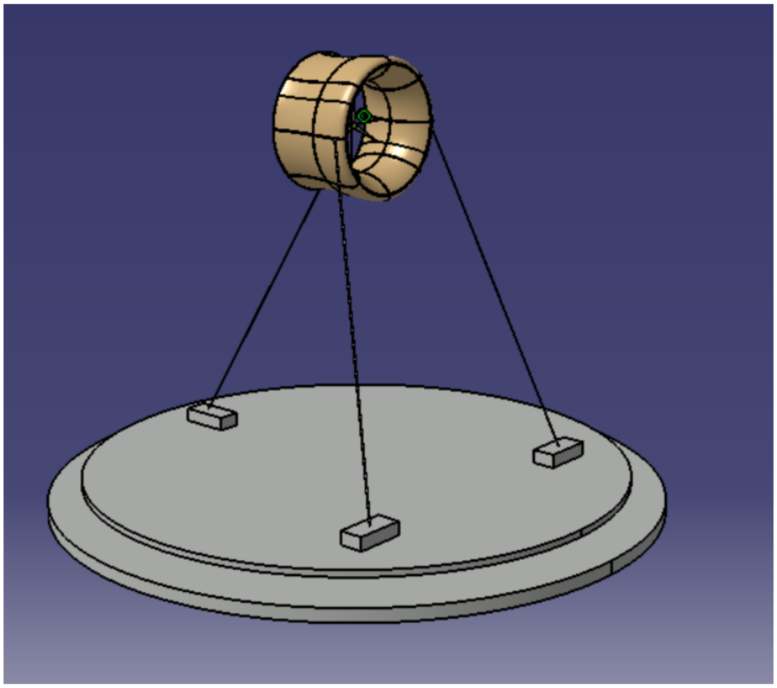

Figure.5.21. 3-Tether Buoyant System Representation

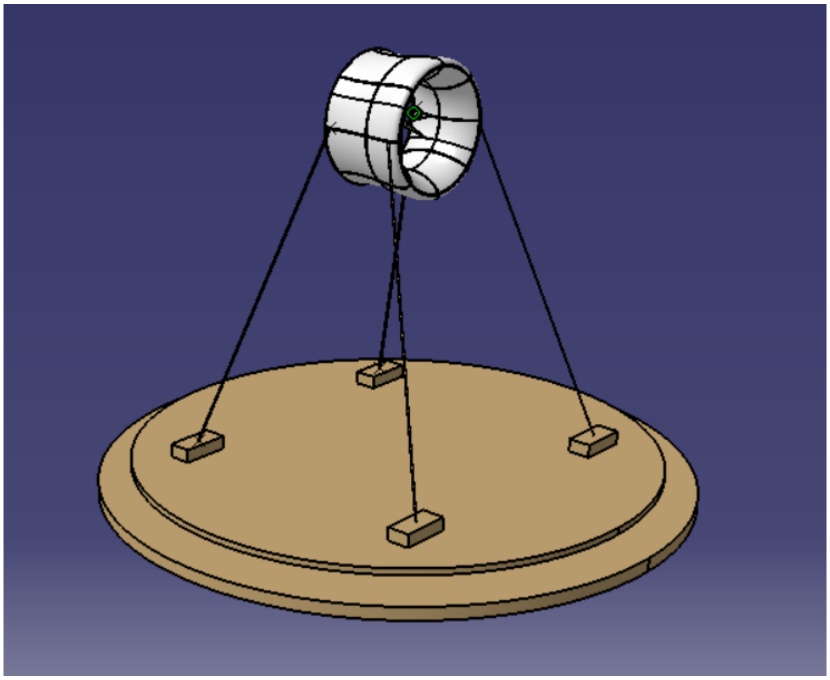

Figure.5.22. 4-Tether Buoyant System Representation

From the figures 5.21 and 5.22 above we can infer that, as a result of the symmetric nature of the shrouded system setup, the net lift force recorded around the annular shroud is 0. With this being the case, the whole system is solely relied on lift generated through the buoyancy. The stability of the system is highly influenced by the drag force that's generated around the annular shroud system. To overcome the disadvantages experienced as a result, the buoyant lift is increased further to negate the influence of the drag on the system thereby increasing the stability of the whole system in its operating condition.

With the presented conceptual design taken into account, the design parameters that influence the performance of the system are the buoyant lift, the net drag force and the tension of the tether. With the conceptual design of the system base platform taken as 90 m for the front support tethers and the 97 m for the back support tethers. With the system measuring at 1500 m3 capacity it had the capability of lifting 1569.75 kg, but the volume needed to lift a system weighing 7705.172 kg is 7362.1 m^3. The weight of the system recorded was about 62694.847 N devoid of the helium as it is taken as a factor for buoyancy calculation, while the buoyant lift was about 75587.7 N, the system generated sufficient lift to perform presenting a 17.02% higher upward force in the lift at its operating condition. With the design velocity as 8m/s considered for analysis of the whole system, the generated net drag force about 56900.31 N, for the annular shroud (13m KT) and the turbine system presenting 173845 N and 1563.25 N respectively, while the lift is

24.72% higher than the drag. To negate the influence of the drag for the stability improvement, an allowance volume of 1255.86 m^3 is added to the volume needed. To stabilize the system at the influence of high drag at high wind velocity, the anchors to which the system is tethered to can pull the system to an altitude where it can perform efficiently.

To operate the system at its optimal efficiency, the system should be introduced to the direction of the wind. The manipulation of the buoyant system towards the wind direction can be controlled through a rotating platform where the anchors to the buoyant system are assembled on top to rotate the whole system based on the direction of the wind. The cut off wind speed system in standard wind turbines typically work when the wind velocity exceeds the prespecified wind speed limit measured by the anemometer. The Aeolos H 30kW turbine possess a mechanical brake system and yaw control system that detects and regulates the orientation of the turbine if the wind speed is over the cutoff capacity [40].

Chapter 6

Conclusion

6.1. Conclusion:

In this thesis, a buoyant turbine system that is capable of harnessing high wind velocities at high altitudes is conceptualized and optimized. The research covered the validation of velocity- altitude models, shroud profile optimization, CFD system simulation and performance predictions and finally a look at the shroud capability at lifting the system. The main research findings can be summsarized as follows:

- The logarithmic law is more accurate in describing the ground boundary layer velocity variation with altitude. Applying the model to collected meteorological data for the UAE showed a deviation of 2.941% between actual and predicted data.
- The topological REmap of UAE was studied to better visualize the wind speed distribution over the UAE. The topological map showed that the mountain regions of Fujairah and Al Ain records higher average wind speed in comparison to the other regions. The REmap findings were substantiated with the 2017 mean wind velocity meteorological data for each locality of the UAE. Fujairah and Al Ain registered 28.8% higher mean velocities in comparison to the other localities.
- The shroud optimization study considered two airfoils, the Karman-Trefftz and the symmetric NACA 4 series, where their performances were compared based on a host of performance indicators including the pressure coefficient, the mass flow rate, the area ratio, the velocity profile, and the mass flow amplification factor. Through a comparison of different chord lengths in the KT model, it was observed that the 13m chord length airfoil gave best results compared to cord lengths ranging from 3 to 15 meters. The continuously increasing trend in the performance of symmetric NACA 4 series airfoils with the cord length forced the use of equal volume concept to compare it to the KT model. The analysis showed that a 25% thickness- NACA 4 series airfoil performs the best among that series, however, it is still inferior to the KT airfoil in wind power augmentation. The 13m KT presented a 270% increase in the available wind power augmentation at the shroud throat section.

- The CFD results of a shrouded turbine indicated a 201% increase in the generated turbine power when compared with the manufacturer data while the CFD results indicated a 221% increase in the power generated from the shrouded turbine in comparison to the CFD results of the bare turbine.
- The conceptual design of the shroud turbine system presented a net buoyant lift of 17.01% higher than the weight of the system while the lifted is also 24.7% higher than the net drag of the system. The allowance of the additional volume, yet the additional buoyant force, is provided to overcome the drag effect on the system stability. The conceptual representation of the system design is also presented for better visualization of the system design and the control system if the turbine experiences adverse conditions during its operation.

6.2. Future Development:

Further experimental study on the buoyant system can be carried out to substantiate the presented conceptual design. This can be done by designing a scaled model of the buoyant system and testing the results in a wind tunnel based on the selected design velocity, creating a prototype, and further testing the performance of the system in selected locations. Further, the economic analysis of the prototype based on hourly wind range in the selected regions of the study will help select a better placement location for optimum performance of the system.

References

[1] **Acciona** ,2020, “Wind Energy”, What are the benefits of wind power? | ACCIONA | Business as unusual

[2] **Twidell, J. and Weir, T**, (2006),” Renewable Energy Resources. 2nd Edition”, Taylor and Francis, London.

[3] **Richard Bowers, Feb 6 2020,”** Wind Energy Statistics”**,** Wind has surpassed hydro as most-used renewable electricity generation source in U.S. - Today in Energy - U.S. Energy Information Administration (EIA)

[4] **Center for Climate and Energy Solutions, 2019**, “Renewable Energy”, Renewable Energy | Center for Climate and Energy Solutions (c2es.org)

[5] **AWEA (Asia Wind Energy Association), 2019, “**United Arab Emirates”**, “**United Arab Emirates – Asia Wind Energy Association 2021”

[6] **IRENA, March 2015,” Renewable Energy Prospects UAE”, “**REmap 2030, Renewable Energy Prospects: United Arab Emirates (irena.org)”

[7] **IRENA , 2019 “ Energy Profile: UAE,”** United Arab Emirates Middle East_RE_SP.pdf (irena.org)”

[8] **Zachary Shahan**, November 2014, “History of Wind Turbine”, “History of Wind Turbines - Renewable Energy World”

[9] **Pope, K., Dincer, I., & Naterer, G. F. (2010),”** Energy and exergy efficiency comparison of horizontal and vertical axis wind turbines”, Renewable Energy, 35(9), 2102–2113. doi:10.1016/j.renene.2010.02.013

[10] **Lindholm Moreton, Nielsen Thomas S Bjertreup, Petersen Torben, Helle Lars**, VESTAS WIND SYSTEMS AS,” Wind energy park with airborne wind energy systems and a direct current (dc) internal grid”, WO2019141334A1, 25th July 2019

[11] **Saleem, A., & Kim, M.-H** (2019).” Performance of buoyant shell horizontal axis wind turbine under fluctuating yaw angles”, Energy, 169, 79–91. doi: 10.1016/j.energy.2018.12.025

[12] **Rob Matheson**, May 15, 2014, “High Flying Turbine Produces more Power,” https://news.mit.edu/2014/high-flying-turbine-produces-more-power-0515 “

[13] **Oliver Abristol**, 2014, “Kiwee one: An Airborne Wind Turbine”, “https://en.wikipedia.org/wiki/Airborne_wind_turbine#/media/File:Kiwee_One.jpg “

[14] **Ben Glass,** Ann Arbor, MI (US),” POWER-AUGMENTING SHROUD FOR Publication Classification”, US 2010/0090473 A1. Apr. 15, 2010

[15] **Trevor Sievert, Nov 12 2014,** ”Interview on BAT”, “What's New in the Wind fair World - The Altaeros Buoyant Airborne Wind Turbine”

[16] **Yirtici, O., Tuncer, I. H., & Ozgen, S**. (2016),” Ice Accretion Prediction on Wind Turbines and Consequent Power Loss”, Journal of Physics: Conference Series, 753, 022022. doi:10.1088/1742-6596/753/2/022022

[17] **Perry Roth Johnson, 2014**.” DU93-W-210 air foil data”. “biplaneblade/DU93-W-210.txt at master · perryjohnson/biplaneblade · GitHub”

[18] **Matthews, Miccal T**. (2012),” Complex mapping of aero foils – a different perspective”, International Journal of Mathematical Education in Science and Technology, 43(1), 43–65. doi:10.1080/0020739X.2011.582174 (use this in Introduction)

[19] **Jacobsson, S., & Bergek, A. (2004)**,” Transforming the Energy Sector: The Evolution of Technological Systems in Renewable Energy Technology”, Industrial and Corporate Change, 13(5), 815– 849

[20] **EIA (2020)**,” Installed electricity capacity”, International - U.S. Energy Information Administration (EIA)

[21] **Hu, X.-M. (2015)**,” Encyclopedia of Atmospheric Sciences: BOUNDARY LAYER (ATMOSPHERIC) AND AIR POLLUTION, Air Pollution Meteorology”.,227–236. doi:10.1016/B978-0-12-382225-3.00499-0

[22] **Nanos, Emmanouil M; Yilmazlar, Kutay; Zanotti, Alex; Croce, Alessandro; Bottasso, Carlo L (2020)**,” Wind tunnel testing of a wind turbine in complex terrain”, Journal of Physics: Conference Series, 1618(), 032041–. doi:10.1088/1742-6596/1618/3/032041

[23] **E. Linacre and B. Geerts.** ,"Roughness length".” http://www-das.uwyo.edu/~geerts/cwx/notes/chap14/roughness.html”

[24] **Lawrence J. De Chant (2005),** “The venerable 1/7th power law turbulent velocity profile: a classical nonlinear boundary value problem solution and its relationship to stochastic processes”, Applied Mathematics and Computation, 161(2), 463–474. doi: 10.1016/j.amc.2003.12.109

[25] **D. F. Menicucci and I. J. Hall.** (1985),” Estimating Wind Speed as A Function of Height Above Ground: An Analysis of Data Obtained at The Southwest Residential Experiment Station”, Las Cruces, New Mexico. SAND84-2530

[26] **Wieringa, J. (1992**),” Updating the Davenport roughness classification”, Journal of Wind Engineering and Industrial Aerodynamics, 41(1-3), 357–368. doi:10.1016/0167-6105(92)90434-c

[27] **Jongyeon Lim, Ryozo Ooka, Hideki Kikumoto**. (2015),” Wind velocity profile observations for roughness parameterization of real urban surfaces”, ICUC9 - 9th International Conference on Urban Climate

[28] **RICHARDS, P. J., & HOXEY, R. P. (1993),”** Appropriate boundary conditions for computational wind engineering models using the k-ε turbulence model”, Computational Wind Engineering 1, 145–153. doi:10.1016/b978-0-444-81688-7.50018-8

[29] **John K. Kaldellis; D. Zafirakis (2011)**,” The wind energy (r)evolution: A short review of a long history. “, 36(7), 1887–1901. Doi: 10.1016/j.renene.2011.01.002

[30] **Daniel Garisto,2022,** July 1887: James Blyth Harness the Wind for Electricity,” https://www.aps.org/publications/apsnews/202207/blyth_harnesses.cfm “

[31] **Wubbo J. Ockels (2001),**" Ladder mill, a novel concept to exploit the energy in the airspace. ", 4(2-3), 81–97. doi:10.1016/s1369-8869(01)00002-7

[32] **Fredrick D Ferguson, Ontario (CA**), SYSTEMS AND METHODS FOR TETHERED WIND TURBINES, US007859 126B2

[33] **Sanuki,** 1950, "Studies on Biplane Wind Vanes, Ventilator Tabes and Cup Anemometers (II)", Papers in Meteorology and Geophysics, Volume 1, Issue 2-4, Pages 227-298, https://doi.org/10.2467/mripapers1950.1.2-4_227

[34] **Abe, K., Nishida, M., Sakurai, A., Ohya, Y., Kihara, H., Wada, E., & Sato, K.** (2005)," Experimental and numerical investigations of flow fields behind a small wind turbine with a flanged diffuser", Journal of Wind Engineering and Industrial Aerodynamics, 93(12), 951–970. doi: 10.1016/j.jweia.2005.09.003

[35] **Saleem, A., & Kim, M.-H.** (2018)," Aerodynamic analysis of an airborne wind turbine with three different aero foil-based buoyant shells using steady RANS simulations", Energy Conversion and Management, pp177, 233–248 doi: 10.1016/j.enconman.2018.09.067

[36] **Ali, Q. S., & Kim, M.-H**. (2021)," Design and performance analysis of an airborne wind turbine for high-altitude energy harvesting", Energy, 230, 120829. doi: 10.1016/j.energy.2021.120829

[37] **Saeed, M., & Kim, M.-H.** (2017)," Aerodynamic performance analysis of an airborne wind turbine system with NREL Phase IV rotor", Energy Conversion and Management, 134, 278–289. doi: 10.1016/j.enconman.2016.12.02

[38] **Samson, J., & Katebi, R.** (2014)," Shroud Design Criteria for a Lighter than Air Wind Energy System", Journal of Physics: Conference Series, 524, 012079. doi:10.1088/1742-6596/524/1/012079

[39] **Bakırcı, Mehmet; Yılmaz, Sezayi** (2018)," Theoretical and computational investigations of the optimal tip-speed ratio of horizontal-axis wind turbines", Engineering Science and Technology, an International Journal, (), S2215098618301381–. doi: 10.1016/j.jestch.2018.05.006

[40] **Aeolos Wind Energy, Ltd,** "Aeolos H 30kW" [Brochure]", http://www.verdeplus.gr/files/Aeolos%20H-30kw%20Brochure.pdf

[41] **Mishnaevsky, Leon; Branner, Kim; Petersen, Helga; Beauson, Justine; McGugan, Malcolm; Sørensen, Bent (2017),"** Materials for Wind Turbine Blades: An Overview. Materials", 10(11), 1285–. doi:10.3390/ma10111285

[42] **Azo Material,2022,"** Properties of E-Glass", August 30, 2001, "Properties: E-Glass Fibre (azom.com)"

[43] **JJ.H.Blom, June 1981,** "Enige Karateristieke Grootheden Van Von Karman-Trefftz "Profielen", Technische Hogeschool, Delft (Netherlands). Department of Aerospace Engineering, Report No. VTH-LR-323,, 40 pp. NATIONAL

[44] **National Aeronautics and Space Administration. June 1981,** "SOME CHARACTERISTIC QUANTITIES OF KARMAN-TREFFTZ PROFILES" NASA TM 79013, JJ.H.Blom

[45] **Matthews, Miccal T. (2012)**, "Complex mapping of aerofoils – a different perspective", International Journal of Mathematical Education in Science and Technology, 43(1), 43–65. doi:10.1080/0020739X.2011.582174

[46] **Houghton, E.L. (2013),"** Aerodynamics for Engineering Students || Two-Dimensional Wing Theory", (), 209–267. doi:10.1016/B978-0-08-096632-8.00004-7

[47] **Stanford**, "the NACA Airfoil Series", https://web.stanford.edu/~cantwell/AA200_Course_Material/The%20NACA%20airfoil%20series.pdf

[48] **Laminated Plastics**, TECHNICAL DATA SHEET Mylar®,"https://laminatedplastics.com/mylar.pdf "

[49] **Reynolds, O. (1895)**, "On the Dynamical Theory of Incompressible Viscous Fluids and the Determination of the Criterion", Philosophical Transactions of the Royal Society A:

Mathematical, Physical and Engineering Sciences, 186(0), 123–164. doi:10.1098/rsta.1895.0004

[50] **Ansys®** ANSYS Fluent Theory Guide, Release 15.0, Help System, Turbulence, ANSYS, Inc

[51] **Prandtl, L. (1925). 7,"** Bericht über Untersuchungen zur ausgebildeten Turbulenz", ZAMM - Journal of Applied Mathematics and Mechanics / Zeitschrift für Angewandte Mathematik und Mechanik, 5(2), 136–139. doi:10.1002/zamm.19250050212

[52] **Versteeg, Henk Kaarle; Malalasekera, Weeratunge** (2007),". An introduction to Computational Fluid Dynamics: The Finite Volume Method. Pearson Education

[53] **Launder, B. E., & Spalding, D. B**. (1974)," The numerical computation of turbulent flows. Computer Methods in Applied Mechanics and Engineering", 3(2), 269–289. doi:10.1016/0045-7825(74)90029-2

[54] **Kekina, Peerakit; Suvanjumrat, Chakrit; Yuan, H.L.; Agarwal, R.K.; Tandon, P.; Wang, E.X. (2017),"** A Comparative Study on Turbulence Models for Simulation of Flow Past NACA 0015 Airfoil Using OpenFOAM," MATEC Web of Conferences, 95(), 12005–. doi:10.1051/matecconf/20179512005

[55] **Douvi C. Eleni, (2012),"** Evaluation of the turbulence models for the simulation of the flow over a National Advisory Committee for Aeronautics (NACA) 0012 airfoil", Journal of Mechanical Engineering Research, 4(3), –. doi:10.5897/JMER11.074

[56] **Menter, F. (1993),"** Zonal Two Equation k-w Turbulence Models for Aerodynamic Flows", 23rd Fluid Dynamics, Plasma dynamics, and Lasers Conference. doi:10.2514/6.1993-2906

[57] **Wilcox, D. C. (2008),"** Formulation of the k-w Turbulence Model Revisited", AIAA Journal, 46(11), 2823–2838. doi:10.2514/1.36541

[58] **Devin Rana, July 2020,** "Sphere Of Influence, Bias And Bias factor, Types of Meshing In Ansys,", https://www.cadsys25.com/2020/06/sphere-of-influence-bias-and-bias-factor-

type-of-meshing-in-ansys.html#:~:text=Bias%20type%20and%20Bias%20factor,edge%20or%20group%20of%20edges.

[59] **UAE Ministry of Climate Change and Environment**, 2017, Wind Speed by Station and Month | Bayanat

[60] **Esri, ArcGis,2022**, “Current Weather and Wind Station Information”,” ArcGIS - Current Weather and Wind Station Information

[61] **Vranková, A., & Palko, M.** (2016),” Atmospheric Boundary Layer. Applied Mechanics and Materials”, 820, 338–344. doi: 10.4028/www.scientific.net/amm.820.338.10.4028/www.scientific.net/amm.820.338

[62] **E.W. Peterson and J.P. Hennesy**,” On the use of power laws for estimates of wind power potential”, J, AoplMeteor 17 (1978) 390-394

[63] **Statistia**, Total area of used land in the emirate of Dubai from 2015 to 2020 (in donums)***,2022,”**UAE: total area of used land in Dubai 2020 | Statista”

[64] **Jake Badger, Neil Davis, Ray Drummond, Andrea Hahmann, Duncan Heathfield, Niels Gylling Mortensen and Marko Onninen. 2015.** “Global Wind Atlas”. Global Wind Atlas

[65] **Waters, Nigel (2003**) 'Geographic Information Systems', Encyclopedia of Library and Information Science, 1: 1, 1106 — 1115

[66] **Mr. Ershad Ali,”** Geographic Information System (GIS): Definition, Development, Applications & Components” Ananda Chandra College

[67] **Aranake, Aniket C.; Lakshminarayan, Vinod K.; Duraisamy, Karthik (2015)**,” Computational analysis of shrouded wind turbine configurations using a 3-dimensional RANS solver. Renewable Energy”, 75(), 818–832. doi: 10.1016/j.renene.2014.10.049

[68] **Marquette Shock Physics,** March 8, 2019, “Wind tunnel pressure data for a NACA 0012 symmetric airfoil”, 12:22, https://www.youtube.com/watch?v=J5aXhnZecvo

[69] **Casey Stockbridge, Alessandro Ceruti, Pier Marzocca, 2012**, “Airship Research and Development in the Areas of Design, Structures, Dynamics and Energy Systems”,Int’l J. of Aeronautical & Space Sci. 13(2), 170–187 (2012), DOI:10.5139/IJASS.2012.13.2.170

[70] **Aeronautics Guide, 2022**, “https://www.aircraftsystemstech.com/p/wings-wing-configurations-wings-are.html “

[71] **Botting, Douglas, et al, 1980,”** The Giant Airships. Time-Life Books”